Gravitational lensing: from micro to nano

- **А.Ф.Захаров (Alexander F. Zakharov)**

- ***Institute of Theoretical and Experimental Physics,***
- ***B. Cheremushkinskaya, 25, 117218 Moscow,***
- ***&***
- ***Boboliubov Laboratory of Theoretical Physics,***
- ***Joint Institute for Nuclear R erach , Dubna***

- **22.08.2009,**

- Lomonosov Conference,
- Moscow State University

- Reference
- New Astronomy Reviews (2009, in press)

1 nano angular second
2.5 cm coin from the Neptune orbit (4.5* 10^{9} km) (about 30 AU)

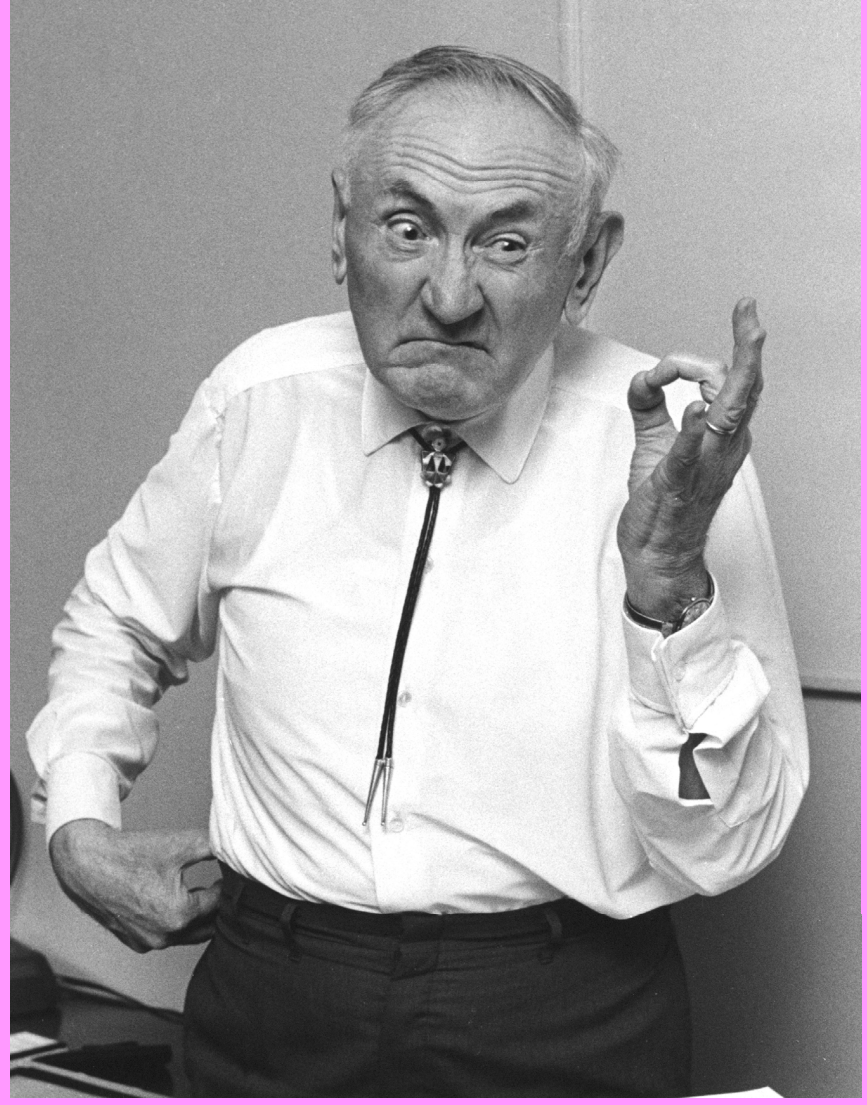

- Fritz Zwicky → DM

Outline

- History (GL, ML, local ML)
- Gravitational microlensing for distant QSOs and GL systems
- Gravitational microlensing toward LMC and SMC & DM problem
- Gravitational microlensing toward Galactic bulge
- Binary lenses (planets), polarization, non-compact lenses
- Pixel microlensing
- Conclusions

History

$$\Theta = \frac{2GM}{c^2 R} \tag{1}$$

or

$$\Theta \sim 0.87'' \tag{2}$$

for $M = M_\odot$ and $R = R_\odot$.

Newton (Optics, 1704): "Does body act on the light, is the action stronger for smaller distances?"

In 1801 J. Soldner presented his derivation of expression (1) for publication.

In 1911 A. Einstein derived the(1) in SR.

In 1915, 1916 A. Einstein derived GR expression for the bending angle of light

$$\Theta = \frac{4GM}{c^2 R} \tag{3}$$

or

$$\Theta \sim 1.75'' \tag{4}$$

and Einstein's prediction was confirmed by A. Eddington in 1919.

Chwolson (1924) and Einstein (1936) analyzed the simple (so called Schwarzschild) GL model. Both of them claimed that there is no chance to detect such a phenomenon because angular distances between images are too small about 10^{-6} angular seconds for cosmological distances.

Zwicky (1936) pointed out the objects where GL effect could be detectable.

Walsh et al. (1979) detected the first gravitational lens system (QSO 0957+561A,B).

aber, wie man sich leicht überzeugt, auf der erwähnten Annahme beruhen.

Damit haben wir die Untersuchung des Meridianinstruments abgeschlossen. Die Untersuchung der Winkelmessung in den zur Meridianebene normalen Ebenen bringt, wie man sich leicht überzeugt, keine neuen Resultate.

Zusammenfassend können wir also sagen: der Winkelmessung liegt die Annahme der euklidischen Kinematik des starren Körpers zu Grunde. Die Verwendung optischer Hilfsapparate (Fernrohr, Mikroskop usw.) bringt keine neuen optischen Annahmen mit sich. Die »Starrheit« der Instrumente wird mit Hilfe unserer Annahme 2 und der Unabhängigkeit der Abbildungsgesetze von der Richtung geprüft. Diese letztere ist zwar noch nicht unmittelbar überprüft, kann aber durch den Ausfall des *Michelson*schen Versuches gestützt werden.

Wien, 1924 Febr. 15. *Fr. Zerner.*

Über eine mögliche Form fiktiver Doppelsterne. Von *O. Chwolson.*

Es ist gegenwärtig wohl als höchst wahrscheinlich anzunehmen, daß ein Lichtstrahl, der in der Nähe der Oberfläche eines Sternes vorbeigeht, eine Ablenkung erfährt. Ist γ diese Ablenkung und γ_0 der Maximumwert an der Oberfläche, so ist $\gamma_0 \geqq \gamma \geqq 0$. Die Größe des Winkels ist bei der Sonne $\gamma_0 = 1''.7$; es dürften aber wohl Sterne existieren, bei denen γ_0 gleich mehreren Bogensekunden ist; vielleicht auch noch mehr. Es sei A ein großer Stern (Gigant), T die Erde, B ein entfernter Stern; die Winkeldistanz zwischen A und B, von T aus gesehen, sei α, und der Winkel zwischen A und T, von B aus gesehen, sei β. Es ist dann

$$\gamma = \alpha + \beta .$$

Ist B sehr weit entfernt, so ist annähernd $\gamma = \alpha$. Es kann also α gleich mehreren Bogensekunden sein, und der Maximumwert von α wäre etwa gleich γ_0. Man sieht den Stern B von der Erde aus an zwei Stellen: direkt in der Richtung TB und außerdem nahe der Oberfläche von A, analog einem Spiegelbild. Haben wir mehrere Sterne B, C, D, so würden die Spiegelbilder umgekehrt gelegen sein wie in einem gewöhnlichen Spiegel, nämlich in der Reihenfolge D, C, B, wenn von A aus gerechnet wird (D wäre am nächsten zu A).

Der Stern A würde als fiktiver Doppelstern erscheinen. Teleskopisch wäre er selbstverständlich nicht zu trennen. Sein Spektrum bestände aus der Übereinanderlagerung zweier, vielleicht total verschiedenartiger Spektren. Nach der Interferenzmethode müßte er als Doppelstern erscheinen. Alle Sterne, die von der Erde aus gesehen rings um A in der Entfernung $\gamma_0 - \beta$ liegen, würden von dem Stern A gleichsam eingefangen werden. Sollte zufällig TAB eine gerade Linie sein, so würde, von der Erde aus gesehen, der Stern A von einem Ring umgeben erscheinen.

Ob der hier angegebene Fall eines fiktiven Doppelsternes auch wirklich vorkommt, kann ich nicht beurteilen.

Petrograd, 1924 Jan. 28. *O. Chwolson.*

Antwort auf eine Bemerkung von *W. Anderson.*

Daß ein Elektronengas einer Substanz mit negativem Brechungsvermögen optisch äquivalent sein müßte, kann bei dem heutigen Stand unserer Kenntnisse nicht zweifelhaft sein, da dasselbe einer Substanz von verschwindend kleiner Eigenfrequenz äquivalent ist.

Aus der Bewegungsgleichung

$$\varepsilon X = \mu \, \mathrm{d}^2x/\mathrm{d}t^2$$

eines Elektrons von der elektrischen Masse ε und der ponderabeln Masse μ folgt nämlich für einen sinusartig pendelnden Prozeß von der Frequenz ν die Gleichung

$$\varepsilon X = -(2\pi\nu)^2 \mu x .$$

Berücksichtigt man, daß εx das »Moment« eines schwingenden Elektrons ist, so erhält man für die Polarisation $p = n\varepsilon x$ eines Elektronengases mit n Elektronen pro Volumeinheit

$$p = -\varepsilon^2 n/[\mu (2\pi\nu)^2] \cdot X .$$

Hieraus folgt, daß die scheinbare Dielektrizitätskonstante

$$D = 1 + 4\pi p/X = 1 - \varepsilon^2 n/(\pi\mu\nu^2)$$

ist. $\sqrt{D}$ ist in diesem Falle der Brechungsexponent, also jedenfalls kleiner als 1. Es erübrigt sich bei dieser Sachlage, auf das Quantitative einzugehen.

Es sei noch bemerkt, daß ein Vergleich des Elektronengases mit einem Metall unstatthaft ist, weil die bei der elementaren Theorie der Metalle zugrundegelegte »Reibungskraft« bei freien Elektronen fehlt; das Verhalten der letzteren ist allein durch die Einwirkung des elektrischen Feldes und durch die Trägheit bedingt.

Berlin, 1924 April 15. *A. Einstein.*

Zur Bemerkung von *W. Anderson* AN 5269.

In his note entitled »Zu Prof. *Einstein*s Bemerkung AN 5233«, *W. Anderson* makes use of the well-known formula for the index of refraction of a medium containing both free

of an electron gas is greater than unity, and that the conductivity is large. This assumption seems to be based on an erroneous conception of dielectric constant and conductivity. In fact, if *Hea-*

DISCUSSION

LENS-LIKE ACTION OF A STAR BY THE DEVIATION OF LIGHT IN THE GRAVITATIONAL FIELD

SOME time ago, R. W. Mandl paid me a visit and asked me to publish the results of a little calculation, which I had made at his request. This note complies with his wish.

The light coming from a star A traverses the gravitational field of another star B, whose radius is R_0. Let there be an observer at a distance D from B and at a distance x, small compared with D, from the extended central line $\overline{AB}$. According to the general theory of relativity, let α_0 be the deviation of the light ray passing the star B at a distance R_0 from its center.

For the sake of simplicity, let us assume that $\overline{AB}$ is large, compared with the distance D of the observer from the deviating star B. We also neglect the eclipse (geometrical obscuration) by the star B, which indeed is negligible in all practically important cases. To permit this, D has to be very large compared to the radius R_0 of the deviating star.

It follows from the law of deviation that an observer situated exactly on the extension of the central line $\overline{AB}$ will perceive, instead of a point-like star A, a luminius circle of the angular radius β around the center of B, where

$$\beta = \sqrt{\alpha_0 \frac{R_0}{D}}.$$

It should be noted that this angular diameter β does not decrease like $1/D$, but like $1/\sqrt{D}$, as the distance D increases.

Of course, there is no hope of observing this phenomenon directly. First, we shall scarcely ever approach closely enough to such a central line. Second, the angle β will defy the resolving power of our instruments. For, α_0 being of the order of magnitude of one second of arc, the angle R_0/D, under which the deviating star B is seen, is much smaller. Therefore, the light coming from the luminous circle can not be distinguished by an observer as geometrically different from that coming from the star B, but simply will manifest itself as increased apparent brightness of B.

The same will happen, if the observer is situated at a small distance x from the extended central line $\overline{AB}$. But then the observer will see A as two point-like light-sources, which are deviated from the true geometrical position of A by the angle β, approximately.

The apparent brightness of A will be increased by the lens-like action of the gravitational field of B in the ratio q. This q will be considerably larger than unity only if x is so small that the observed positions of A and B coincide, within the resolving power of our instruments. Simple geometric considerations lead to the expression

$$q = \frac{l}{x} \cdot \frac{1 + \frac{x^2}{2l^2}}{\sqrt{1 + \frac{x^2}{4l^2}}},$$

where

$$l = \sqrt{\alpha_0 D R_0}.$$

If we are interested mainly in the case $q \gg 1$, the formula

$$q = \frac{l}{x},$$

is a sufficient approximation, since $\frac{x^2}{l^2}$ may be neglected.

Even in the most favorable cases the length l is only a few light-seconds, and x must be small compared with this, if an appreciable increase of the apparent brightness of A is to be produced by the lens-like action of B.

Therefore, there is no great chance of observing this phenomenon, even if dazzling by the light of the much nearer star B is disregarded. This apparent amplification of q by the lens-like action of the star B is a most curious effect, not so much for its becoming infinite, with x vanishing, but since with increasing distance D of the observer not only does it not decrease, but even increases proportionally to $\sqrt{D}$.

ALBERT EINSTEIN

INSTITUTE FOR ADVANCED STUDY,
PRINCETON, N. J.

Alle Dreiecke sind gleichschenklig

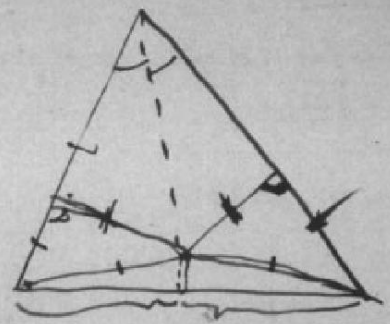

Herstellung
Berlin-Halensee,
Joachim Friedrichstr. 33.

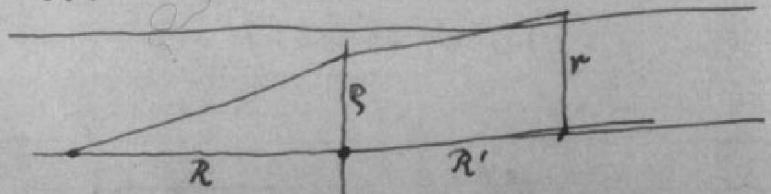

$$r = \varrho\frac{R+R'}{R} - \frac{R'\alpha}{\varrho}$$

ϱ ist nach unten negativ. Dann gilt auch für stärkabgebogene Strahl.

$$r_0 = \varrho_0 - \frac{1}{\varrho_0} \quad \ldots (1)$$

$$\boxed{\varrho_0^2 = \varrho^2\frac{R+R'}{RR'\alpha}}$$

Einsetzt. $r = \cdot - \frac{R\alpha}{\varrho} = \cdot - \frac{R\alpha}{\varrho_0}\sqrt{\frac{R+R'}{RR'\alpha}}$

$$= \cdot - \frac{1}{\varrho_0}\sqrt{\frac{R}{R'}(R+R')\alpha}$$

$$\left.\begin{aligned} \boxed{r_0 = r\sqrt{\frac{R'}{R(R+R')\alpha}}} \\ \boxed{\varrho_0 = \varrho\sqrt{\frac{R+R'}{RR'\alpha}}} \end{aligned}\right\} (2)$$

1) gibt zwei Wurzeln für ϱ_0

Von hier an Index $_0$ weggelassen.

$$2 + r^2 = \varrho^2 + \frac{1}{\varrho^2}$$

$$f = \varphi + \frac{\pi^2}{\varphi}$$

$$df = \left(1 - \frac{\pi^2}{\varphi^2}\right)d\varphi = \left(1 - \frac{1}{\varrho^4}\right)d\varphi$$

$$\mathcal{H}df = \pm H\,d\varphi$$

$$\mathcal{H} = \pm\frac{H}{1 - \frac{1}{\varrho^4}}$$

$$\mathcal{H}_{tot} = H\left\{\frac{1}{1 - \frac{1}{\varrho_1^4}} + \frac{1}{\frac{1}{\varrho_2^4} - 1}\right\} \quad \ldots (3)$$

Klemmer gibt relative Helligkeit. (für ∞ = 1)

$\frac{\varrho_1^4}{\varrho_1^4 - 1}$ $\quad r = \frac{1}{x} - x$

$$\{\ \} = \frac{1}{1 - x_1^4} + \frac{1}{x_2^4 - 1}$$

Nebulae as Gravitational Lenses

Einstein recently published[1] some calculations concerning a suggestion made by R. W. Mandl, namely, that a star B may act as a "gravitational lens" for light coming from another star A which lies closely enough on the line of sight behind B. As Einstein remarks the chance to observe this effect for stars is extremely small.

Last summer Dr. V. K. Zworykin (to whom the same idea had been suggested by Mr. Mandl) mentioned to me the possibility of an image formation through the action of gravitational fields. As a consequence I made some calculations which show that extragalactic *nebulae* offer a much better chance than *stars* for the observation of gravitational lens effects.

In the first place some of the massive and more concentrated nebulae may be expected to deflect light by as much as half a minute of arc. In the second place nebulae, in contradistinction to stars, possess apparent dimensions which are resolvable to very great distances.

Suppose that a distant globular nebula A whose diameter is 2ξ lies at a distance, a, which is great compared with the distance D of a nearby nebula B which lies exactly in front of A. The image of A under these circumstances is a luminous ring whose average apparent radius is $\beta=(\gamma_0 r_0/D)^{\frac{1}{2}}$, where γ_0 is the angle of deflection for light passing at a distance r_0 from B. The apparent width of the ring is $\Delta\beta=\xi/a$. The apparent total brightness of this luminous ring is q times greater than the brightness of the direct image of A. In our special case $q=2la/\xi D$, with $l=(\gamma_0 r_0 D)^{\frac{1}{2}}$. In actual cases the factor q may be as high as $q=100$, corresponding to an increase in brightness of five magnitudes. The surface brightness remains, of course, unchanged.

The discovery of images of nebulae which are formed through the gravitational fields of nearby nebulae would be of considerable interest for a number of reasons.

(1) It would furnish an additional test for the general theory of relativity.

(2) It would enable us to see nebulae at distances greater than those ordinarily reached by even the greatest telescopes. Any such *extension* of the known parts of the universe promises to throw very welcome new light on a number of cosmological problems.

(3) The problem of determining nebular masses at present has arrived at a stalemate. The mass of an average nebula until recently was thought to be of the order of $M_N=10^9\,M_\odot$, where $M_\odot$ is the mass of the sun. This estimate is based on certain deductions drawn from data on the intrinsic brightness of nebulae as well as their spectrographic rotations. Some time ago, however, I showed[2] that a straightforward application of the virial theorem to the great cluster of nebulae in Coma leads to an average nebular mass four hundred times greater than the one mentioned, that is, $M_N'=4\times10^{11}M_\odot$. This result has recently been verified by an investigation of the Virgo cluster.[3] Observations on the deflection of light around nebulae may provide the most direct determination of nebular masses and clear up the above-mentioned discrepancy.

A detailed account of the problems sketched here will appear in *Helvetica Physica Acta*.

F. Zwicky

Norman Bridge Laboratory,
California Institute of Technology,
Pasadena, California,
January 14, 1937.

[1] A. Einstein, Science **84**, 506 (1936).
[2] F. Zwicky, Helv. Phys. Acta **6**, 124 (1933).
[3] Sinclair Smith, Astrophys. J. **83**, 23 (1936).

Emergence of Low Energy Protons from Nuclei

In some experiments recently described[1] the emission of protons in alpha-particle induced transmutations has been studied. In several cases the interesting fact was noticed that protons of relatively low energy were emitted in considerable numbers. Thus for each of the reactions

$$\begin{aligned}
&Al^{27}+He^4\rightarrow Si^{30}+H^1,\\
&P^{31}\ +He^4\rightarrow S^{34}\ +H^1,\\
&Cl^{35}+He^4\rightarrow A^{38}+H^1,\\
&Ca^{40}+He^4\rightarrow Sc^{42}+H^1,
\end{aligned}$$

a group of protons of maximum range 20 cm or less is found and the yield is in general large (more than one-third of the total number of protons emitted). In each case protons of range 10 cm are observed with no apparent diminution of the probability of emission. The question arises as to how these low energy protons get out of the composite nucleus.

In recent experiments in this laboratory the excitation curve for the emission of neutrons from argon under alpha-particle bombardment has been plotted and the nuclear radius found to be 7.3×10^{-13} cm which is in accord with Bethe's revised radii for the radioactive elements[2] and may be taken as a basis for calculation of the nuclear radii of Si^{30}, S^{34}, A^{38}, Ca^{42} and Sc^{42}. Other evidence (e.g., scattering experiments) indicates, if anything, smaller radii than those found in this way. In Table I are given the radii so calculated, together with the heights of the corresponding proton barriers and the range of a proton just able to surmount them. It will be seen that in every case the experimentally observed ranges are smaller than necessary to scale the barrier. It therefore appears that we can draw one of two significant conclusions from the experimental data. Either *barriers to emerging protons are abnormally low* or *the composite nucleus containing the final product element and the proton has a finite lifetime sufficiently long to enable the proton to leak through the barrier*. The latter view, which is in accordance with Bohr's conception of transmutation,[3]

Table I.

Product Nucleus	Nuclear Radius ($\times10^{13}$cm)	Proton Barrier Height (Mev)	Range to Scale Barrier (cm)	Experimentally Found Range
Si^{30}	6.7	3.0	14.0	<10
S^{34}	6.9	3.3	16.5	<10
A^{38}	7.2	3.6	19.0	<10
Ca^{42}	7.4	3.9	22.0	14
Sc^{43}	7.5	4.0	23.0	<10

Constraints on DM objects from GL.

Technique	Mass range ($M_\odot$)	Ω_m	Refs
Multiple images of bright quasars	$10^{10} - 10^{12}$	0.02	Surdej et al. (1993)
Multiple images of compact sources	$10^{6} - 10^{8}$	0.05	Kassiola et al. (1993)
Echos from GRBs of compact sources	$10^{6.5} - 10^{8.1}$	< 1	Nemiroff et al. (1993)
Quasar variability	$10^{-2} - 10^{-3}$	< 0.1	Schneider (1993)
Femtolensing of GRBs	$10^{-17} - 10^{-18}$	?	Gould (1992)

Constraints on DM objects from GL

(Wambsganss(1993))

Prefix	Deflection angle (")	Mass $M/M_\odot$	Lens	Time delay
kilo	10^3	10^{18}	supercluster	
macro	10^0	10^{12}	galaxy	months
milli	10^{-3}	10^6	MBH	min
micro	10^{-6}	10^0	star	10^{-4} sec
nano	10^{-9}	10^{-6}	planet	10^{-10} sec
pico	10^{-12}	10^{-12}	???	10^{-16} sec
femto	10^{-15}	10^{-18}	comet	10^{-22} sec

Just after the discovery of the first multiple imaged quasar QSO 0957+561 A,B by Walsh, Carswell & Weymann (1979) the idea of microlensing by low mass stars in heavy halo was suggested by Gott (1981).

First evidences of quasar microlensing was found by Irwin et al. (1989).

Now there are a number of known gravitational lens systems (Claeskens & Surdej 2002; Browne et al. 2003) and some of them indicate evidences for microlensing (Wambsganss 2001a).

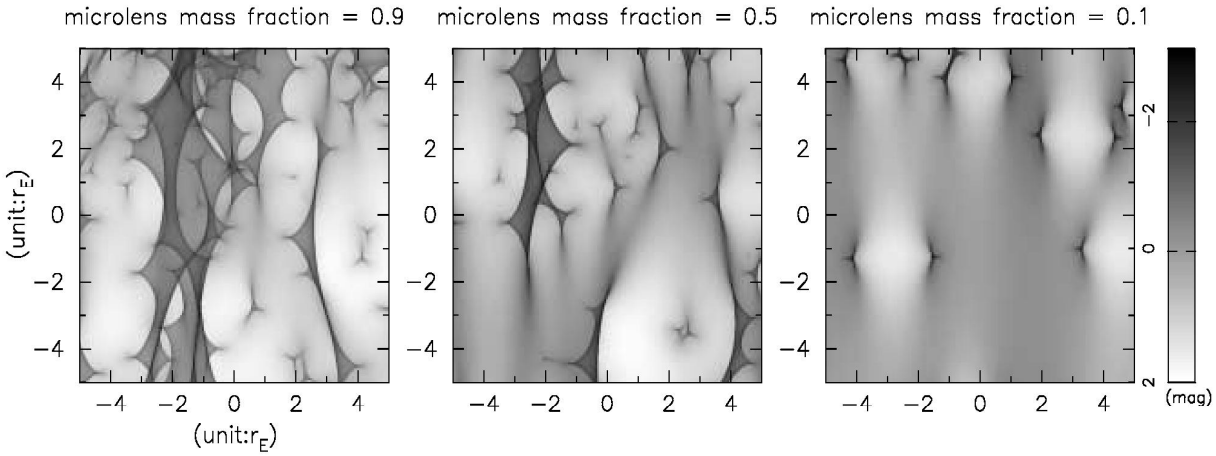

Figure 1 Magnification patterns for quasar microlensing in the case of microlens mass fraction = 0.9, 0.5, and 0.1 are displayed in left, middle, and right panel, respectively. These figures are calculated from the code developed by Wambsganss (1990).

10.1071/AS01014 1323-3580/01/020211$05.00

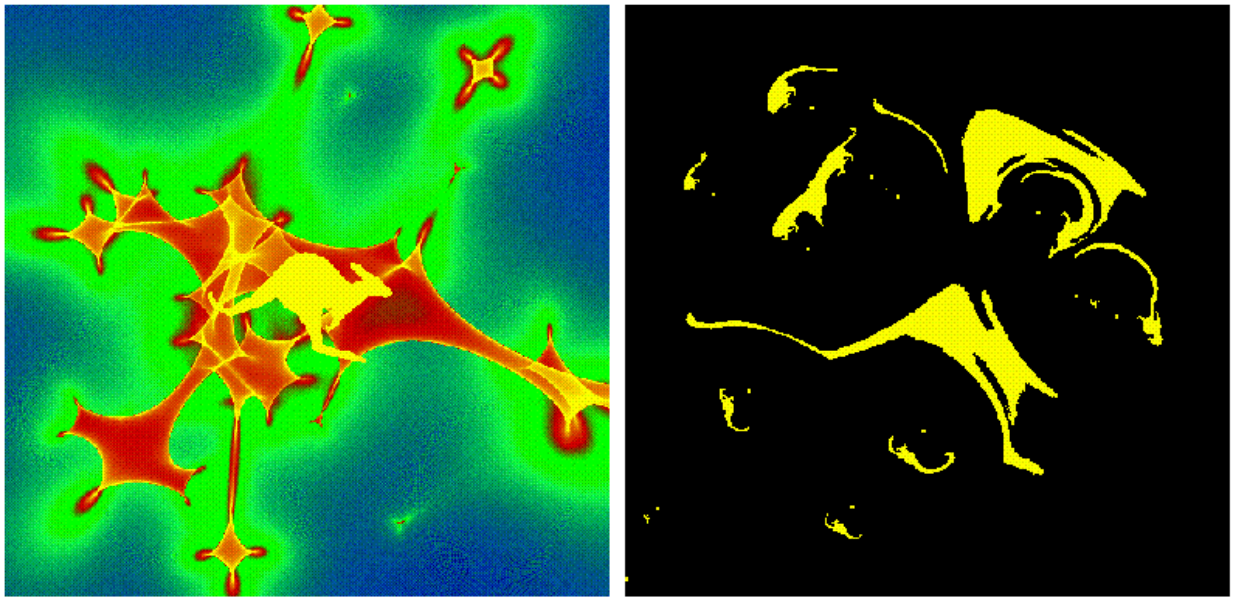

Figure 1 Illustration of how a caustic/magnification distribution (left) of stars/compact objects can distort and differentially magnify a background object (right).

Notations and expressions

$$\vec{\eta} = D_s\vec{\xi}/D_d - D_{ds}\vec{\Theta}(\vec{\xi}). \quad (5)$$

For Schwarzschild GL

$$\vec{\Theta}(\vec{\xi}) = 4GM\vec{\xi}/(c^2\xi^2). \quad (6)$$

If $\vec{\eta} = \vec{0}$ then

$$\xi_0 = \sqrt{\frac{4GM}{c^2} \times \frac{D_d D_{ds}}{D_s}}$$

is Einstein – Chwolson radius and

$$\theta_0 = \xi_0/D_d \quad (7)$$

is Einstein – Chwolson angle. If we introduce dimensionless variables $\vec{x} = \vec{\xi}/\xi_0, \vec{y} = D_s\vec{\eta}/(\xi_0 D_d)$ then

$$\vec{y} = \vec{x} - \vec{x}/x^2. \quad (8)$$

The Eq. (8) has two roots

$$\vec{x}^{\pm} = \vec{y}\left(\frac{1}{2} \pm \sqrt{\frac{1}{4} + \frac{1}{y^2}}\right) \quad (9)$$

and

$$l = |x^-| + |x^+| = 2y\sqrt{\frac{1}{4} + \frac{1}{y^2}}. \quad (10)$$

Astron. Astrophys. 260, 1–13 (1992)

ASTRONOMY AND ASTROPHYSICS

Research Note

The gravitational lens equation near cusps

P. Schneider and A. Weiss

Max-Planck-Institut für Astrophysik, Karl-Schwarzschild-Str. 1, W-8046 Garching bei München, Federal Republic of Germany

Received January 11, accepted February 29, 1992

Abstract. The behaviour of the gravitational lens mapping near cusps is studied, both analytically and numerically, paying particular attention to magnification probabilities. We demonstrate that the three images of a point source inside a cusp satisfy the relation that the sum of the magnifications of the two images with the same parity equals, up to a sign, the magnification of the third image (of opposite parity). This property will then be used to show that the asymptotic magnification cross-section for point sources, in the limit $\mu_s \to \infty$, derived previously for folds only, is also valid in the presence of cusps. The next order term of such an expansion, which is due to sources just outside of cusps, is derived. We apply these relations to a special gravitational lens model and show that these asymptotic relations are indeed very good approximations for the large-μ_s cross-sections. For the study of the magnification of extended sources near cusps, we generalize the ray-shooting method to allow for very small sources. The magnification cross-sections for extended sources are then compared to those for point sources. A magnification contour plot for extended sources near a cusp is obtained. Since the largest magnifications of sources occur near cusps, this paper may directly apply to studies of the amplification bias in source counts.

Key words: gravitational lensing, Catastrophe Theory

1. Introduction

The gravitational deflection of light, in the approximation of gravitational lens theory, can be described by a mapping $f : \mathbb{R}^2 \to \mathbb{R}^2$ from the lens plane (or a small part of the observer's sky) to the source plane (or the corresponding part of the sphere of constant source redshift). In the case of a single geometrically-thin deflector, this is a gradient mapping (for an introduction to gravitational lens theory, see Blandford & Narayan 1986, hereafter BN; Blandford & Kochanek 1987; Schneider, Ehlers & Falco 1992, hereafter SEF). The behaviour of such a gradient mapping near critical points, i.e., points where the Jacobian of the lens mapping vanishes, is investigated and classified by Catastrophe Theory (e.g., Poston & Steward 1978; Gilmore 1981; for applications in gravitational lensing, see BN; Kovner 1987a; SEF, Chap. 6). In a generic lens mapping, the critical points form closed, smooth, non-intersecting curves (so-called critical curves), and their image curves under the mapping f are the so-called caustics. They are also closed curves, but can intersect each other, self-intersect, and are not necessarily smooth, but can have cusps.

Caustics are an important ingredient in gravitational lens theory, for several reasons. First, the number of images of a source changes by ± 2 if, and only if, the source position changes across a caustic. Hence, knowing the structure of the caustics allows a qualitative understanding of the lens mapping, at least concerning image multiplicities. Also, if one considers families of lens mapping, Catastrophe Theory allows to predict the parameter values of the models at which the caustic structure changes, thus allowing a classification of parametrized lens models (for an example, see Erdl & Schneider 1992). Second, the magnification of a source, which is due to the area distortion of the lens mapping (i.e., the inverse of the Jacobian) becomes largest if the source is near a caustic. In particular, to determine the probability distribution for very large magnification of sources, one has to consider the lens mapping near caustics only.

A generic lens mapping has only two types of singularities, folds and cusps. At fold points, the caustic is smooth. A source on the "positive side" of a fold has two images close to, and on opposite sides of the corresponding critical curve. By approaching the caustic, the two critical images move closer together, thereby brightening. At the point where the source crosses the caustic, the two images attain (formally) infinite magnification (in practice, a finite source size leads to finite values of the magnification, but if we had a sufficiently compact source, wave optics effects would limit the magnification; see Chap. 7 of SEF and references therein), merge and disappear thereafter. The magnification of a point source scales like $1/\sqrt{y}$, where y is the distance of the source from the caustic. Considering folds only, the magnification probability of point sources in the limit of high magnifications, $\mu \to \infty$, behaves like μ^{-2}, and the constant of proportionality can be derived as a particular integral over the critical curves of the lens mapping (see BN, SEF, and Sect. 2.4 below).

The derivation of this probability distribution neglects the fact that cusps show a different behaviour. The standard argument implicitly used is that "cusps form a set of measure zero in the set of all critical points"; one therefore expects that cusps do neither change the shape, nor the amplitude of the $p(\mu) \propto \mu^{-2}$ law. Cusps are isolated points, connected by folds. A source close

Send offprint requests to: P. Schneider

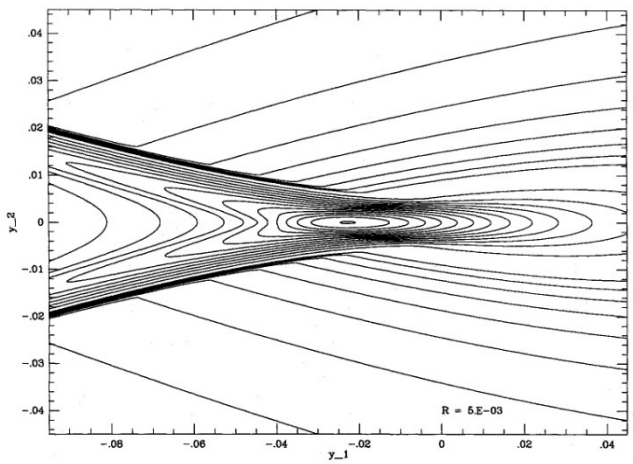

Fig. 5. Magnification contours around a generic cusp. The source radius chosen for this plot was $5\,10^{-3}$. The contour levels range from 3 to 10 in steps of one, and then to 80 (central contour) in steps of 5.

be the following: select a region in the source plane such that all points with magnification $> \mu_0$ lie inside the selected region (this region, in the case of the Chang-Refsdal lens, is preferentially chosen as a rectangle). Then, distribute N point sources inside this region (with area $\mathscr{A}$), calculate their magnifications from the lens equation, assign to each point a differential cross-section $d\sigma = \mathscr{A}/N$ and add up these differential cross-sections. If the N points are distributed randomly, we can easily estimate the number of points required for a given accuracy. If $\mathscr{A} \sim 4$, and $\sigma(10^3) \sim 4 \times 10^{-6}$ (typical values for the Chang-Refsdal lens), then $N_{1000} \sim 10^{-6}N$ points will have magnification $> 10^3$. If the cross-section is to be determined to within an accuracy of 10^{-3}, we would need $N = 10^{12}$ points — a hopeless task. The situation is slightly better if the points are not distributed randomly, but on a regular grid. Nevertheless, even then the computing time would be much too large for calculating accurate cross-sections for large μ_p.

To overcome these difficulties, we use a hierarchical method, based on the idea 'to use the computing time for interesting source positions'. For example, we want to distribute a higher density of points in regions where the magnification is large. Ideally, the number of source positions should be the same for each logarithmic bin of magnification, so that the statistical accuracy is smooth over the whole μ-interval considered. We now describe such a method applicable to point sources; a similar method has been used for extended sources, as described in the next subsection.

Consider the area $\mathscr{A}$ to be divided up into N squares. If the magnification at the center of a square is μ_p, we assign to this square a differential cross-section $d\sigma(\mu_p) = \mathscr{A}/N$. If this particular square is 'interesting' (we will specify this below), we can divide it into four subsquares and again calculate the magnification at the center of each subsquare (the corresponding differential cross-section then is $\mathscr{A}/(4N)$). If one or more of these subsquares appears again 'interesting', further divisions can be made; we can go down this hierarchy as far as desired.

Squares are 'interesting' if they have high magnification, if the gradient across the square is large, or if a caustic crosses the square (these conditions are not mutually exclusive, of course). We have defined numerical criteria according to the preceding prescription of 'interesting'; for example, if the magnification of a square at hierarchy level n is larger than μ_n, the square is further divided (it was found that $\mu_{n+1} = \mu_n\ 10^{0.15}$ is a good splitting criterium). Further, if the magnification factors at the corners of a square differed by more than 0.5, subdivision was applied. For the calculations shown in this paper, 14 hierarchy levels were used.

The solutions of the lens equation, and thus the point source magnification, can be calculated for the Chang-Refsdal lens, using the equations of Sect. 3. For each source position, one has to solve the fourth-order equation (3.3b), insert the real solutions into (3.3a), and calculate the magnification of each individual image. In connection with the hierarchical splitting of the source plane as described above, we have implemented an efficient and reliable method to solve Eq. (3.3a). This method will be described next; however, another method of solving the lens equation, to be described later, turned out to be superior in the situation considered here.

The Chang-Refsdal-equation in the form of Eq. (3.3b) can in principle be solved by any reasonable root-finder for polynomials or other well-behaved functions. Indeed, some of the root-solvers (e.g. from Press et al., 1986) worked well for most of the tested source positions, but with no exception all failed for those being close to cusps. The reason lies in the fact that at cusps a terrace point in the fourth-order polynomial $f(u)$ (given by (3.3b)) develops into a pair of extrema, or, in other words, a single root changes into three. All tested standard root-solvers gave the wrong number of roots of $f(u)$ on either side of the cusp! Numerically, a root cannot be found with an accuracy higher than $\approx 10^{-8}$ for coefficients of (3.3b) of the order of one by propagation of the machine inaccuracy into the powers of u.

Astron. Astrophys. 293, 1–4 (1995)

ASTRONOMY AND ASTROPHYSICS

On the magnification of gravitational lens images near cusps

Alexander F. Zakharov[1,2]

[1] Institute of Theoretical and Experimental Physics, B.Cheremushkinskaya, 25, 117259, Moscow, Russia
[2] Max-Planck-Institut für Astrophysik, Karl-Schwarzschild-Strasse 1, D-85740 Garching, Germany

Received 6 November 1993 / Accepted 30 April 1994

Abstract. On the base of the gravitational lens equation obtained by Schneider & Weiss the magnification of images near a cusp is investigated. Using the symmetrical polynomials on the roots of the polynomial of the third degree we slightly generalize the Schneider & Weiss statement on the magnification near different solutions of the gravitational lens equation. The analytical expressions for magnifications of different images near the cusp are presented.

Key words: gravitational lensing

1. Introduction

It is well known that the mapping of two-dimensional surfaces into a plane gives only two types of stable singularities: folds and cusps (pleats). There are also similar singularities of caustics in gravitational lens optics. Schneider & Weiss (1986; 1992) studied the gravitational lens mapping near the cusps. Mandzhos (1993) investigated the mutual coherence by solving analytically the gravitational lens equation near the cusp. In turn, we study the magnification near the cusp and obtain a useful analytical expression for it.

2. Basic equations

We recall the basic equations from Schneider & Weiss (1992) before considering their gravitational lens equation near the cusp. As is shown in Schneider, Ehlers & Falco (1992), hereafter SEF, the gravitational lens equation may be written in the following form: let the distance between an observer and a source be D_s, the distance between an observer and the gravitational lens be D_d , and D_{ds} be the distance between the gravitational lens and a source. If we suppose a small angle of deflection then we have the following simple expression for the lens equation (SEF)

$$\boldsymbol{\eta} = D_s\, \boldsymbol{\xi}/D_d + D_{ds}\, \boldsymbol{\beta}(\boldsymbol{\xi}),$$

Send offprint requests to: A.F. Zakharov

where the vectors $\boldsymbol{\eta}, \boldsymbol{\xi}$ define the coordinates in source plane and in the lens plane respectively (SEF),

$$\boldsymbol{\beta}(\boldsymbol{\xi}) = 4G/c^2 \int \rho\,(\boldsymbol{R})\,(\boldsymbol{\xi} - \boldsymbol{R})\,/\,|\,\boldsymbol{\xi} - \boldsymbol{R}|^2\ \mathrm{dXdY},$$

where $\boldsymbol{R}=\{X, Y\}$ is the point vector in the lens plane, $\rho(\boldsymbol{R})$ is the surface mass density of the gravitational lens. We introduce the following variables (SEF)

$$\boldsymbol{x} = \boldsymbol{\xi}/R_0, \quad \boldsymbol{y} = D_s\, \boldsymbol{\eta}/(R_0 D_d),$$

where $R_0 = \sqrt{2r_g D_d D_{ds}/D_s}$ is the Einstein - Chwolson radius (see Historical Remarks in SEF). We also introduce the following notation for the scaled (SEF) angle

$$\boldsymbol{\alpha} = \boldsymbol{\beta}\, D_{ds} D_d/(D_s R_0).$$

In the modelling of gravitational lenses, the surface mass density is normalized with the critical surface mass density (Wamsganss 1990)

$$\rho_{cr} = \frac{c^2 D_s}{4\pi G D_d D_{ds}}.$$

For typical lensing situations the critical surface mass density is of the order of $\rho_{cr} = 10^4 M_\odot pc^{-2}$ (Wamsganss 1990). Therefore, if we define the scaled surface mass density by the following expression (SEF)

$$\sigma = \rho/\rho_{cr},$$

then we have the expression for the angle $\boldsymbol{\alpha}$

$$\boldsymbol{\alpha}(\boldsymbol{x}) = \int \sigma\,(\boldsymbol{x}')(\boldsymbol{x} - \boldsymbol{x}')/|\boldsymbol{x} - \boldsymbol{x}'|^2\ d^2x'.$$

As Schneider (1985) showed, we may introduce the scalar potential ψ, such, that

$$\boldsymbol{\alpha}(\boldsymbol{x}) = \nabla\psi\,(\boldsymbol{x}),$$

where

If we introduce (as in SEF)

$$\phi\,(\boldsymbol{x},\boldsymbol{y}) = (\boldsymbol{x}-\boldsymbol{y})^2/2 - \psi(\boldsymbol{x}),$$

we can write the lens equation in the form (Schneider 1985)

$$\nabla\phi\,(\boldsymbol{x},\boldsymbol{y}) = 0.$$

It is easy to see that mapping $x \mapsto y$ is a Lagrange mapping (Arnold 1979), since that is gradient mapping (Arnold 1983). Really, if we consider the function

$$S = \boldsymbol{x}^2\ /2 - \psi\,(\boldsymbol{x}),$$

then

$$\boldsymbol{y} = \nabla S.$$

Singularities of Lagrange's mappings are described in Arnold's paper (1972), and in Arnold's review (1983), and their bifurcations are described in Arnold's paper (1976).

Equation (1) defined the mapping of points on the lens plane into points on the source plane. Using the Jacobian matrix we define the local mapping (SEF):

$$\delta\,\boldsymbol{y} = A\,\delta\,\boldsymbol{x},$$

$$A = \begin{pmatrix} \partial y_1/\partial x_1 & \partial y_1/\partial x_2 \\ \partial y_2/\partial x_1 & \partial y_2/\partial x_2 \end{pmatrix} = \begin{pmatrix} 1-\psi_{11} & -\psi_{12} \\ -\psi_{21} & 1-\psi_{22} \end{pmatrix}, \qquad (2)$$

where

$$\psi_{ij} = \frac{\partial^2\psi}{\partial x_i \partial x_j}(i,j=1,2). \qquad (3)$$

Let us consider lenses which are systems of point masses. Outsides the points where the masses are located, we have the following equality (SEF)

$$\psi_{22} = -\psi_{11}, \qquad (4)$$

since the potential obeys the Laplace equation.

The magnification of an image at $\boldsymbol{x}$ is

$$\mu(\boldsymbol{x}) = 1/\det A\,(\boldsymbol{x}),$$

(where the mapping is not one-to-one). The set is formed by so-called critical curves (SEF).

Since $\det A(\gamma^{(c)}) = 0$ (at points on the critical curve), it is possible to find coordinates with $\phi_{11} \neq 0, \phi_{12} = \phi_{22} = 0$. As shown in Schneider & Weiss (1992), the lens equation near the cusp can be represented as

$$\begin{aligned} y_1 &= cx_1 + \frac{b}{2}{x_2}^2, \\ y_2 &= bx_1x_2 + a{x_2}^3, \end{aligned} \qquad (5)$$

where $a = \frac{1}{6}\phi_{2222}, b = \phi_{122}, c = \phi_{11}$ and $c \neq 0, b \neq 0, 2ac - b^2 \neq 0$. It was shown in SEF that additional terms do not affect the local properties of the mapping. It is possible to see that by the direct comparison of terms (for example the term with ϕ_{112} is smaller than the term with ϕ_{11}) or using Newton's polygon or Bruno's truncating rules (see for example Bruno 1989). Similar to Schneider & Weiss (1992), we introduce the notations

$$\hat{x}_1 = \frac{c}{b}x_1, \quad \hat{x}_2 = x_2, \quad \hat{y}_1 = y_1/b, \quad \hat{y}_2 = \frac{c}{b^2}y_2, \qquad (6)$$

then we have

$$\begin{aligned} \hat{y}_1 &= \hat{x}_1 + \frac{1}{2}\hat{x}_2^2, \\ \hat{y}_2 &= \hat{x}_1\hat{x}_2 + s\hat{x}_2^3, \end{aligned}$$

where $s = ac/b^2$. We also introduce $S = 1 - 2s$, $\tilde{y}_1 = 2\hat{y}_1/3S$, $\tilde{y}_2 = \hat{y}_2/S$; then we have (Schneider & Weiss 1992)

$$\hat{x}_1 = \frac{3S}{2}\tilde{y}_1 - \frac{1}{2}\hat{x}_2^2, \qquad (7)$$

$$\hat{x}_2^3 - 3\tilde{y}_1\hat{x}_2 + 2\tilde{y}_2 = 0. \qquad (8)$$

3. Statement on the magnifications of images near cusps

We recall that (Schneider & Weiss 1992)

$$\hat{\mu} = (\det\hat{A})^{-1}, \quad \hat{\mu} = b^2\mu, \qquad (9)$$

$$\det A = b^2 \det\hat{A} = b^2[\hat{x}_1 + (3s-1)\hat{x}_2^2]. \qquad (10)$$

Consider the magnifications for different images of one point inside the cusp. We show below that the following equality is valid for all sources inside the cusp

$$\hat{\mu}^{(1)} + \hat{\mu}^{(2)} + \hat{\mu}^{(3)} = 0. \qquad (11)$$

It is clear from Eq.(11) that we have the statement of Schneider & Weiss (1992) that

$$|\hat{\mu}^{(1)}| = |\hat{\mu}^{(2)} + \hat{\mu}^{(3)}|. \qquad (12)$$

It should be mentioned that Eq. (11) follows from Schneider and Weiss Eq.(2.3) (Eq. (12) of our paper) plus their comment on the parities after their Eq.(2.33b). We use the following expression for magnifications

$$\mu^{(i)} = \frac{1}{\hat{x}_1^{(i)} + (3s-1)(\hat{x}_2^{(i)})^2} \tag{13}$$

or using Eq.(7)

$$\mu^{(i)} = \frac{2}{S[\tilde{y}_1 - (\hat{x}_2^{(i)})^2]} \tag{14}$$

Therefore it is necessary to prove that

$$\frac{1}{\tilde{y}_1 - (\hat{x}_2^{(1)})^2} + \frac{1}{\tilde{y}_1 - (\hat{x}_2^{(2)})^2} + \frac{1}{\tilde{y}_1 - (\hat{x}_2^{(3)})^2} = 0 \tag{15}$$

or that

$$3\tilde{y}_1^2 - 2\tilde{y}_1[(\hat{x}_2^{(1)})^2 + (\hat{x}_2^{(2)})^2 + (\hat{x}_2^{(3)})^2] + \\ +[(\hat{x}_2^{(1)}\hat{x}_2^{(2)})^2 + (\hat{x}_2^{(1)}\hat{x}_2^{(3)})^2 + (\hat{x}_2^{(2)}\hat{x}_2^{(3)})^2] = 0. \tag{16}$$

Vieta's theorem applied to Eq.(8) yields

$$\hat{x}_2^{(1)} + \hat{x}_2^{(2)} + \hat{x}_2^{(3)} = 0,$$
$$\hat{x}_2^{(1)}\hat{x}_2^{(2)} + \hat{x}_2^{(1)}\hat{x}_2^{(3)} + \hat{x}_2^{(2)}\hat{x}_2^{(3)} = -3\tilde{y}_1.$$

If we express the symmetric power polynomials in terms of symmetric elementary polynomials we have

$$(\hat{x}_2^{(1)})^2 + (\hat{x}_2^{(2)})^2 + (\hat{x}_2^{(3)})^2 = 6\tilde{y}_1, \tag{17}$$
$$(\hat{x}_2^{(1)}\hat{x}_2^{(2)})^2 + (\hat{x}_2^{(1)}\hat{x}_2^{(3)})^2 + (\hat{x}_2^{(2)}\hat{x}_2^{(3)})^2 = 9\tilde{y}_1^2, \tag{18}$$

Thus we obtain (16). Similarly we have

$$q_1 = \hat{\mu}^{(1)}\hat{\mu}^{(2)}\hat{\mu}^{(3)} = \frac{2}{(3S)^3(\tilde{y}_1^3 - \tilde{y}_2^2)}, \tag{19}$$

$$p_1 = \hat{\mu}^{(1)}\hat{\mu}^{(2)} + \hat{\mu}^{(1)}\hat{\mu}^{(3)} + \hat{\mu}^{(2)}\hat{\mu}^{(3)} = \frac{-3\tilde{y}_1}{(3S)^2(\tilde{y}_1^3 - \tilde{y}_2^2)}. \tag{20}$$

Therefore we get an equation of third degree for the magnification of different images of a point inside the cusp

$$\tilde{\mu}^3 + \tilde{p}_1\tilde{\mu} + \tilde{q}_1 = 0, \tag{21}$$

where $\tilde{\mu} = \hat{\mu}/S, \tilde{p}_1 = p_1(3S)^2, \tilde{q}_1 = q_1(3S)^3$. If $\tilde{y}_1^3 > \tilde{y}_2^2$ then the discriminant for the pure cubic equation

$$D = \left(\frac{\tilde{p}_1}{3}\right)^3 + \left(\frac{\tilde{q}_1}{2}\right)^2 = \frac{-\tilde{y}_2^2}{(\tilde{y}_1^3 - \tilde{y}_2^2)^3}$$

is negative and we have three solutions of the Eq.(21) (see for example, Bronstein & Semendjajew 1980). Namely, we have

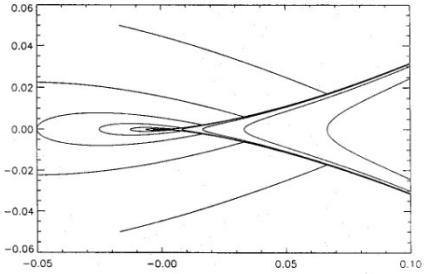

Fig. 1. Magnification contours around a cusp for the sum of absolute values of magnifications of all images. The contour levels are $10 * 2^i, -1 \le i \le 14$

for a point inside the cusp region

$$\tilde{\mu}^{(1)} = -\frac{2}{3}\sqrt{\frac{\tilde{y}_1}{\tilde{y}_1^3 - \tilde{y}_2^2}}\cos\left\{\frac{\cos^{-1}\left[\sqrt{\frac{\tilde{y}_1^3 - \tilde{y}_2^2}{\tilde{y}_1^3}}\right]}{3}\right\}, \tag{22}$$

$$\tilde{\mu}^{(2)} = -\frac{2}{3}\sqrt{\frac{\tilde{y}_1}{\tilde{y}_1^3 - \tilde{y}_2^2}}\cos\left\{\frac{\cos^{-1}\left[\sqrt{\frac{\tilde{y}_1^3 - \tilde{y}_2^2}{\tilde{y}_1^3}}\right]}{3} + \frac{2\pi}{3}\right\}, \tag{23}$$

$$\tilde{\mu}^{(3)} = -\frac{2}{3}\sqrt{\frac{\tilde{y}_1}{\tilde{y}_1^3 - \tilde{y}_2^2}}\cos\left\{\frac{\cos^{-1}\left[\sqrt{\frac{\tilde{y}_1^3 - \tilde{y}_2^2}{\tilde{y}_1^3}}\right]}{3} + \frac{4\pi}{3}\right\} \tag{24}$$

and we have only one solution for a point outside the cusp region

$$\tilde{\mu}^{(1)} = \frac{\sqrt[3]{\sqrt{\tilde{y}_2^2 - \tilde{y}_1^3} + \tilde{y}_2} + \sqrt[3]{\sqrt{\tilde{y}_2^2 - \tilde{y}_1^3} - \tilde{y}_2}}{\sqrt{\tilde{y}_2^2 - \tilde{y}_1^3}}. \tag{25}$$

It is possible to calculate the magnifications of the images from the direct solution of the gravitational lens equation near a cusp. Namely, we solve Eq.(8) and use Eqs.(7),(9),(10). After that we also obtain the expressions for magnifications.

4. Discussion

In Fig. 1 we present the contours for the sum of absolute values of magnifications of images near the cusp. Note that the algebraic sum of the values is equal to zero and that there are three real solutions of the gravitational lens equation in the cusp region. The contours are plotted by using expressions (22-25). It is possible to compare Fig. 1 with the similar figure from Schneider & Weiss (1992) that was obtained using the ray - shooting method (see, for example, Wamsganss 1990). Figure 1 shows clearly the cusp type singularity.

The Astrophysical Journal, 690:1772–1796, 2009 January 10 doi:10.1088/0004-637X/690/2/1772

EXTENDED-SOURCE EFFECT AND CHROMATICITY IN TWO-POINT-MASS MICROLENSING

Ondřej Pejcha[1] and David Heyrovský
Institute of Theoretical Physics, Charles University, Prague, Czech Republic; pejcha@astronomy.ohio-state.edu, and heyrovsky@utf.mff.cuni.cz
Received 2007 December 7; accepted 2008 September 11; published 2008 December 30

ABSTRACT

We explore the sensitivity of two-point-mass gravitational microlensing to the extended nature of the source star, as well as the related sensitivity to its limb darkening. We demonstrate that the sensitive region, usually considered to be limited to a source-diameter-wide band along the caustic, is strongly expanded near cusps, most prominently along their outer axis. In the case of multicomponent caustics, facing cusps may form a region with a non-negligible extended-source effect spanning the gap between them. We demonstrate that for smaller sources the size of the sensitive region extending from a cusp measured in units of source radii increases, scaling as the inverse cube root of the radius. We study the extent of different sensitivity contours and show that for a microlensed Galactic bulge giant the probability of encountering at least a 1% extended-source effect is higher than the probability of caustic crossing by 40–60% when averaged over a typical range of lens-component separations, with the actual value depending on the mass ratio of the components. We derive analytical expressions for the extended-source effect and chromaticity for a source positioned off the caustic. These formulae are more generally applicable to any gravitational lens with a sufficiently small source. Using exactly computed amplifications we test the often used linear-fold caustic approximation and show that it may lead to errors on the level of a few percent even in near-ideal caustic-crossing events. Finally, we discuss several interesting cases of observed binary and planetary microlensing events and point out the importance of our results for the measurement of stellar limb darkening from microlensing light curves.

Key words: binaries: general – gravitational lensing – planetary systems – stars: atmospheres

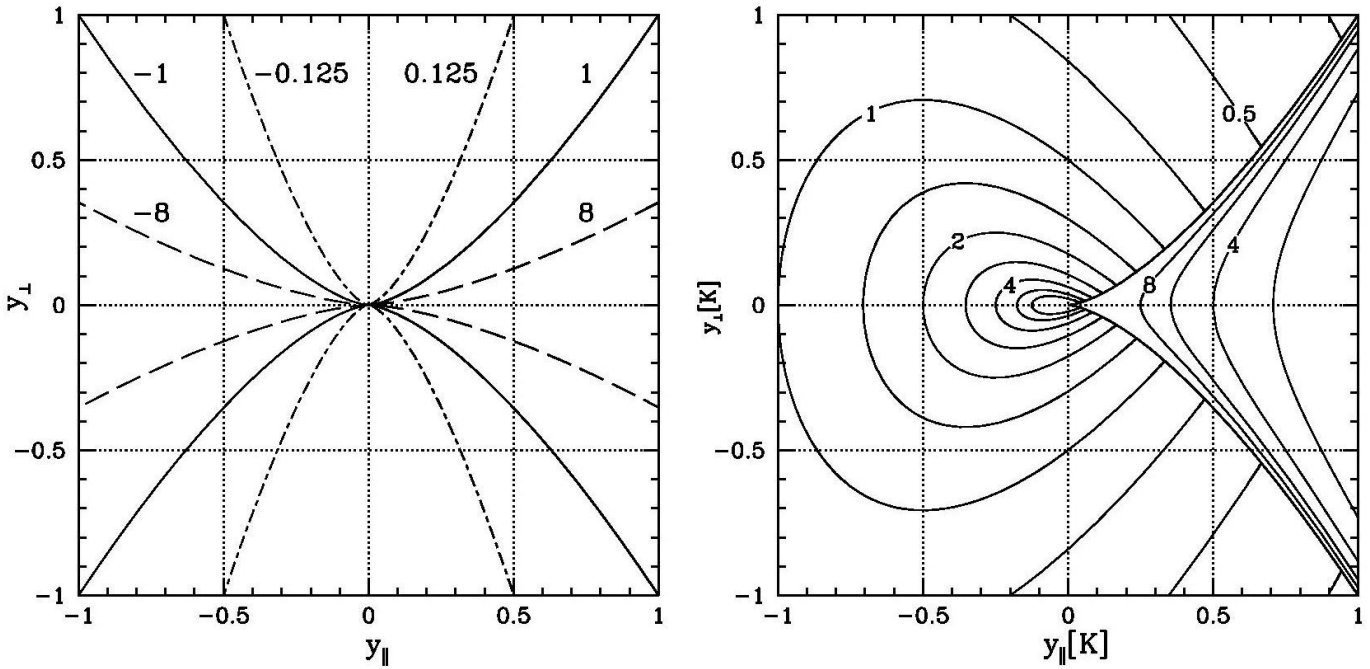

Figure 16. Geometry of a generic cusp caustic given by Equation (A2). Left panel: cusps for six values of K, with $K > 0$ curves drawn bold and $K < 0$ thin. Cusps with $|K| = 1$, 8, and 0.125 are marked by solid, dashed, and dot-dashed lines, respectively. Right panel: amplification contours for lensing by a generic cusp (bold curve). Contour values in units of $|K\,b\,|^{-1}$ are spaced by a factor of $2^{1/2}$; outside the cusp levels range from the outermost $2^{-3/2}$ to the innermost 2^3, inside the cusp from the rightmost $2^{3/2}$ to the leftmost 2^3. With axes marked in units of K, the right panel is valid for an arbitrary cusp.

We thank the referee, Scott Gaudi, for his helpful comments and constructive suggestions. Work on this project was supported by the Czech Science Foundation grant GACR 205/07/0824 and by the Czech Ministry of Education project MSM0021620860.

APPENDIX

AMPLIFICATION OF IMAGES FORMED BY A CUSP

As shown by Schneider & Weiß (1992), the lens equation

a function of the image position (Schneider & Weiß 1992). Zakharov (1995, 1999) presented an elegant alternative method for obtaining image amplifications as a function of the source position, without explicitly solving the lens equation. From the general properties of the roots of the image equation, Zakharov derived a simple cubic equation for the amplification, the roots of which are the amplifications of the images. We reproduce the main results here because of a few typos appearing in the original papers. A point source satisfying $y_\perp^2 < K^{-1} y_\parallel^3$ lies

If we introduce $\vec{\theta} := \vec{\xi}/D_d, \vec{\beta} = \vec{\eta}/D_s$ then the magnification of GL mapping is

$$\mu := \frac{\Delta\omega}{\Delta\omega_0} := \left|\det \frac{\partial\vec{\beta}}{\partial\vec{\theta}}\right|^{-1} = \left|\det \frac{\partial\vec{y}}{\partial\vec{x}}\right|^{-1} \qquad (11)$$

and

$$\mu_\pm = \frac{1}{4}\left(\frac{y}{\sqrt{4+y^2}} + \frac{\sqrt{4+y^2}}{y} \pm 2\right). \qquad (12)$$

Therefore,

$$\mu_{\text{total}} = \mu_+ + \mu_- = \frac{y^2+2}{y(y^2+4)^{1/2}}, \qquad (13)$$

thus $\mu_{\text{total}} \to 1/y$ (for $y \to 0$) and $\mu_{\text{total}} \to 1 + 1/y^4$ (for $y \to \infty$).

If $M \sim M_\odot$ and $D_d \sim 10$ kpc then

$$\theta_0 = 0.902\text{mas}\left(\frac{M}{M_\odot}\right)^{1/2}\left(\frac{10\text{ kpc}}{D_d}\right)\left(1 - \frac{D_d}{D_s}\right)^{1/2};$$

and angular velocity

$$\dot{\theta} = \frac{d\theta}{dt} = 4.22\left(\frac{v}{200\text{ km/s}}\right)\left(\frac{10\text{ kpc}}{D_d}\right)\frac{\text{mas}}{\text{yr}}. \qquad (14)$$

Therefore a typical duration is

$$t_0 = \frac{\theta_0}{\dot{\theta}} = .214\left(\frac{M}{M_\odot}\right)^{1/2}\left(\frac{D_d}{10\ kpc}\right)^{1/2} \times \qquad (15)$$

$$\times\left(1 - \frac{D_d}{D_s}\right)^{1/2}\left(\frac{200\text{ km/s}}{v}\right)\text{yr}. \qquad (16)$$

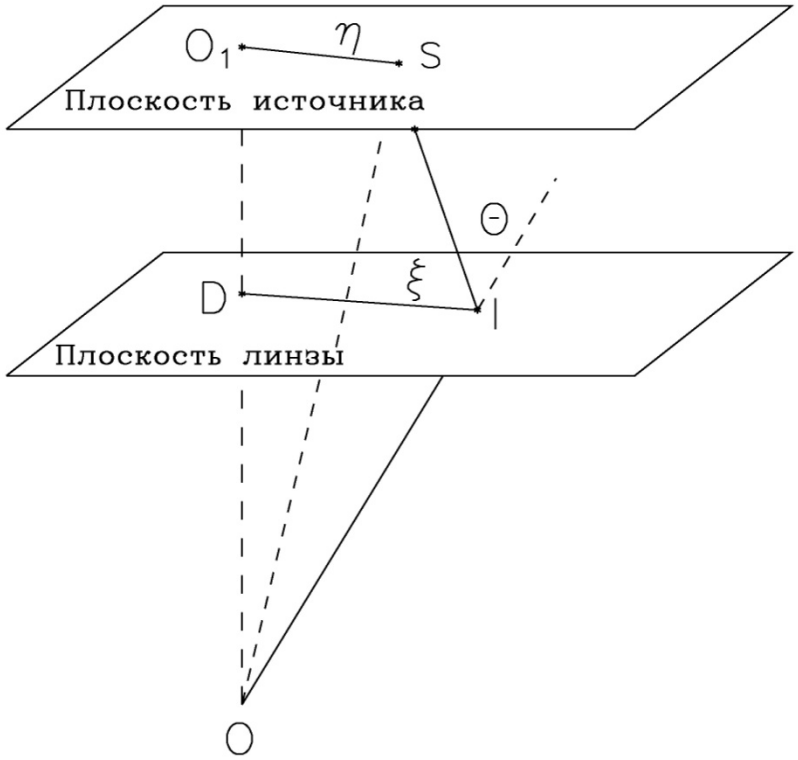
O1
η
S
Плоскость источника
Θ
ξ
D
I
Плоскость линзы
O

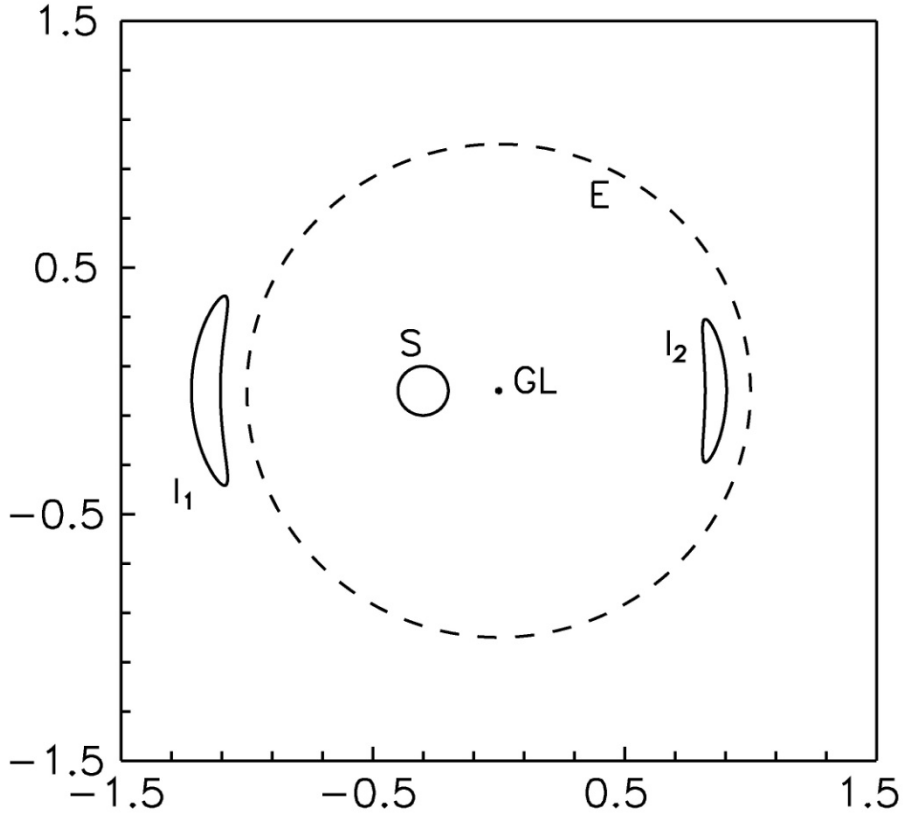
1.5
0.5
−0.5
−1.5
−1.5
−0.5
0.5
1.5
E
S
GL
I1
I2

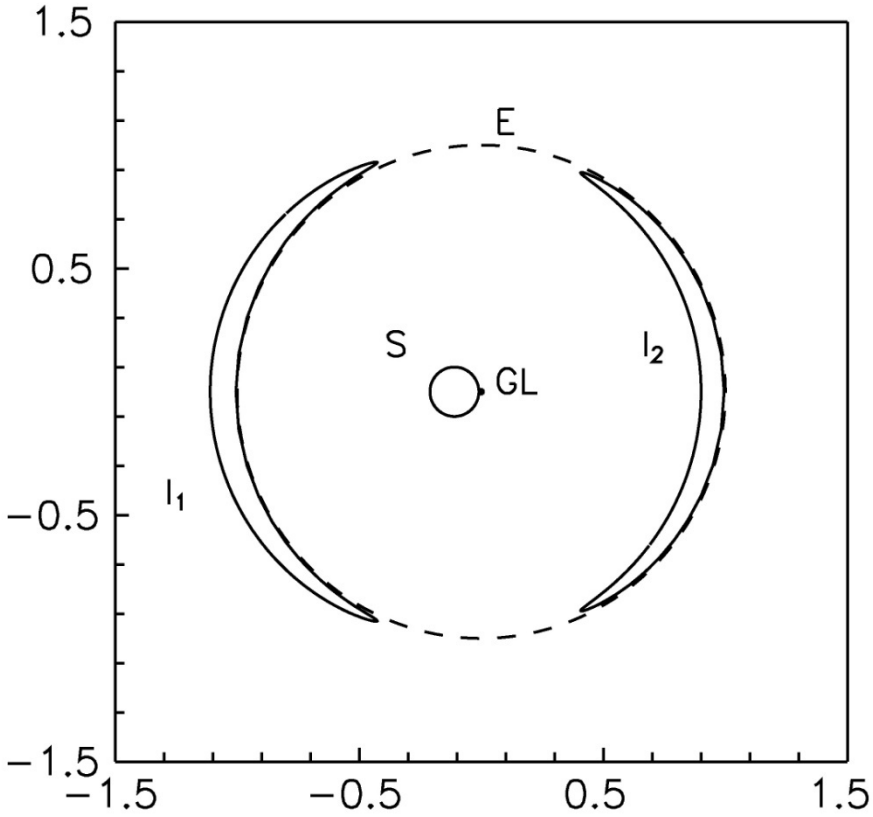
1.5
0.5
−0.5
−1.5
−1.5
−0.5
0.5
1.5
E
S
GL
I_1
I_2

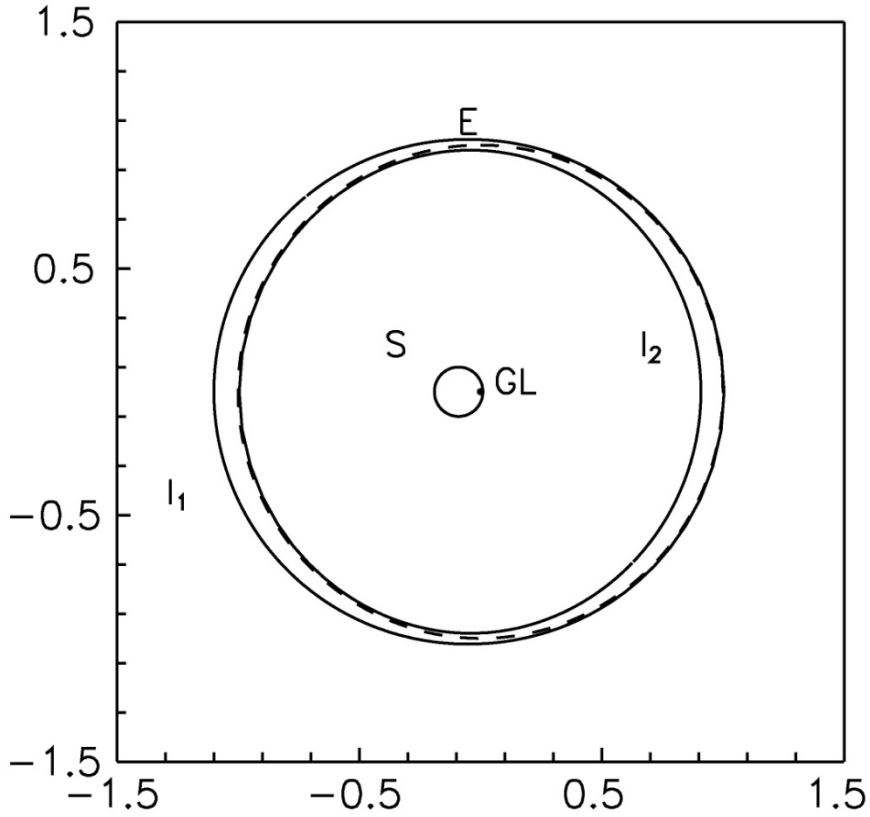
1.5
0.5
−0.5
−1.5
−1.5
−0.5
0.5
1.5
E
S
GL
I2
I1

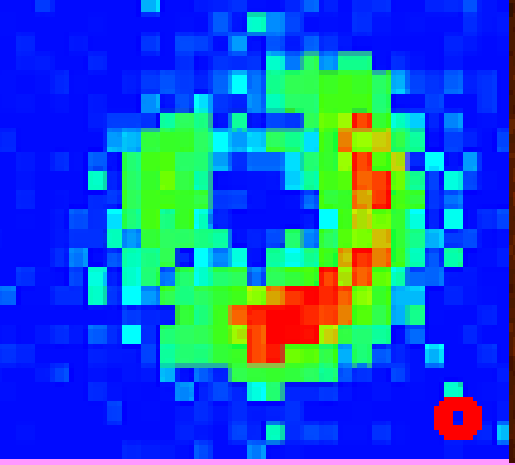
o

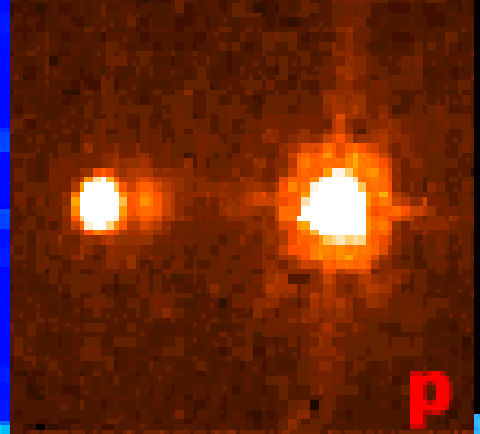
p

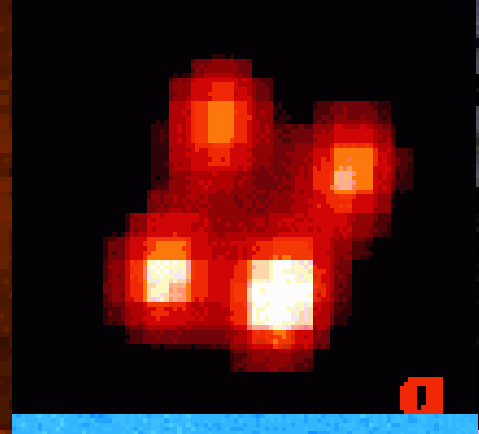
q

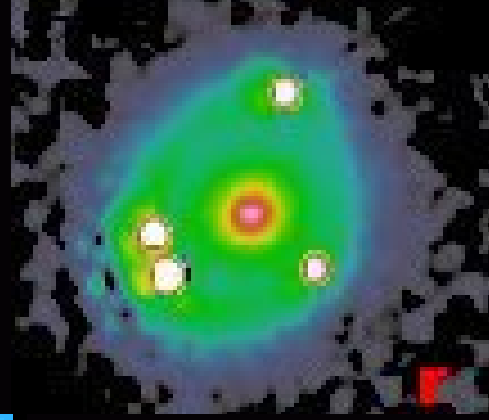
r

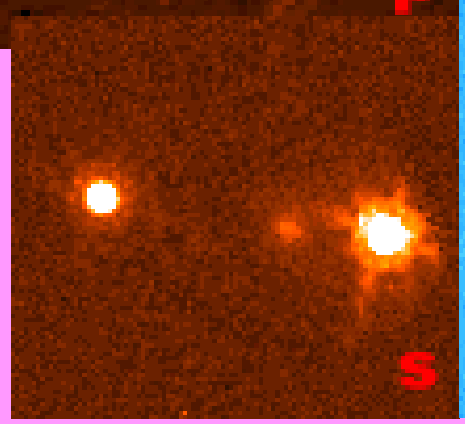
s

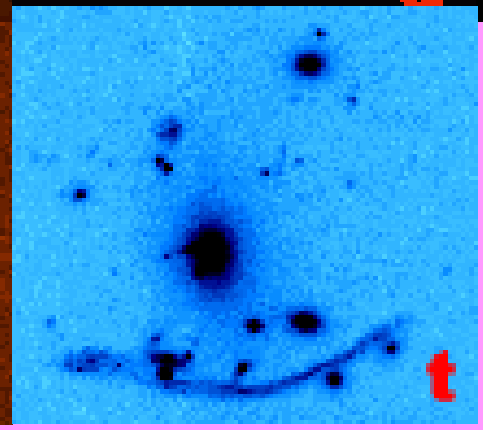
t


u

MG J0414+0534

- QSO 2237+0305
  “Крест Эйнштейна”

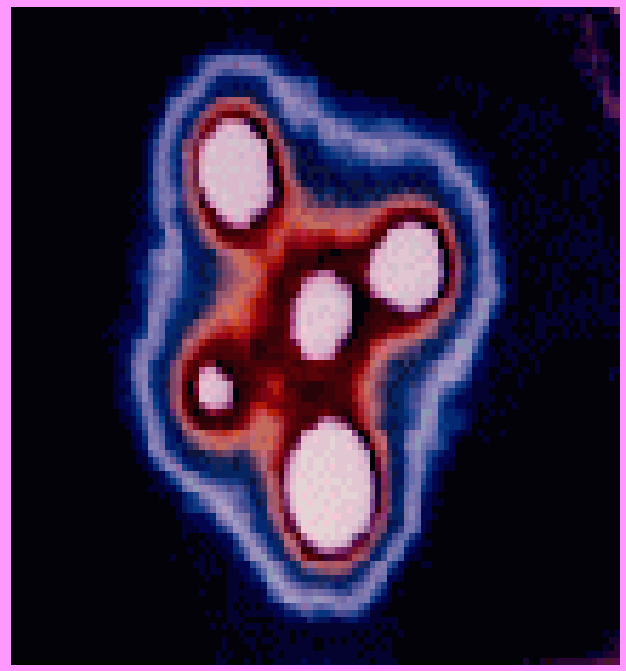

MG J0414+0534

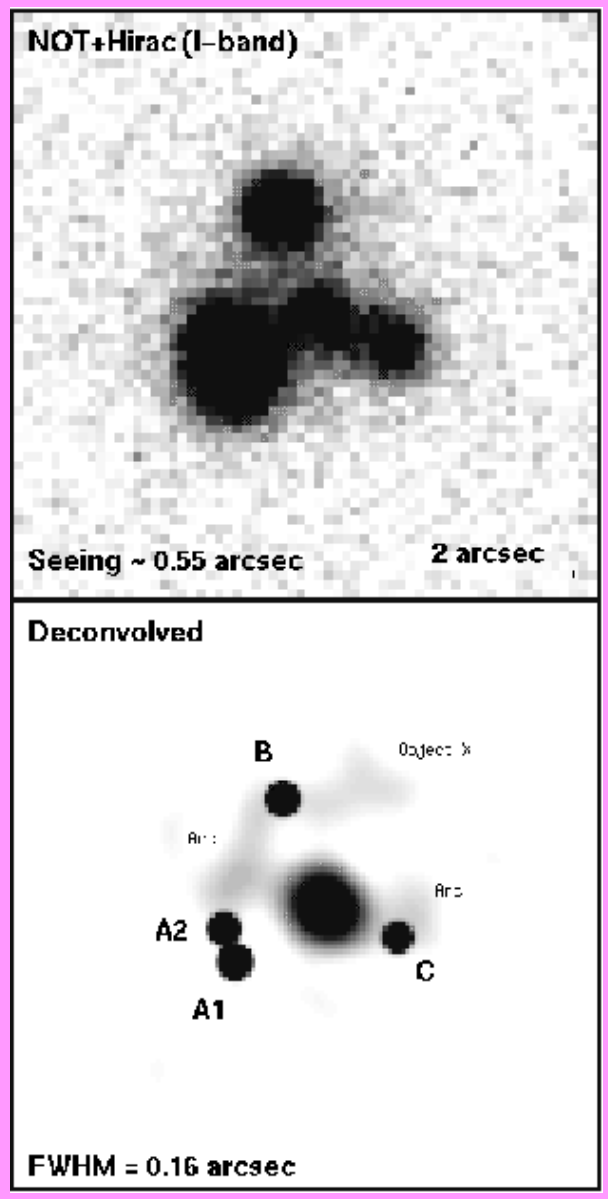

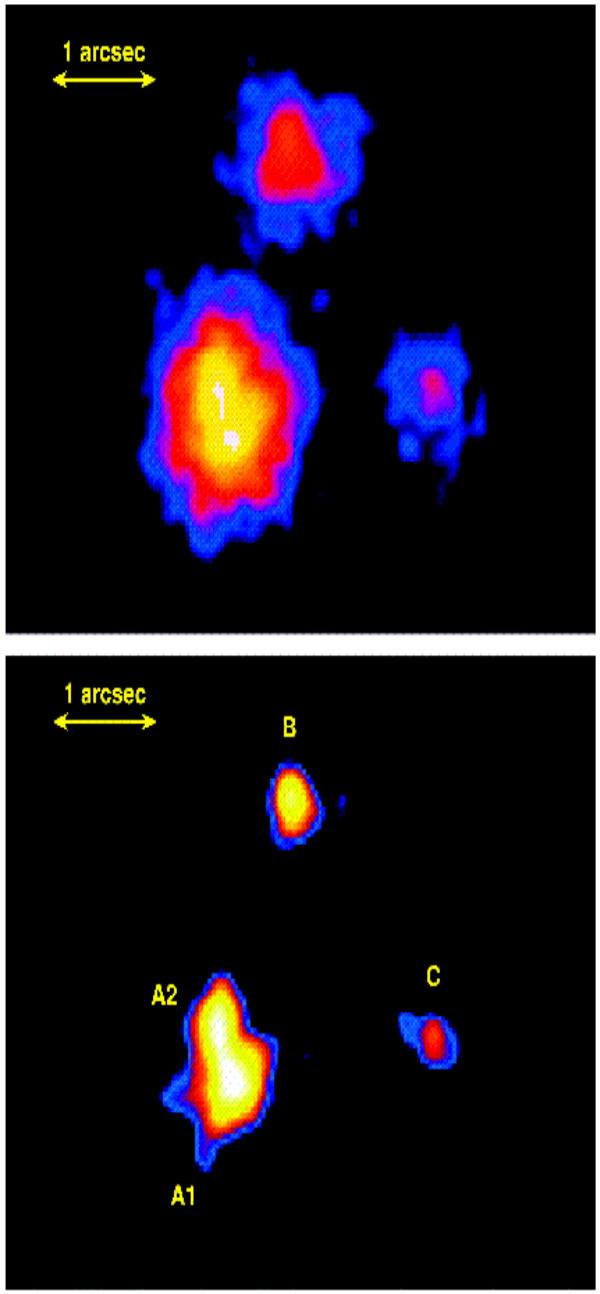

FIG. 1.—*Top panel*: Combined image of five *Chandra* observations of MG J0414+0534. *Bottom panel*: Deconvolved image of combined *Chandra* observations.

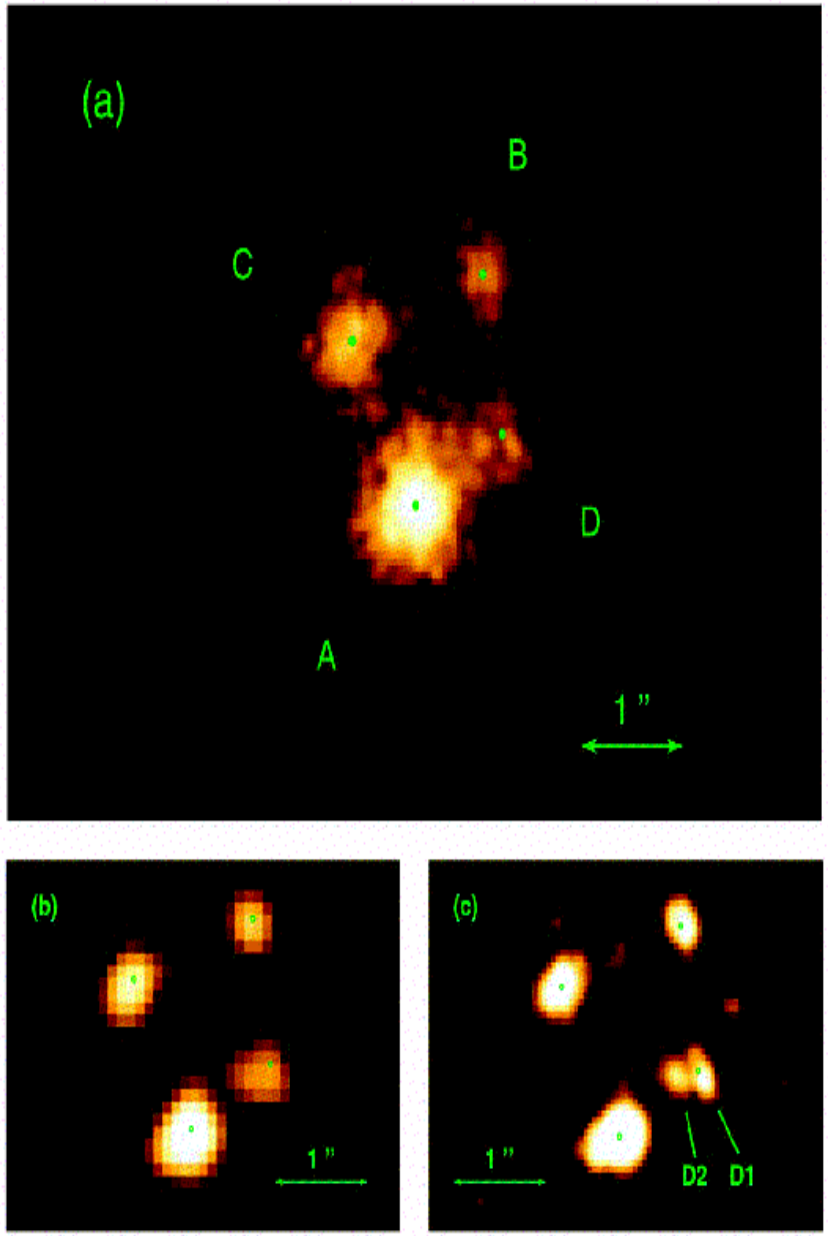

FIG. 1.—(*a*) Raw image of the combined observations of Q2237−0305 binned with a bin size of 0.″05 and smoothed with a Gaussian of 0.″05. (*b*) Deconvolved image binned with a bin size of 0.″1. (*c*) Deconvolved image binned with a bin size of 0.″05. The green circles in each image are the corresponding *HST* image positions provided by CASTLES.

The Astrophysical Journal, 637:620–630, 2006 February 1

A STUDY OF THE CORRELATION BETWEEN THE AMPLIFICATION OF THE Fe Kα LINE AND THE X-RAY CONTINUUM OF QUASARS DUE TO MICROLENSING

L. Č. Popović,[1,2] P. Jovanović,[1,2] E. Mediavilla,[3] A. F. Zakharov,[4,5,6] C. Abajas,[3] J. A. Muñoz,[3,7] and G. Chartas[8]

Received 2005 March 4; accepted 2005 October 4

ABSTRACT

The observed enhancement of the Fe Kα line in three gravitationally lensed QSOs (MG J0414+0534, QSO 2237+0305, and H1413+117) is interpreted in terms of microlensing, even when equivalent X-ray continuum amplification is not observed. In order to interpret these observations, first we studied the effects of microlensing on quasar spectra produced by a straight fold caustic crossing over a standard relativistic accretion disk. The disk emission was analyzed using the ray-tracing method, considering Schwarzschild and Kerr metrics. When the emission is separated into two regions (an inner disk corresponding to the Fe Kα line and an outer annulus corresponding to the continuum, or vice versa), we find microlensing events that enhance the Fe Kα line without noticeable amplification of the X-ray continuum, but only during a limited time interval. Continuum amplification is expected if a complete microlensing event is monitored. Second, we studied a more realistic case of amplification by a caustic magnification pattern. In this case we could satisfactorily explain the observations if the Fe Kα line is emitted from the innermost part of the accretion disk while the continuum is emitted from a larger region. We also studied the chromatic effects of microlensing, finding that the radial distribution of temperature in the accretion disk, combined with microlensing itself, can induce wavelength-dependent variability of $\sim$30% for microlenses with very small masses. All these results show that X-ray monitoring of gravitational lenses is a method well suited for studying the innermost structure of active galactic nucleus accretion disks.

Subject headings: gravitational lensing — quasars: individual (H1413+117, MG J0414+0534, QSO 2237+0305) — X-rays: galaxies

1. INTRODUCTION

Recent observational and theoretical studies suggest that gravitational microlensing can induce variability in the X-ray emission of lensed QSOs. Microlensing of the Fe Kα line has been reported in at least three macrolensed QSOs: MG J0414+0534 (Chartas et al. 2002), QSO 2237+0305 (Dai et al. 2003), and H1413+117 (Oshima et al. 2001b; Popović et al. 2003b; Chartas et al. 2004).

The influence of microlensing in the X-ray emission has been also theoretically investigated. Mineshige et al. (2001) simulated the variation of the X-ray continuum due to microlensing, showing that the flux magnifications for the X-ray and optical continuum emission regions are not significantly different during the microlensing event, while Yonehara et al. (1998, 1999) and Takahashi et al. (2001) found that simulated spectral variations caused by microlensing show different behavior, depending on photon energy. Also, microlensed light curves for thin accretion disks around Schwarzschild and Kerr black holes were considered in Jaroszyński et al. (1992), and microlensing light curves for the Fe Kα were simulated by Jaroszyński (2002). On the other hand, the influence of microlensing in the Fe Kα spectral line shape was discussed in Popović et al. (2001b, 2003a, 2003b) and Chartas et al. (2002).[9] Popović et al. (2003a, 2003b) showed that objects in a foreground galaxy with even relatively small masses can produce observable changes in the Fe Kα line flux much stronger than those expected for the UV and optical lines (Popović et al. 2001a; Abajas et al. 2002; Lewis & Ibata 2004). In the optical spectra, microlensing induced magnification of broad UV lines (e.g., C IV and S IV/O IV) was reported by Richards et al. (2004). Consequently, one can expect that microlensing of the Fe Kα line region will be more frequent. Observations of the X-ray continuum and the Fe Kα line in multi-imaged active galactic nuclei (AGNs) open new possibilities for the study of the unresolved X-ray–emitting structure in QSOs, particularly for high-redshift QSOs (Zakharov et al. 2004; Dai et al. 2004).

However, an explanation for the different behavior of the line and continuum variability in the observed events should be given in context of the microlensing hypothesis. Chartas et al. (2002) detected an increase of the Fe Kα equivalent width in image B of the lensed QSO J0414+0534 that was not followed by the continuum. Chartas et al. (2002) explained the nonenhancement of the continuum emission in the spectrum of image B by proposing that the thermal emission region of the disk and the Compton upscattered emission region of the hard X-ray source lie within smaller radii than the iron line reprocessing region. Analyzing the X-ray variability of QSO 2237+0305A, Dai et al. (2003) also measured amplification of the Fe Kα line in component A of QSO

[1] Astronomical Observatory, Volgina 7, 11160 Belgrade 74, Serbia.
[2] Isaac Newton Institute of Chile, Yugoslavia Branch, and Universidad Diego Portales, Chile.
[3] Instituto de Astrofisica de Canarias, 382005 La Laguna, Tenerife, Spain.
[4] Institute of Theoretical and Experimental Physics, 25, B. Cheremushkinskaya st., Moscow, 117259, Russia.
[5] Astro Space Centre of Lebedev Physics Institute, Moscow, Russia.
[6] Isaac Newton Institute of Chile, Moscow Branch.

[9] Simulations of X-ray line profiles are presented in a number of papers; see, for example, Fabian (2001) and Zakharov & Repin (2002a, 2002b, 2002c)

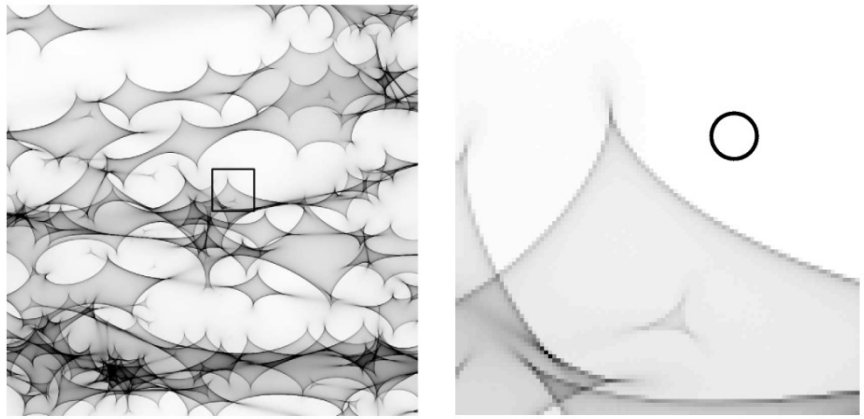

FIG. 2.—*Left:* Microlensing map of QSO 2237+0305A image with 16 ERR ($177,372R_g$) on a side (Abajas et al. 2005). *Right:* A small part (*square in the left panel*) of the microlensing pattern, compared to a face-on accretion disk. The assumed outer radius of the disk is $R_{out} = 1000R_g$.

of the caustic crossing and microlens mass. In the following subsections we choose and discuss the parameters used in the calculations.

2.2.1. *Accretion Disk Parameters*

For the disk inclination we adopt the averaged values given by Nandra et al. (1997) from a study of the Fe Kα line profiles of 18 Seyfert 1 galaxies: $i = 35°$. The inner radius, R_{in}, cannot be smaller than the radius of the marginally stable orbit, R_{ms}, that corresponds to $R_{ms} = 6R_g$ (gravitational radii $R_g = GM/c^2$, where G is gravitational constant, M is the mass of central black hole, and c is the velocity of light) in the Schwarzschild metric and to $R_{ms} = 1.23R_g$ in the case of the Kerr metric with angular momentum parameter $a = 0.998$. To select the outer radius, R_{out}, we take into account previous investigations of the X-ray variability that support very compact X-ray–emitting disks. In particular, Oshima et al. (2001a) infer from the observed variation in the lensed blazar PKS 1830−211 a size of the X-ray continuum emission region of $\sim 3 \times 10^{14}$ cm, which is in agreement with the estimation for QSO 2237+03050 given by Dai et al. (2003). So, considering a range of black hole masses of 10^7–$10^9\ M_\odot$ we can conclude that the X-ray emission is coming from a compact region of the order of $10R_g$–$100\ R_g$. This range of sizes is also acceptable for the Fe Kα emission region (see, e.g., Nandra et al. 1997, 1999).

To explore the suitability of the various hypotheses explaining the lack of adequate response of the X-ray continuum to the microlensing events detected in the Fe Kα line (see § 1), we consider several combinations of disk sizes for the emitters of both the continuum and the line: (1) the inner and outer radii of both emission regions are the same, $R_{in} = R_{ms}$ and $R_{out} = 20\ R_g$; (2) the inner radius is the same, $R_{in} = R_{ms}$, but the outer radius of the X-ray continuum disk is smaller, $R_{out} = 20R_g$, than the radius of the line emission disk, $R_{out} = 80R_g$; (3) the continuum emission disk has radii $R_{in} = R_{ms}$ and $R_{out} = 20R_g$, and the line emission disk has $R_{in} = 20R_g$ and $R_{out} = 80R_g$ (the continuum emission takes place in an inner part of disk surrounded by an annulus of Fe Kα emission); (4) the continuum emission disk has radii $R_{in} = 20R_g$ and $R_{out} = 80R_g$, and the line emission disk has $R_{in} = R_{ms}$ and $R_{out} = 20R_g$ (the Fe Kα emission is located in the inner disk and the continuum emission in the outer annulus).

We adopt the central object mass from Bian & Zhao (2002). We assume a black hole of mass $M_8 = 10^8\ M_\odot$. We use this value in order to determine the effective temperature distribution. This value is in agreement with Wang et al. (2003), where it was found that the majority of QSOs have black hole masses in the range of 10^8–$10^9\ M_\odot$.

It is difficult to discuss the validity of different emissivity laws for demonstrating the X-ray emission (in the line as well as in the continuum), but sometimes, as for example in the case of

TABLE 1

PROJECTED ERR FOR DIFFERENT DEFLECTOR MASSES FOR THE THREE LENSED QSOS WHERE MICROLENSING OF THE Fe Kα LINE IS SUSPECTED

Object	z_s	z_l	$1 \times 10^{-4}\ M_\odot$	$1 \times 10^{-3}\ M_\odot$	$1 \times 10^{-2}\ M_\odot$	$1 \times 10^{-1}\ M_\odot$	$1\ M_\odot$
MG J0414+0534	2.64	0.96	20.3	64.2	203.1	642.3	2031.1
QSO 2237+0305	1.69	0.04	11.2	35.4	112.1	354.5	1121.0
QSO H1413+117	2.56	1.00	19.8	62.5	197.7	625.2	1977.0

NOTES.—Expressed in gravitational radii. The three QSOs are J0414+0534 (Chartas et al. 2002), QSO H1413+117 (Oshima et al. 2001b; Chartas et al. 2004), and QSO 2237+0305 (Dai et al. 2003). The values used for the cosmological constants are $H_0 = 50$ km s^{-1} Mpc^{-1} and $\Omega_0 = 1$. The black hole mass is assumed to be $10^8\ M_\odot$.

figures does the continuum remain strictly constant during a complete Fe Kα microlensing event. In the most favorable case (the inner Fe Kα disk plus an outer continuum annulus; Figs. 6 and 7), we achieve a significant and relatively quick change of the Fe Kα emission while the continuum experiences only a slow increase. This behavior could well approximate a nonvarying continuum, but only if we consider observations in a temporal window that fall on the peak of the microlensing event in the Fe Kα line. In this case the continuum of the microlensed image experiences an (slowly changing or almost constant) amplification with respect to the continua of the other images, but practically it is indistinguishable from the amplifications due to global macrolensing.

3.3. *Microlensing by a Caustic Magnification Pattern: An Example for Q2237+0305A Image*

Here we consider a situation where a low-mass population of microlenses (smaller than one solar mass) can form pattern structures (see Table 1) that are comparable with the size of the X-ray accretion disk. Moreover, the black hole mass of the lensed quasar may be of the order of 10^9–10^{10} $M_\odot$, taking that $R_g \sim M_{\rm BH}$, the pattern structure of low-mass microlenses are comparable with a X-ray disk size of several dozen R_g. Therefore, here we consider that the black hole mass of the lensed quasar is 10^9 $M_\odot$.

For modeling of the caustic magnification pattern for image Q2237+0305A we used the same values for the convergence and external shear as presented in Figure 2, but for a low-mass population, taking that the mass of the deflectors are randomly distributed in an interval ranging from 0.1 to 0.6 $M_\odot$, with a mean value of $\langle m \rangle = 0.35$ $M_\odot$. Also, the positions of the lenses were distributed randomly in a rectangular region in the lens plane, significantly larger than the considered region in the source plane. Now, 1 ERR projected in the source plane corresponds to

$$\mathrm{ERR}(M) = \mathrm{ERR}(M_\odot)\sqrt{\frac{M}{M_\odot}\frac{M_8}{M_{\rm BH}}},$$

where $\mathrm{ERR}(M_\odot) = 0.054$ pc is the projected ERR for a solar mass deflector, M is the mean mass of the deflectors, and $M_{\rm BH}$ is the blackhole mass. Taking the mean deflector mass as $\langle m \rangle = 0.35$ $M_\odot$ and $R_g = 9.547.10^{-6}$ $M_{\rm BH}/M_8$ pc, we modeled a caustic magnification pattern of 1 ERR × 2 ERR, that corresponds to $334.63R_g \times 669.26R_g$ in the source plane for a black hole mass of $M_{\rm BH} = 10^9$ $M_\odot$ (Fig. 9). For numerical reasons, the microlens magnification map is given in pixels, 1000 × 2000 (1 pixel = $0.33463R_g$ in source plane). As one can see from Figure 9, the microlensing pattern structures are comparable with a compact X-ray accretion disk.

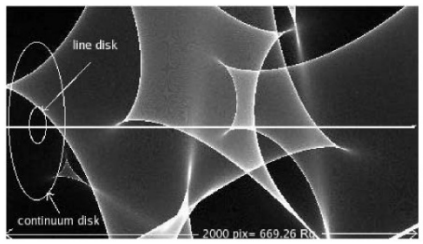

FIG. 9.—Microlensing map of QSO 2237+0305A image with 1 ERR × 2 ERR (1000 pixel × 2000 pixel = $334.63R_g \times 669.26R_g$) on a side and scheme of the projected disk with outer radius $R_{\rm out} = 20R_g$ and $100R_g$ for the Fe Kα line and the X-ray continuum, respectively. The straight line presents the path of the center of the disk (the left side of the pattern corresponds to 0 pixels).

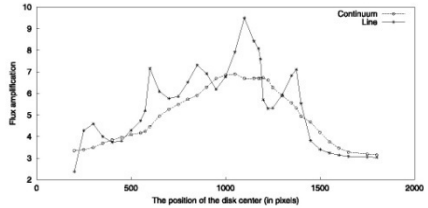

FIG. 10.—Amplification of the Fe Kα line and the X-ray continuum total flux for different positions of the center on the microlensing map of QSO 2237+0305A image (see Fig. 9).

In our previous modeling based on the straight fold caustic approximation the lack of a correlation between the continuum and Fe Kα line is expected only if the line and X-ray continuum region are separated. Recent investigations of the Fe Kα line profile from active galaxies show that the line should be emitted from the innermost part of the accretion disk. In particular, Ballantyne & Fabian (2005) found that in BLRG 4C+74.26 the outer radius of the relativistic iron line should be within $10R_g$. Consequently, here we assume that the Fe Kα line is formed in the innermost part of the disk ($R_{\rm in} = R_{\rm ms}$ and $R_{\rm out} = 20R_g$) and that the continuum (emitted in the energy range between 0.1 and 10 keV) is mainly originated from a larger region ($R_{\rm in} = 20R_g$ and $R_{\rm out} = 100R_g$).[10] On the other hand, from the straight fold caustic modeling we conclude that the correlation between the total line and continuum flux due to microlensing is not very different for different emissivity laws. Consequently, here we used the blackbody emissivity law. A disk (Schwarzschild metric) with an inclination of 35° is considered.

To explore the line and X-ray continuum variation we moved the disk center along the microlensing map as shown in Figure 9 (going from 0 to 2000 pixels, from left to right). In Figure 10 we present the corresponding total line and X-ray continuum flux variation. As one can see from Figure 10, there is a global correlation between the total line and continuum flux during the complete path. However, the total continuum flux variation is smooth and has a monotonic change, while the total line flux varies very strongly and randomly.

In fact, during some portion of the microlensing of the emission regions by the magnification pattern, we found the total Fe Kα line flux changes, while the continuum flux remains nearly constant (e.g., the position of the disk center between 1000 and 1200 pixels). This and the shapes of the line and continuum total flux amplification indicate that the observed microlensing amplification of the Fe Kα in three lensed quasars may be explained if the line is originated in the innermost part of the disk and the X-ray continuum in a larger region. Also, it

[10] Note that here, taking the continuum disk size from $R_{\rm in} = 20R_g$ to $R_{\rm out} = 100R_g$, we neglected the contribution of the innermost part emission (from $R_{\rm ms}$ to $20R_g$) to the total continuum flux only in the energy interval from 0.1 to 10 keV. It does not mean that there is no the continuum emission.

Mon. Not. R. Astron. Soc. **386,** 397–406 (2008) doi:10.1111/j.1365-2966.2008.13036.x

Microlensing of the X-ray, UV and optical emission regions of quasars: simulations of the time-scales and amplitude variations of microlensing events

P. Jovanović,[1]★ A. F. Zakharov,[2,3,4] L. Č. Popović[1] and T. Petrović[1]

[1]*Astronomical Observatory, Volgina 7, 11160 Belgrade, Serbia*
[2]*Institute of Theoretical and Experimental Physics, B. Cheremushkinskaya 25, Moscow 117259, Russia*
[3]*Bogoliubov Laboratory for Theoretical Physics, JINR, 141980 Dubna, Russia*
[4]*Centre of Advanced Mathematics and Physics, National University of Science and Technology, Rawalpindi, Pakistan*

Accepted 2008 January 28. Received 2008 January 28; in original form 2007 March 26

ABSTRACT

We consider the influence of microlensing on different spectral bands of lensed QSOs. We assumed that the emitting X-ray, ultraviolet (UV) and optical regions are different in size, but that the continuum emission in these spectral bands is originating from an accretion disc. Estimations of the time-scales for microlensing and flux amplification in different bands are given. We found that the microlensing duration should be shorter in the X-ray (several months) than in UV/optical emitting region (several years). This result indicates that monitoring of the X-ray variations in lensed QSOs that show a 'flux anomaly' can clarify the source of this anomaly.

Key words: accretion, accretion discs – gravitational lensing – galaxies: active – ultraviolet: galaxies – X-rays: galaxies.

1 INTRODUCTION

Recent observational and theoretical studies suggest that gravitational microlensing can induce variability not only in optical light, but also in the X-ray emission of lensed QSOs (Popović et al. 2001; Chartas et al. 2002; Dai et al. 2003; Chartas et al. 2004; Dai et al. 2004; Jovanović 2006; Popović et al. 2003a, 2003b, 2006a,b). Variability studies of QSOs indicate that the size of the X-ray emitting region is significantly smaller (∼ several light-hours), than the optical and ultraviolet (UV) emitting regions (∼ several light-days).

Gravitational lensing is achromatic (the deflection angle of a light ray does not depend on its wavelength), but it is clear that if the geometries of the emitting regions at different wavelengths are different then chromatic effects could occur. For example, if the microlens is a binary star or if the microlensed source is extended (Griest & Hu 1992, 1993; Bogdanov & Cherepashchuk 1995a,b; Zakharov 1997; Zakharov & Sazhin 1998; Popović & Chartas 2005) different amplifications in different spectral bands can be present. Studies aiming to determine the influence of microlensing on the spectra of lensed QSOs need to take into account the complex structure of the QSO central emitting region (Popović & Chartas 2005). Since the sizes of the emitting regions are wavelength dependent, microlensing by stars in the lens galaxy may lead to a wavelength-dependent magnification. For example, Blackburne, Pooley & Rappaport (2006) reported such a 'flux anomaly' in quadruply imaged quasar 1RXS J1131−1231. In particular, they found discrepancies between the X-ray and optical flux ratio anomalies. Such anomalies in the different spectral band flux ratios can be attributed to microlensing or millilensing in the massive lensing halo. In the case of millilensing one can infer the nature of substructure in the lensing galaxy, which can be connected to cold dark matter (CDM) structures (see e.g. Dobler & Keeton 2006). Besides microlensing, there are several mechanisms which can produce flux anomalies, such as extinction and intrinsic variability. These anomalies were discussed in Popović & Chartas (2005) where the authors gave a method that can aid in distinguishing between variations produced by microlensing from ones resulting from other effects. In this paper we discuss consequences of variations due to gravitational microlensing, in which the different geometries and dimensions of emitting regions of different spectral bands are considered.

The influence of microlensing on QSO spectra emitted from their accretion discs in the range from the X-ray to the optical spectral band is analysed. Moreover, assuming different sizes of the emitting regions, we investigate the microlensing time-scales for those regions, as well as a time-dependent response in amplification of different spectral bands due to microlensing. Also, we give the estimates of microlensing time-scales for a sample of lensed QSOs.

In Section 2, we describe our model of the quasar emitting regions and a model of the microlens. In Section 3 we discuss the time-scales of microlensing and in Section 4 we present our results. Finally, in Section 5, we draw our conclusions.

★E-mail: pjovanovic@aob.bg.ac.yu

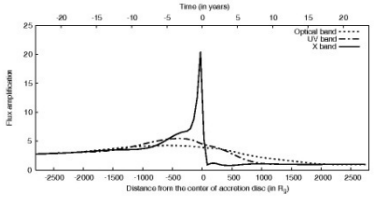

Figure 2. The variations of normalized total continuum flux in optical (3500–7000 Å), UV (1000–3500 Å) and X (1.24–12.4 Å, i.e. 1–10 KeV) band due to microlensing by a caustic crossing along $y = -x$ direction in the case of Schwarzschild metric. Time-scale corresponds to 'typical' redshifts of microlens and source: $z_l = 0.5$ and $z_s = 2$. The parameters of the caustic are: $A_0 = 1$, $\beta = 1$, $\kappa = +1$ and its 'size' is $9000\,R_g$. Negative distances and times correspond to the approaching side, and positive to the receding side of accretion disc. In this case, due to $\kappa = +1$, caustic motion is from the receding towards the approaching side (i.e. from the right- to left-hand side). The source mass is $10^8\,M_\odot$. The radii of optical emitting region are: $R_{in} = 100\,R_g$, $R_{out} = 2000\,R_g$, for UV emitting region: $R_{in} = 100\,R_g$, $R_{out} = 1000\,R_g$ and for X-ray-emitting region: $R_{in} = R_{ms}$, $R_{out} = 80\,R_g$.

3 TYPICAL TIME-SCALES FOR MICROLENSING

Typical scales for microlensing are discussed not only in books on gravitational lensing (Schneider, Ehlers & Falco 1992; Zakharov 1997; Petters, Levine & Wambsganss 2001), but in recent papers also (see e.g. Treyer & Wambsganss 2004). In this paper we discuss microlenses located in gravitational macrolenses (stars in lensing galaxies), since optical depth for microlensing is then the highest (Wyithe & Turner 2002a,b; Zakharov, Popović & Jovanović 2004, 2005) in comparison with other possible locations of gravitational microlenses, as for example stars situated in galactic clusters and extragalactic dark haloes (Tadros, Warren & Hewett 1998; Inoue & Chiba 2003; Totani 2003).

Assuming the concordance cosmological model with $\Omega_{tot} = 1, \Omega_{matter} = 0.3$ and $\Omega_\Lambda = 0.7$ we recall that typical length-scale for microlensing is (Treyer & Wambsganss 2004):

$$R_E = \sqrt{2 r_s \frac{D_s D_{ls}}{D_l}} \approx 3.2 \times 10^{16} \sqrt{\frac{m}{M_\odot}} h_{75}^{-0.5}\ \mathrm{cm}, \tag{10}$$

where 'typical' microlens and sources redshifts are assumed to be $z_l = 0.5, z_s = 2$. (similar to Treyer & Wambsganss 2004), $r_s = 2Gm/c^2$ is the Schwarzschild radius corresponding to microlens mass m, $h_{75} = H_0/[(75\,\mathrm{km\,s^{-1}})\,\mathrm{Mpc^{-1}}]$ is dimensionless Hubble constant.

The corresponding angular scale is (Treyer & Wambsganss 2004)

$$\theta_0 = \frac{R_E}{D_s} \approx 2.2 \times 10^{-6} \sqrt{\frac{m}{M_\odot}} h_{75}^{-0.5}\ \mathrm{arcsec}. \tag{11}$$

Using the length-scale (10) and velocity scale (say $v_\perp \sim 600\,\mathrm{km\,s^{-1}}$ as Treyer & Wambsganss 2004 did), one could calculate the standard time-scale corresponding to the scale to cross the projected Einstein radius

$$t_E = (1 + z_l) \frac{R_E}{v_\perp} \approx 25 \sqrt{\frac{m}{M_\odot}} v_{600}^{-1} h_{75}^{-0.5}\ \mathrm{yr}, \tag{12}$$

where a relative transverse velocity $v_{600} = v_\perp/(600\,\mathrm{km\,s^{-1}})$. The time-scale t_E, corresponding to a point-mass lens and to a small source (compared to the projected Einstein radius of the lens), could be used if microlenses are distributed freely at cosmological distances and if each Einstein angle is located far enough from another one. However, the estimation (12) gives long and most likely overestimated time-scales especially for gravitationally lensed systems. Thus we must apply another microlens model to estimate time-scales.

For a simple caustic model, such as one that considers a straight-fold caustic,[1] there are two time-scales depending either on the 'caustic size' ($r_{caustic}$) or the source radius (R_{source}). In the case when source radius is larger or at least close to the 'caustic size' ($R_{source} \gtrsim r_{caustic}$), the relevant time-scale is the 'crossing time' (Treyer & Wambsganss 2004):

$$\begin{aligned} t_{cross} &= (1 + z_l) \frac{R_{source}}{v_\perp (D_s/D_l)} \\ &\approx 0.69\ R_{15}\ v_{600}^{-1} \left(\frac{D_s}{D_l}\right)^{-1} h_{75}^{-0.5}\ \mathrm{yr} \\ &\approx 251\ R_{15}\ v_{600}^{-1}\ h_{75}^{-0.5}\ \mathrm{d}, \end{aligned} \tag{13}$$

where D_l and D_s correspond to $z_l = 0.5$ and $z_s = 2$, respectively, and $R_{15} = R_{source}/10^{15}$ cm. As a matter of fact, the velocity perpendicular to the straight-fold caustic characterizes the time-scale and it is equal to $v_\perp \sin\beta$ where β is the angle between the caustic and the velocity $v_\perp$ in the lens plane, but in our rough estimates we can omit factor $\sin\beta$ which is about unity. However, if the source radius R_{source} is much smaller than the 'caustic size' $r_{caustic}$ ($R_{source} \ll r_{caustic}$), one could use the 'caustic time', i.e. the time when the source is located in the area near the caustic:

$$\begin{aligned} t_{caustic} &= (1 + z_l) \frac{r_{caustic}}{v_\perp (D_s/D_l)} \\ &\approx 0.69\ r_{15}\ v_{600}^{-1} \left(\frac{D_s}{D_l}\right)^{-1} h_{75}^{-0.5}\ \mathrm{yr} \\ &\approx 251\ r_{15}\ v_{600}^{-1}\ h_{75}^{-0.5}\ \mathrm{d}, \end{aligned} \tag{14}$$

where $r_{15} = r_{caustic}/10^{15}$ cm.

Therefore, t_{cross} could be used as a lower limit for typical time-scales in the case of a simple caustic microlens model. From equations (13) and (14) it is clear that one cannot unambiguously infer the source size R_{source} from variability measurements alone, without making some further assumptions. In general, however, we expect that t_{cross} corresponds to smaller amplitude variations than $t_{caustic}$, since in the first case only a fraction of a source is significantly amplified by a caustic (due to assumption that $R_{source} \gtrsim r_{caustic}$), while in the second case it is likely that the entire source could be strongly affected by caustic amplification (due to assumption that $R_{source} \ll r_{caustic}$).

In this paper, we estimated the microlensing time-scales for the X-ray, UV and optical emitting regions of the accretion disc using the following three methods.

(i) By converting the distance scales of microlensing events to the corresponding time-scales according to the formula (13) in which R_{source} is replaced by the distance from the centre of accretion disc. Caustic rise times (t_{HME}) are then derived from the simulated variations of the normalized total flux in the X-ray, UV and optical

[1] We use the following approximation for the extra magnification near the caustic: $\mu = \sqrt{r_{caustic}/(\xi - \xi_c)}$, $\xi > \xi_c$ where ξ is the perpendicular direction to the caustic-fold (it is obtained from equation 4 assuming that factor K is about unity).

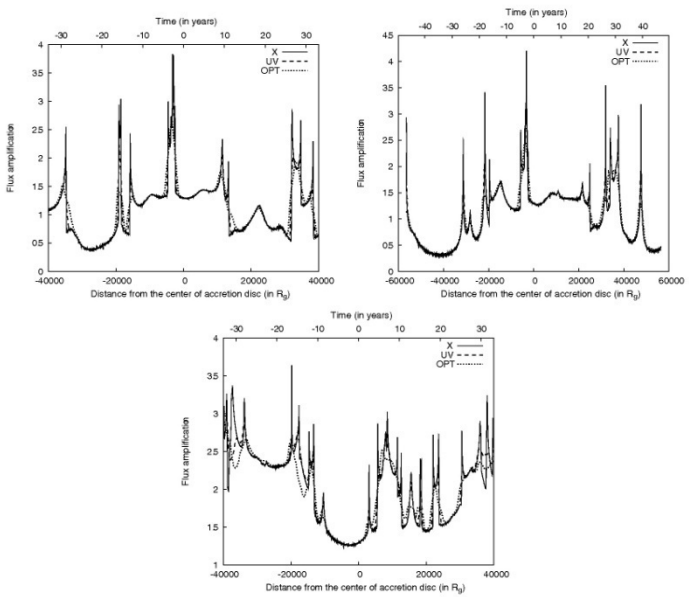

Figure 5. Variations in the X-ray (solid), UV (dashed) and optical (dotted) spectral bands corresponding to the horizontal (top left-hand panel), diagonal (top right-hand panel) and vertical (bottom panel) path in the magnification map of the QSO 2237+0305A (Fig. 1, left-hand panel).

HMEs are asymmetric peaks in the light curves which depend not only on microlens parameters but also on the sizes of emitting regions in the following sense: the larger emitting regions are expected to produce smoother light curves and more symmetric peaks (Witt et al. 1995). Consequently, it can be expected that the majority of HMEs should be detected in X-ray light curves, less of them in UV and the smallest number in optical light curves. Therefore, we isolated only clearly asymmetric peaks in all light curves and measured their rise times $t_{\rm HME}$ as the intervals between the beginning and the maximum of the corresponding microlensing events. In the case of Q2237+0305A we found the following number of HMEs: (i) horizontal path: 13 in X-ray, eight in UV and seven in optical band, (ii) diagonal path: 10 in X-ray, seven in UV and five in optical band and (iii) vertical path: 22 in X-ray, 12 in UV and six in optical band. In case of 'typical' lens these numbers are: (i) horizontal path: 21 in X-ray, 10 in UV and eight in optical band, (ii) diagonal path: 30 in X-ray, nine in UV and seven in optical band and (iii) vertical path: 18 in X-ray, seven in UV and four in optical band.

The average number of caustic crossings per unit length ($\langle N_{\rm caustic}\rangle_0$) and per year ($\langle N_{\rm caustic}\rangle_y$) are given in Table 2. This table also contains the average rise times ($\langle t_{\rm HME}\rangle$) in all three spectral bands, derived from the rise times ($t_{\rm HME}$) of individual HMEs which are presented in Figs 8 and 9 in the form of histograms. These results, as expected, show that the rise times are the shortest and the frequency of caustic crossings is the highest in the X-ray spectral band in comparison to the other two spectral bands. One can also see from Tables 1 and 2 that in the case of Q2237+0305A, the average rise times of HMEs for all three spectral bands (obtained from microlens magnification pattern simulations) are longer than both caustic rise times (obtained from caustic simulations) and caustic times (calculated from equation 14).

Microlensing can result in flux anomalies in the sense that different image flux ratios are observed in different spectral bands (Popović & Chartas 2005; Popović et al. 2006b). As shown in Figs 2–6, the amplification in the X-ray band is larger and lasts shorter than it does in the UV and optical bands. Consequently, monitoring of lensed QSOs in the X-ray and UV/optical bands can clarify whether the flux anomaly is produced by CDM clouds, massive black holes or globular clusters (millilensing) or stars in foreground galaxy (microlensing).

5 CONCLUSION

In this paper we calculated microlensing time-scales of different emitting regions. Using a model of an accretion disc (in the centre of lensed QSOs) that emits in the X-ray and UV/optical spectral bands, we calculated the variations in the continuum flux caused by a straight-fold caustic crossing an accretion disc. We also simulated crossings of accretion discs over microlensing magnification patterns for the case of image A of Q2237+0305 and for a 'typical' lens system. From these simulations we conclude the following:

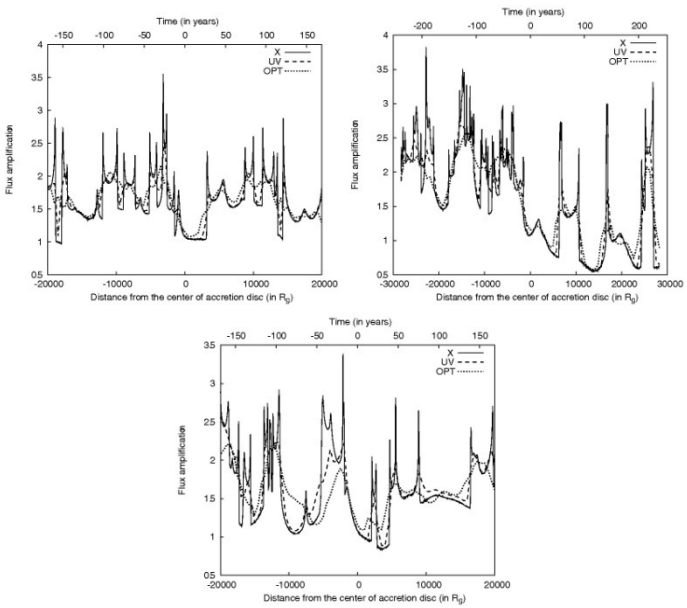

Figure 6. The same as in Fig. 5 but for the magnification map of a 'typical' lens system (Fig. 1, right-hand panel).

Table 1. The estimated time-scales (in years) for microlensing of the X-ray, UV and optical emission region for lensed QSOs observed by *Chandra X-ray Observatory* (Dai et al. 2004). The calculated caustic times $t_{\rm caustic}$ are obtained according to formula (14) for the following values of the cosmological constants: $H_0 = 75\,{\rm km\,s^{-1}\,Mpc^{-1}}$ and $\Omega_0 = 0.3$. The caustic rise times $t_{\rm HME}$ are derived from caustic crossing simulations (see Figs 2–4). The black hole mass is assumed to be $10^8\,{\rm M}_\odot$.

Object	z_s	z_l	X-ray		UV		Optical	
			$t_{\rm caustic}$	$t_{\rm HME}$	$t_{\rm caustic}$	$t_{\rm HME}$	$t_{\rm caustic}$	$t_{\rm HME}$
HS 0818+1227	3.115	0.39	0.572	0.660	7.147	7.070	14.293	15.160
RXJ 0911.4+0551	2.800	0.77	0.976	1.120	12.200	12.080	24.399	25.880
LBQS 1009−0252	2.740	0.88	1.077	1.240	13.468	13.330	26.935	28.570
HE 1104−1805	2.303	0.73	0.918	1.050	11.479	11.370	22.957	24.350
PG 1115+080	1.720	0.31	0.451	0.520	5.634	5.570	11.269	11.950
HE 2149−2745	2.033	0.50	0.675	0.780	8.436	8.350	16.871	17.890
Q 2237+0305	1.695	0.04	0.066	0.080	0.828	0.820	1.655	1.760

(i) One can expect that the X-ray radiation is more amplified than UV/optical radiation due to microlensing which can induce the so called 'flux anomaly' of lensed QSOs.

(ii) The typical microlensing time-scales for the X-ray band are of the order of several months, while for the UV/optical they are of the order of several years (although the time-scales obtained from microlensing magnification pattern simulations are longer in comparison to those obtained from caustic simulations).

(iii) Monitoring of the X-ray emission of lensed QSOs can reveal the nature of 'flux anomaly' observed in some lensed QSOs.

All results obtained in this work indicate that monitoring the X-ray emission of lensed QSOs is useful not only to discuss the nature of the 'flux anomaly', but also can be used for constraining the size of the emitting region.

ACKNOWLEDGMENTS

This work is a part of the project (146002) 'Astrophysical Spectroscopy of Extragalactic Objects' supported by the Ministry of

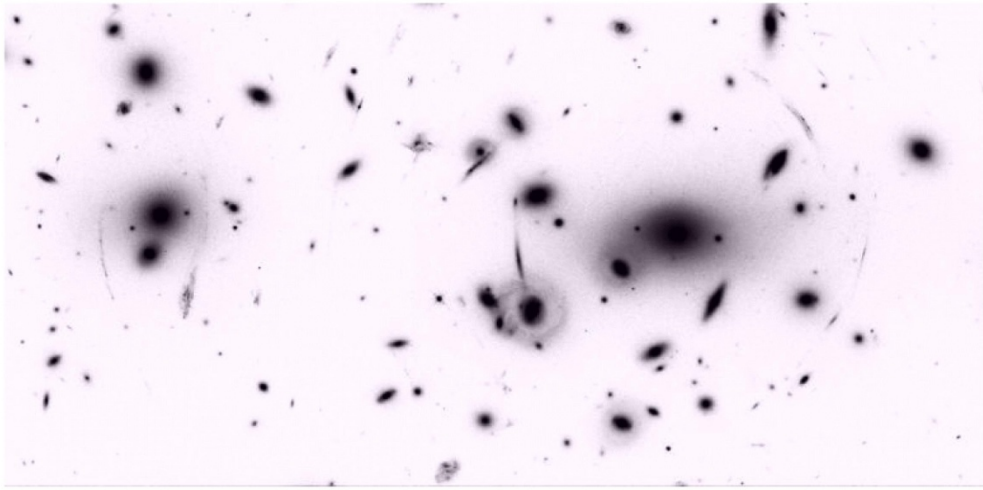

SOVIET ASTRONOMY – AJ VOL. 13, NO. 5 MARCH-APRIL, 1970

FOCUSING OF RADIATION BY A GRAVITATIONAL FIELD

A. V. Byalko

L. D. Landau Institute of Theoretical Physics, Academy of Sciences of the USSR

Translated from Astronomicheskii Zhurnal, Vol. 46, No. 5,
pp. 998-1002, September-October, 1969
Original article submitted July 15, 1967;
revision submitted April 11, 1969

A discussion is given of the focusing effect of gravitating bodies due to the curvature in the trajectory of light rays passing near them. The intensity distribution is derived for radiation passing close to a spherically symmetric body in the geometric- and wave-optics approximations. The possibilities of observing the effect are examined. The conditions most favorable for detection would be the observation of a distant radio source through the galactic-center region.

According to Einstein, a light ray passing near a spherically symmetric body whose gravitational radius $r_g = 2Gm/c^2$ will be deflected toward the center of the body by the small angle

$$\alpha = 2r_g / h, \tag{1}$$

where h is the distance of closest approach, m is the mass of the body, c is the velocity of light, and G is the gravitational constant. Radiation will therefore appear to be focused by the deflecting body, which will act like a gravitational lens.

We wish to consider only the case where the distance a to the source is much greater than the distance b from the observer to the lens. We shall introduce cylindrical coordinates z, r, φ, with origin at the center of the deflecting body and the axis directed away from the source. Then in the geometry-optics approximation, as Einstein showed [1], the intensity of the radiation from the point source at the point of observation (z = b, r = ξ) will be given by the expression

$$q = \frac{I}{I_0} = \frac{2+p}{\sqrt{p(p+4)}} = \frac{4r_g b + \xi^2}{\xi\sqrt{8r_g b + \xi^2}}, \tag{2}$$

where I_0 is the intensity of the incident flux and $p = \xi^2/2r_g b$ is a dimensionless parameter.

This expression has a singularity at $\xi = 0$, which appears because a point source is assumed and the geometric-optics approximation is adopted.

1. The influence of an extended source has been investigated by Refsdal [2], who has obtained series expansions of the intensity distribution. We shall give a more accurate equation below.

A surface element r dr dφ of a source with brightness B(r, φ) will yield at the point of observation an intensity (geometric optics)

$$dI = \frac{B(r,\varphi)}{a^2} r\,dr\,d\varphi \frac{4r_g b + \eta^2}{\eta\sqrt{8r_g b + \eta^2}}, \tag{3}$$

where $\eta = \sqrt{\xi^2 - 2\frac{b}{a}\xi\cos\varphi + \frac{r^2 b^2}{a^2}}$ is the distance from the point of observation to the central projection of the given surface element on the plane z = b. The total intensity is obtained by integrating over the surface of the source.

If the angular diameter of the source is not too great, the influence of its extended area will be sigficant only for small ξ. For a star of radius s with a constant surface brightness B = const (a Lambert source), we obtain, for $\xi^2 \ll r_g b$,

$$q = \frac{I}{I_0} = \frac{\sqrt{2r_g b}}{s'}\Phi\left(\frac{\xi}{s'}\right). \tag{4}$$

Evidently the asymptotic form of Eq. (14), as $k \to \infty$, with an average taken over the rapidly oscillating square of the cosine, will give an expression coinciding with Eq. (2) for $\xi^2 \ll r_g b$:

$$q = \frac{\sqrt{2r_g b}}{\xi} \cdot 2\cos^2\left(k\xi\sqrt{\frac{2r_g}{b}} - \frac{\pi}{4}\right) \to \frac{\sqrt{r_g b}}{\xi}. \quad (15)$$

It is now evident that in order for Eq. (12) to be applicable the characteristic length $l = \pi/k(b \cdot 2r_g)^{-1/2}$ of the oscillations in the diffraction pattern must be much greater than the blurring due to the extension of the source; that is,

$$k\frac{s}{a}\sqrt{r_g b} \ll 1. \quad (16)$$

This condition may be considered satisfied for observations of quasars ($s/a < 10^{-12}$) in the radio range ($k < 10^{-2}$ cm^{-1}) if the stars ($r_g \approx 10^5$ cm) of our galaxy ($b < 10^{23}$ cm) are regarded as the lenses.

3. We turn now to the probability of detecting the effect. Two different observational processes are conceivable. In the first procedure one would follow a lens star and note any intensity variations as the line joining the lens to the observer passes near a distant source.

The second method would consist in observing a distant source and recording bursts in intensity when objects are encountered along the line of sight, even though they themselves may be invisible.

Einstein [1] had pointed out that it was unlikely the effect would be detectable. Refsdal [2] has discussed in detail the probability of observing it by the first method.

Let us consider the probability of an observation by the second method. Suppose that the parameters of the source are given, together with the requisite statistical properties of the medium through which the source is observed. We shall first obtain the probability dw of observing a burst of intensity $g \pm dq/2$ in the geometric-optics case. Starting with Einstein's equation, Eq. (1), we obtain

$$\frac{dw}{dq} = \left|\frac{dp}{dq}\right| \frac{dw}{dp} = \frac{2}{(q^2-1)^{1/2}} \frac{dw}{dp}, \quad (17)$$

where dw/dp is the probability distribution of the quantity $p = \xi^2/2r_g b$.

In particular, let $\partial\nu/\partial r_g(r_g, b)dr_g dV$ represent the number of bodies with a gravitational radius $r_g \pm dr_g/2$ in a volume $dV = 2\pi\xi d\xi db$ about a point located at a distance b from the observer.

The ordinary density $\mu(b)$ is related to this distribution function as follows:

$$\mu(b) = \frac{c^2}{2G}\int_0^\infty \frac{\partial\nu}{\partial r_g} r_g\, dr_g. \quad (18)$$

We shall assume single scattering, as will be confirmed by the result. Then the probability dw that $\xi^2/2r_g b$ will fall in the range $p \pm dp/2$ will be

$$dw = \int_{p < \frac{\xi^2}{2r_g b} < p+dp} \frac{\partial\nu}{\partial r_g} dr_g\, 2\pi\xi\, d\xi\, db$$

$$= dp \int \frac{\partial\nu}{\partial r_g} r_g\, dr_g\, 2\pi b\, db. \quad (19)$$

Finally, the distribution function of the intensity bursts for the geometric-optics case becomes

$$dw/dq = \frac{8\pi G}{c^2}\int \mu(b)\, b\, db\, 1/(q^2-1)^{3/2}. \quad (20)$$

The integration should extend over the region for which the initial equation is valid. In practice this reduces to an integration along a ray within our galaxy.

One important property of the distribution is the fact that it is not normalized. This circumstance is not accidental, however, but occurs because the gravitational focusing increases the total flux: the intensity in the Einstein equation does not have a minimum with respect to ξ. In other words, unlike an ordinary lens a gravitational lens does not redistribute the flux, but "intensifies" it.

This apparent paradox is readily understood. In fact, the ray is deflected because of the change in the metric near the lens; in particular, the surface of the sphere is no longer equal to $4\pi r^2$ but to a smaller value, causing an increase in the flux.

The distribution (20) enables us to compute the mean value of an intensity burst:

$$\langle q - 1\rangle = \frac{8\pi G}{c^2}\int \mu(b)\, b\, db \sim 10^{-5}.$$

In evaluating the integral the density has been considered constant along the entire diameter of

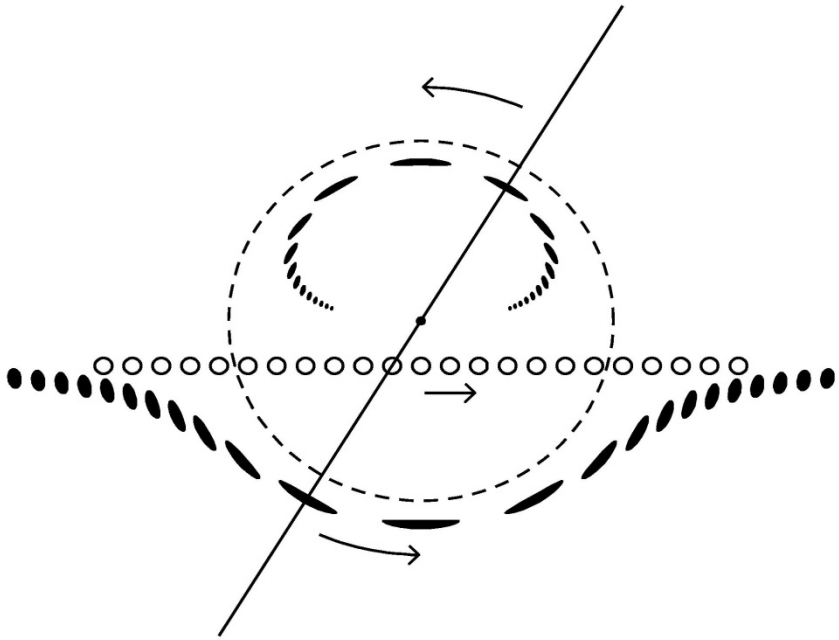

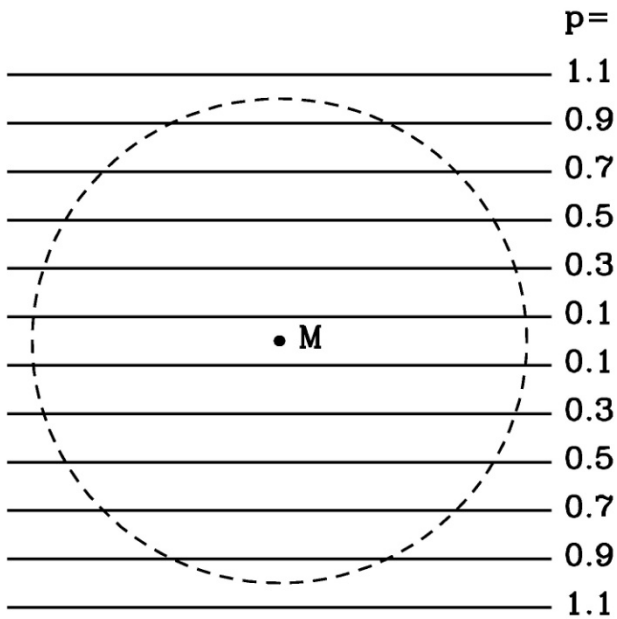
p=
1.1
0.9
0.7
0.5
0.3
0.1
M
0.1
0.3
0.5
0.7
0.9
1.1

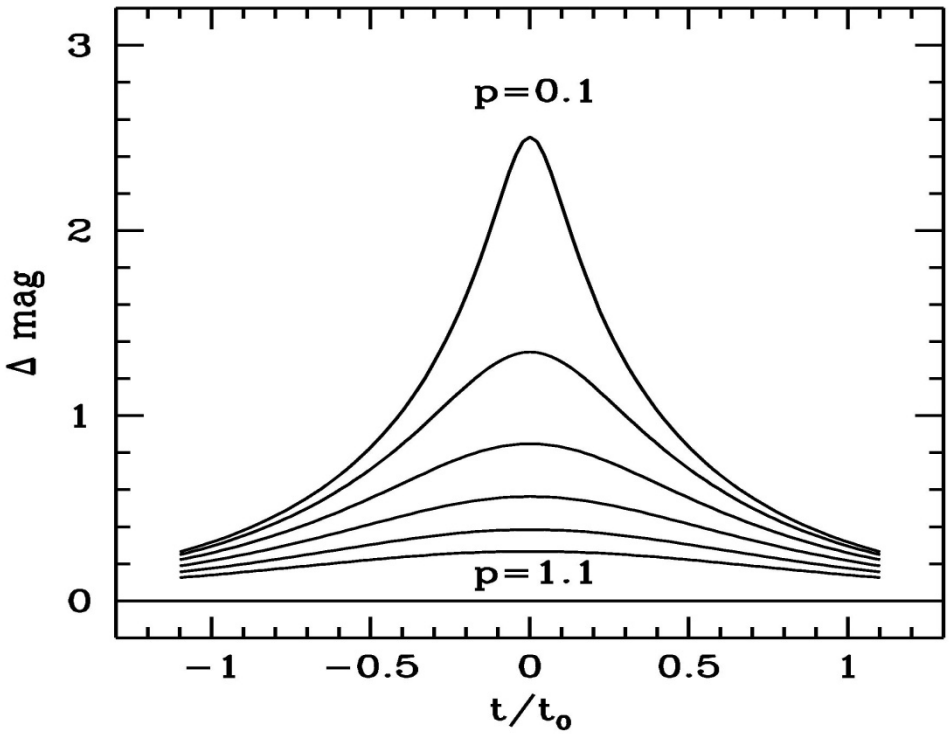
3
2
1
0
Δ mag
p=0.1
p=1.1
−1
−0.5
0
0.5
1
t/t$_o$

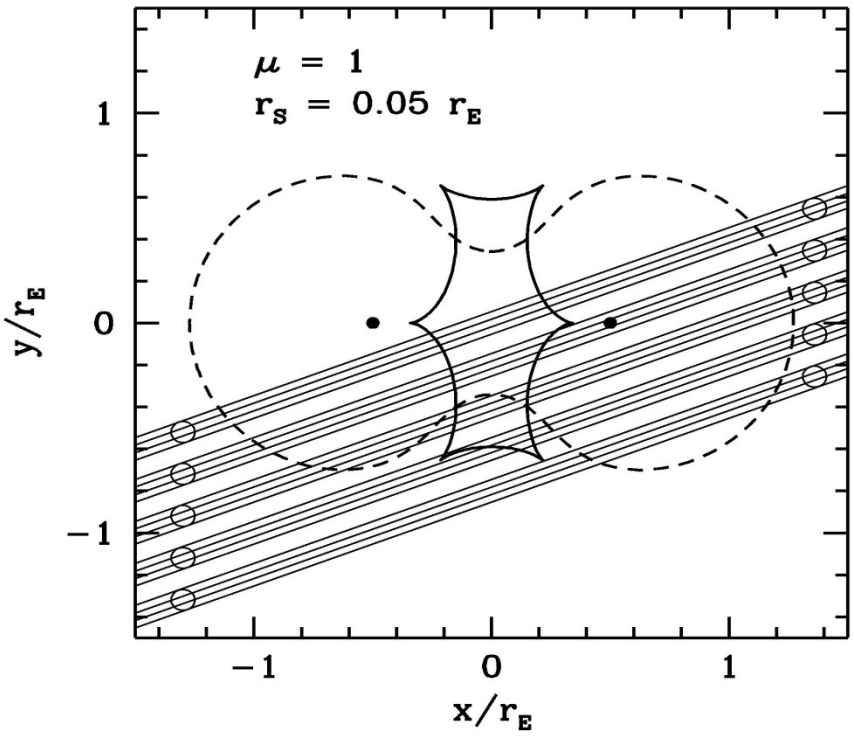
μ = 1
r_S = 0.05 r_E
1
0
−1
y/r_E
−1
0
1
x/r_E

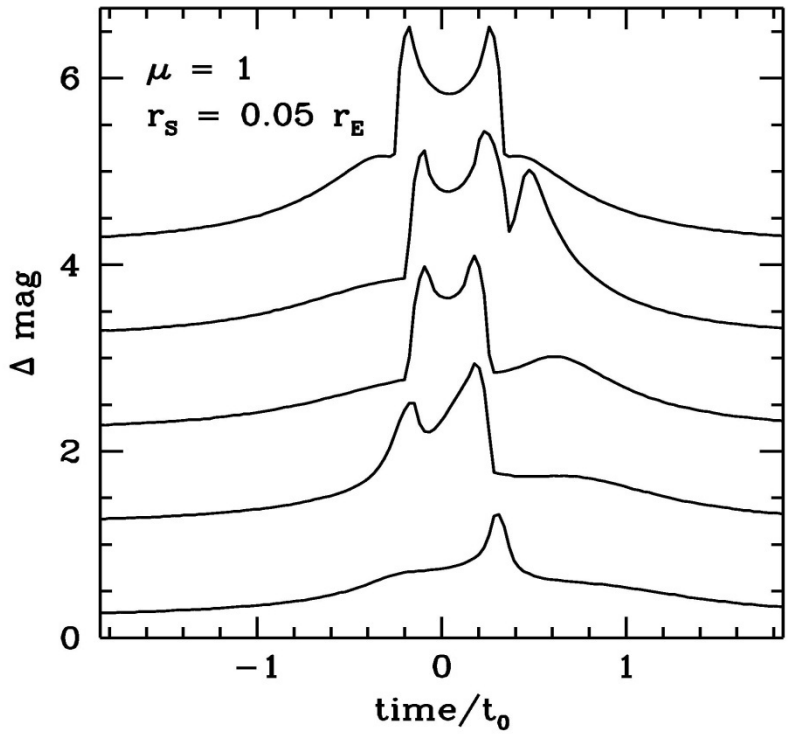
μ = 1
r_S = 0.05 r_E
Δ mag
time/t_0
0
2
4
6
−1
0
1

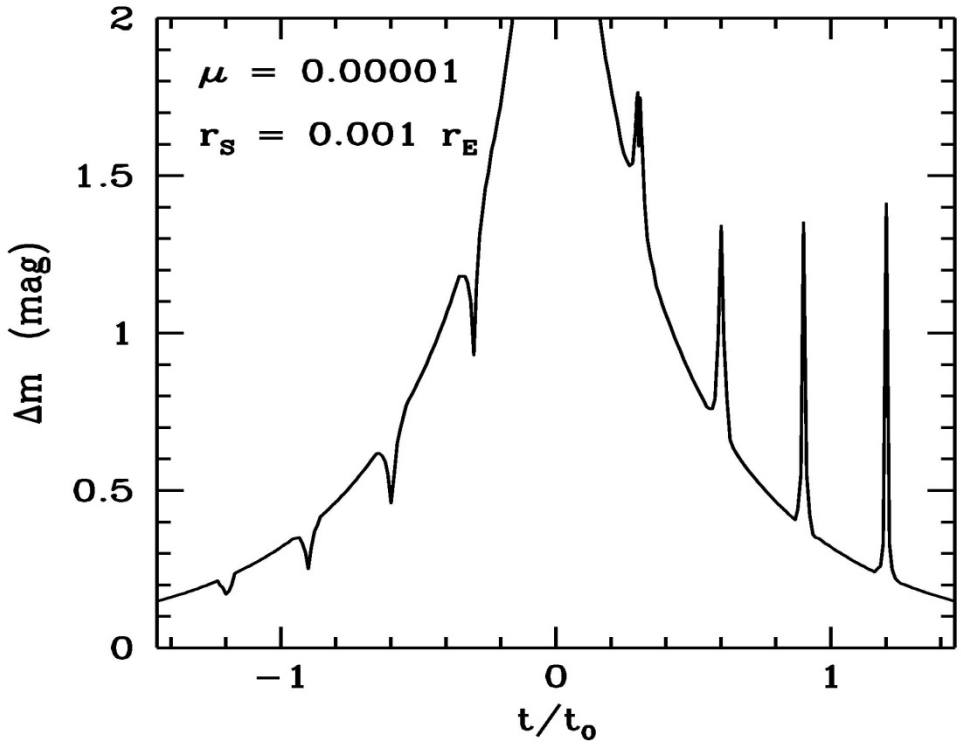
μ = 0.00001
r_S = 0.001 r_E
Δm (mag)
t/t_o
2
1.5
1
0.5
0
−1
0
1

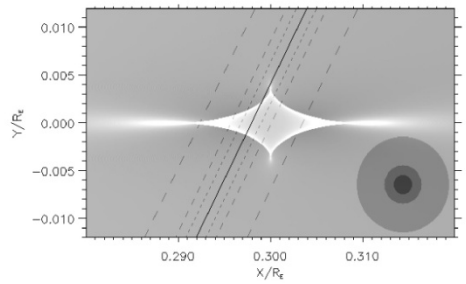
0.010
0.005
0.000
−0.005
−0.010
Y/R_E
0.290
0.300
0.310
X/R_E

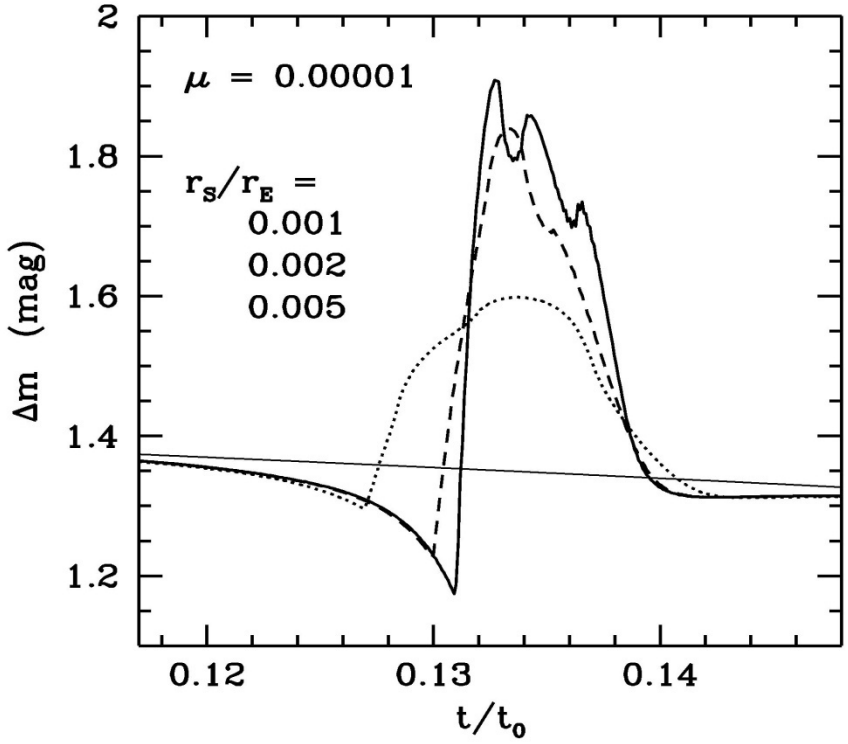
μ = 0.00001
r_S/r_E =
0.001
0.002
0.005
Δm (mag)
t/t_0
2
1.8
1.6
1.4
1.2
0.12
0.13
0.14

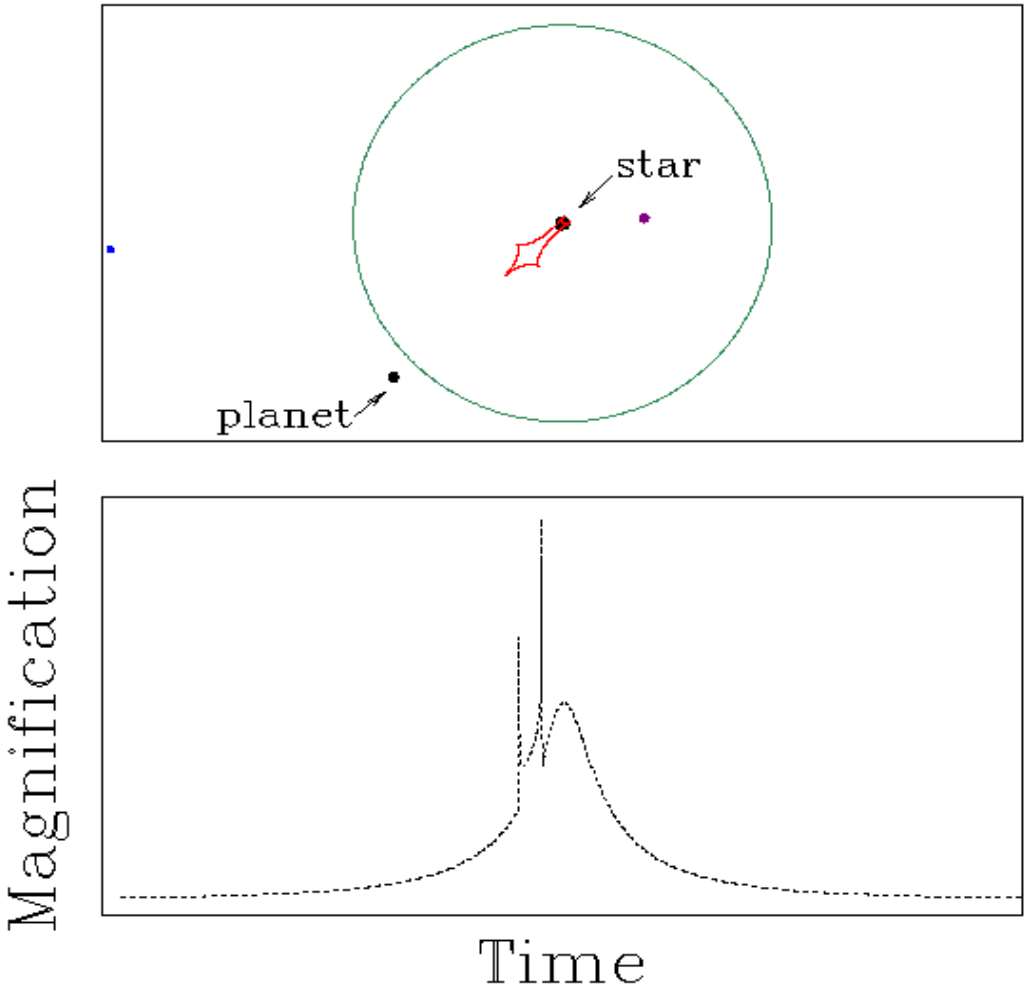
star
planet
Magnification
Time

DM matter problem

$$\Omega = \rho/\rho_c, \rho_c = \frac{3H_0^2}{8\pi G} = 2 \times 10^{-29} \text{g/cm}^2, \quad (17)$$

where

$$h = \frac{H_0}{100 \text{ km s}^{-1}\text{Mpc}^{-1}}, \quad (18)$$

Flat rotation curves for galaxies $M(R) \sim R$ (for $r > r_c$) (Rubin, 1980)

Our Galaxy has a halo with radius $R > 30$ kpc (Fich, Tremaine, 1991)

Galactic clusters and rich clusters $\rho_{DM} > \rho_{\text{vis}} \times 10$ (Zwicky, 1933, White et al. 1993)

Persic & Salucci (1992) claimed $0.003 < \Omega_{vis} < 0.007$

According the cosmological SN (Supernovae) Ia data and CMB anisotropy one could take that $\Omega_\Lambda \approx 0.7, \Omega_0 \approx 0.3$. Recent CMB anisotropy observations by the WMAP satellite team has confirmed

important aspects of the current standard cosmological model, actually, the WMAP team determined $\Omega_\Lambda \approx 0.73, \Omega_0 \approx 0.27$ (Spergel, 2003) for the "best" fit of cosmological parameters. Big Bang Nucleosynthesis (BBN) calculations together with observational data about an abundance of ^{2}D give the following constraints on cosmic baryon density (Turner, 2002)

$$\Omega_b h^2 = 0.02 \pm 0.002, \tag{19}$$

and taking into account the Hubble constant estimation $h = 0.72 \pm 0.08$ (Freedman, 2001). Therefore, using for example the estimate one could obtain cosmic baryon density

$$\Omega_b = 0.039 \pm 0.0075. \tag{20}$$

Using cosmic microwave background (CMB) anisotropy data of BOOMERANG and MAXIMA-1 experiments (Stompor et al. 2001) obtained that

$$\Omega_b h^2 = 0.033 \pm 0.013. \tag{21}$$

An analysis of recent WMAP data on CMB anisotropy gives as the best fit (Spergel, 2003)

$$\Omega_b h^2 = 0.0224 \pm 0.0009, \tag{22}$$

which is very close to the BBN constraints, but with much smaller error bars.

Non-baryonic DM

1. Primordial Black Holes (PBHs)

2. Axions.

3. Neutralinos.

4. Neutrinos.

Baryonic DM

1. Snow balls 10^{22}g $< m < 10^{26}$g
2. Brown dwarfs $m < m_{HB} \sim 0.08 M_{\odot}$
3. Faint M-dwarfs
4. Clouds of molecular hydrogen.
5. Neutron stars.
6. Black holes as a result of stellar collapse.

Galactic components

Galactic halo (spheroid)

$$\rho^H = \rho_0^H \frac{R_0^2 + a^2}{r^2 + a^2},$$

where
$\rho_0^H = 10^{-2} M_\odot \text{pc}^{-3}$, $R_0 = 8.5$ kpc, $a \in [2, 8]$ kpc

Galactic disk

$$\rho^D = \rho_0^D \exp\left(-\frac{R-R_0}{h_R} - \frac{|z|}{h_z}\right),$$

where ρ_0^D is a local disk density, $h_R = 3.5$ kpc, ($h_R \in [2,8]$ kpc), $h_z \in [100, 350]$ pc, surface density (Gould et al. 1996)

$$\Sigma_0^D := 2h_z\rho_0^D \sim 40 M_\odot/\mathrm{pc}^2,$$

and the total mass

$$M_D \sim 4.4 \times 10^{10} M_\odot \left(\frac{\Sigma_0^D}{50\ M_\odot\ \mathrm{pc}^{-2}}\right),$$

Galactic bulge

The inner part of Galaxy with radius 1 –2 kpc is called galactic bulge (Dwek, 1995)

$$\rho^B(s) = \frac{M_0}{8\pi abc} \exp\left(-\frac{-s^2}{2}\right),$$

where

$$^4 := \left[\left(\frac{x'}{a}\right)^2 + \left(\frac{y'}{b}\right)^2\right]^2 + \left(\frac{z'}{c}\right)^4,$$

x', y', z' are the main axis of the bar

$$x' = x\cos\alpha + y\sin\alpha,$$

$$y' = -x\sin\alpha + y\cos\alpha,$$

$$z' = z$$

$a = 1.58$ kpc, $b = 0.62$ kpc, $c = 0.43$ kpc, $\alpha \sim 20^0$.

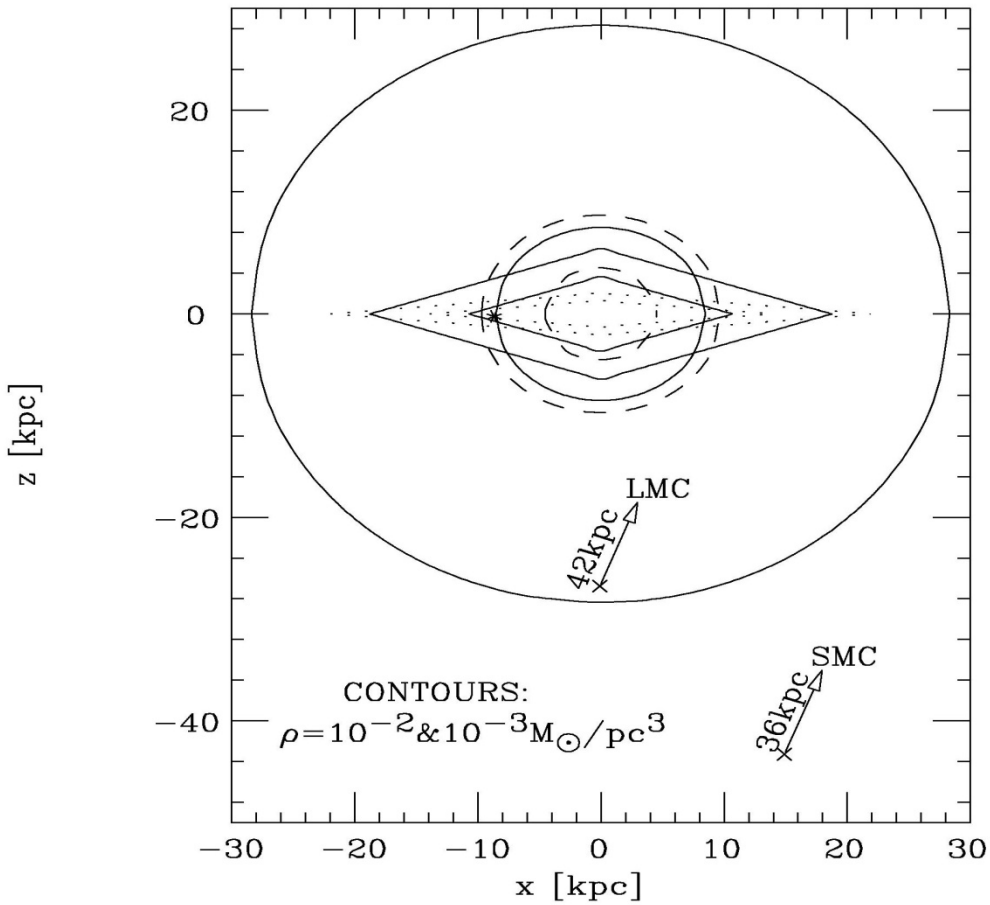
20
0
−20
−40
z [kpc]
−30
−20
−10
0
10
20
30
x [kpc]
LMC
42kpc
SMC
36kpc
CONTOURS:
$\rho=10^{-2}\&10^{-3}M_\odot/pc^3$

Results:
"Machos and clouds of uncertainties"

MACHO collaboration (astro-ph/0001272)

Target: LMC; Time of observations: 5.7 years

Number of stars (10^6): 11.9

Number of candidates: $13 - 17$

Durations of events (days): $34 - 230$

Contribution of Machos in halo density: f =0.2

Masses of Machos: $m \in [0.15 - 0.9] M_\odot$ (it depends on halo model)

The total mass of Machos in halo up to 50 kpc: $9^{+4}_{-3} \times 10^{10} M_\odot$

Optical depth: $1.2^{+0.4}_{-0.3} \times 10^{-7}$

Probabilities: $P(0.08 < f < 0.5) = 0.95$,
$P(f = 1) < 0.05$

MACHO results of gravitational microlensing toward LMC and SMC (analysis of observations of two years)

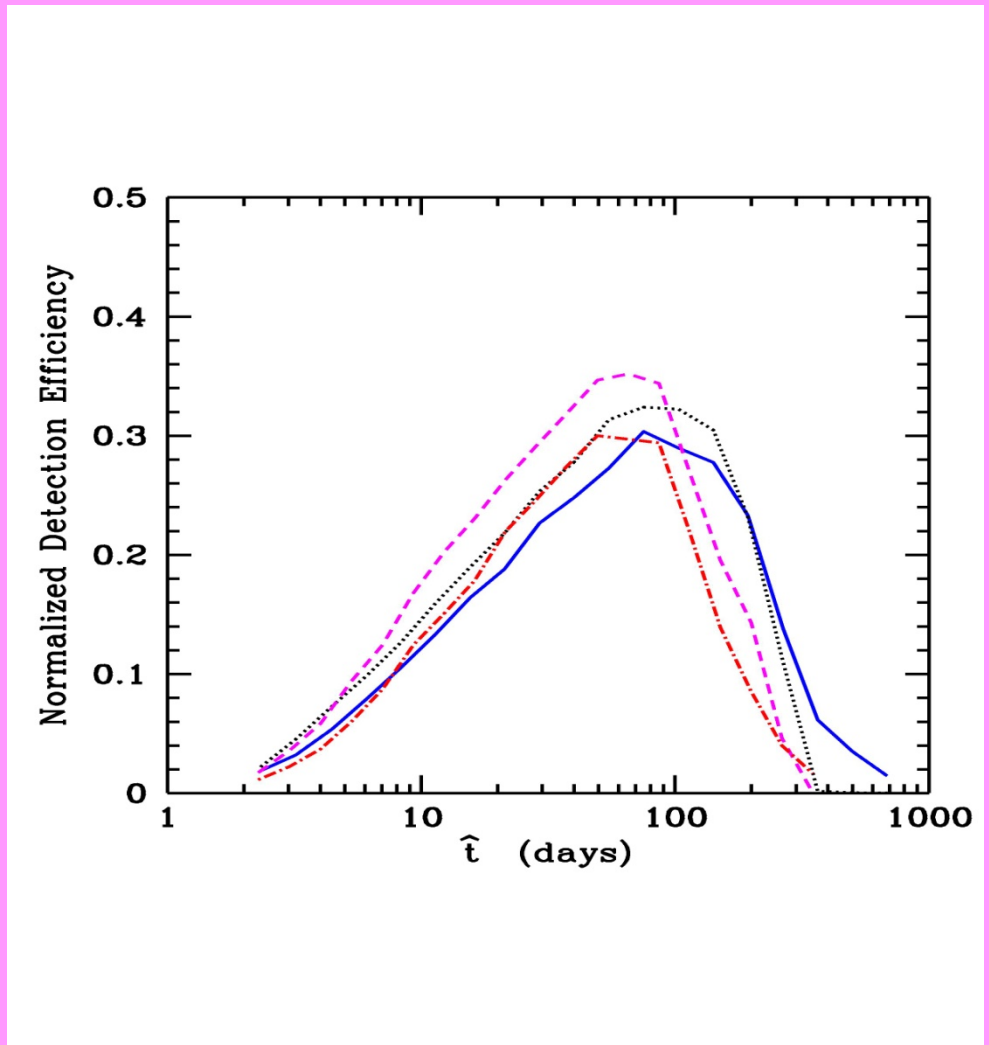

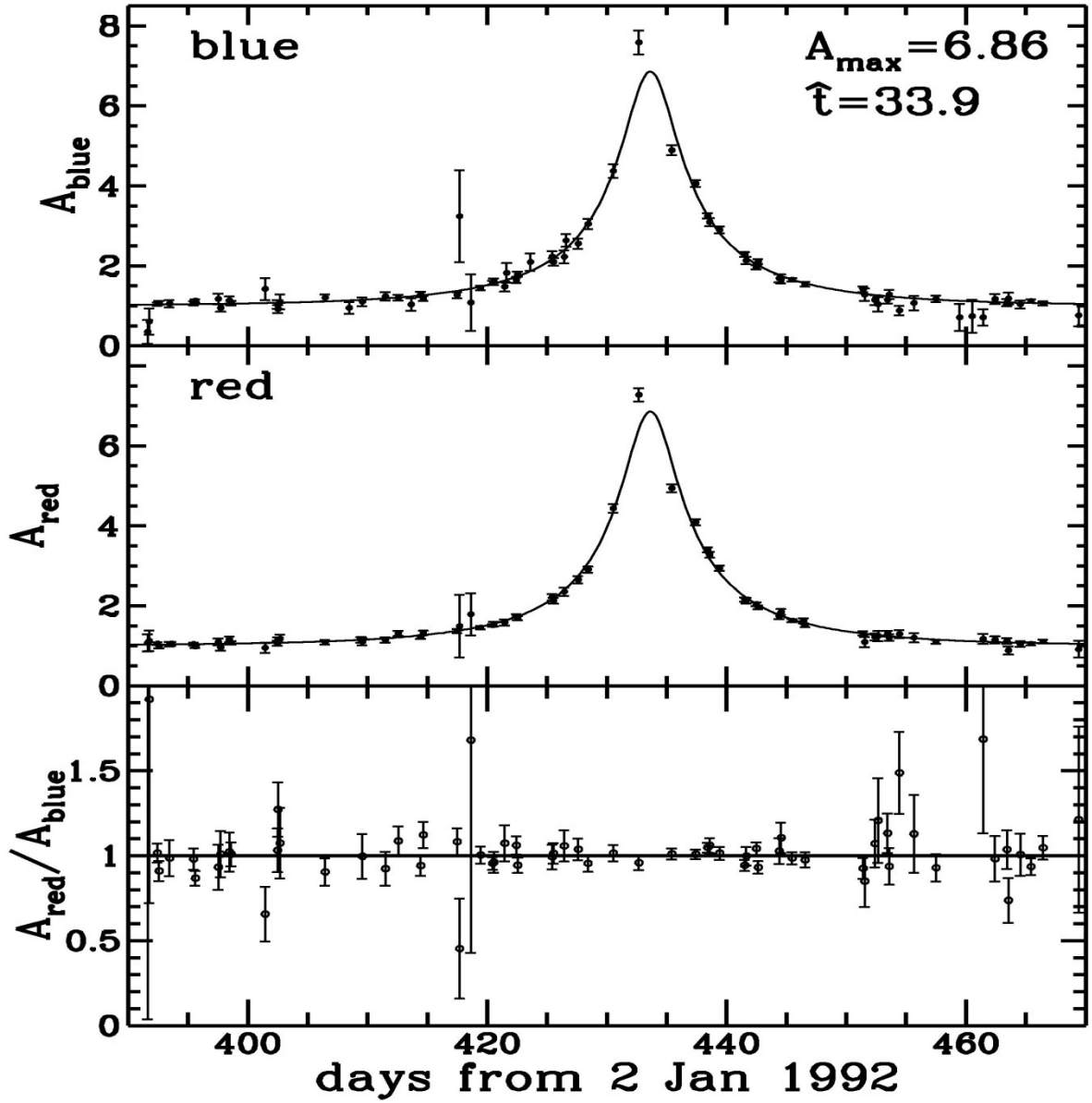
blue
A_{max}=6.86
$\hat{t}$=33.9
A_{blue}
red
A_{red}
A_{red}/A_{blue}
days from 2 Jan 1992

EROS collaboration (astro-ph/0011375)

Target: LMC & SMC

Time of observations: 3 years

Number of stars (10^6): 25

Number of candidates: 6 (1 (EROS-I); 4 (LMC), 1 (SMC) + 1 binary microlens in SMC). If the halo is formed by Machos with $M \sim M_\odot$, EROS could detect $\sim$ 30 events.

Durations of events (days): $24 - 44$

Probabilities:
$P(m \in [10^{-1}, 10] M_\odot \& f > 0.4) < 0.05$

Expérience de Recherche d'Objets Sombres

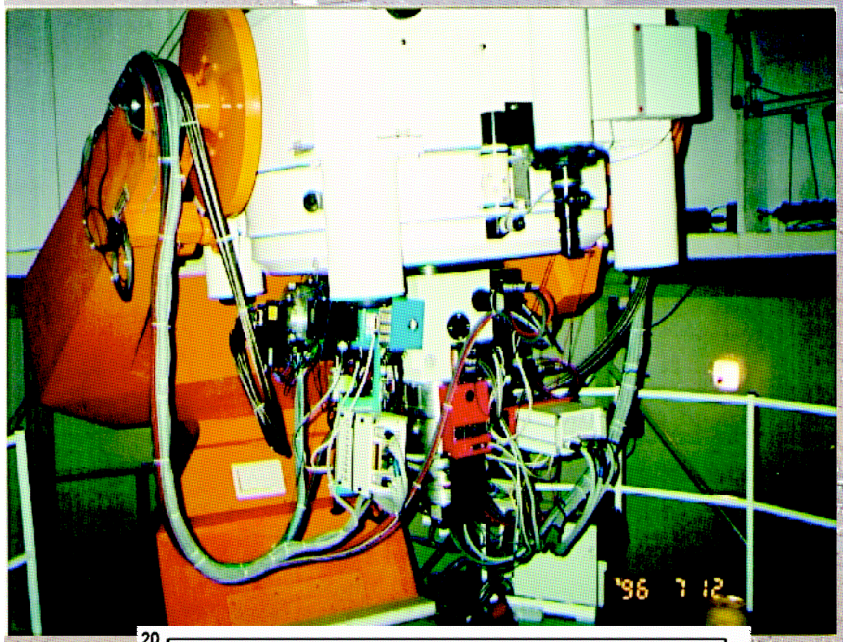

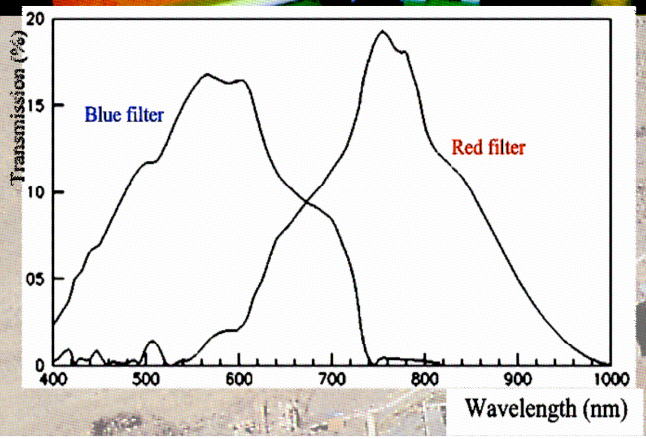

- 1m telescope in Chile
- Wide-field cameras **R** et **B** -> 32Mpix each
- 7 years operation
- ***50 Terabytes of data***
- 850,000 images processed
- ~77 10^6 stars measured 300 to 500 times
- **EROS1 (1990-1994)**
- **EROS2 (1996-2003)**
- Main subject: microlensing
- A number of other topics:
  - SN searches
  - Proper motion searches
  - Variable stars

Events found after 7 years of data taking

- ✓**Galactic Center: hundreds of microlensing events found**
  - •20 million stars monitored
  - •5.6 million **Red Giant** stars
  - •**120 microlensing** events on **RG**
- ✓**Spiral arms**
  - •13.3 million stars monitored
  - •**26 microlensing** events
- ✓**LMC**
  - •29.2 million stars monitored
  - •5.5 million « bright » stars
  - •**1 microlensing** event on bright stars
- ✓**SMC**
  - •4.2 million stars monitored
  - •0.84 million « bright » stars
  - •**1 microlensing** event on bright stars

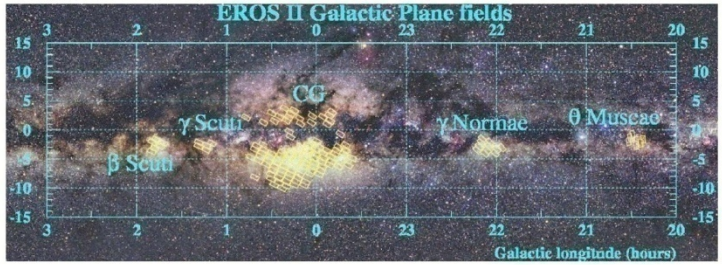

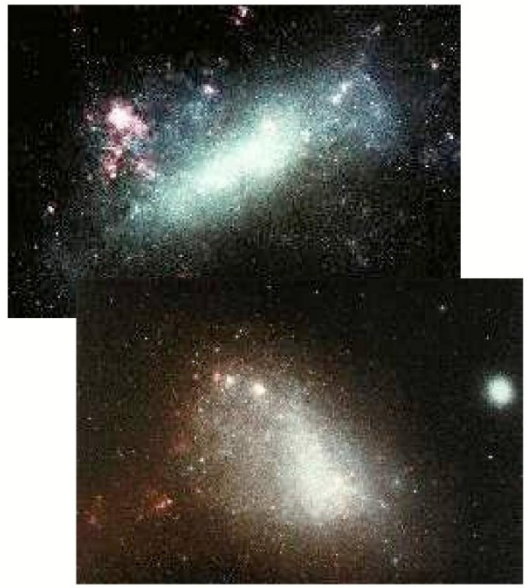

Examples of candidates (3)

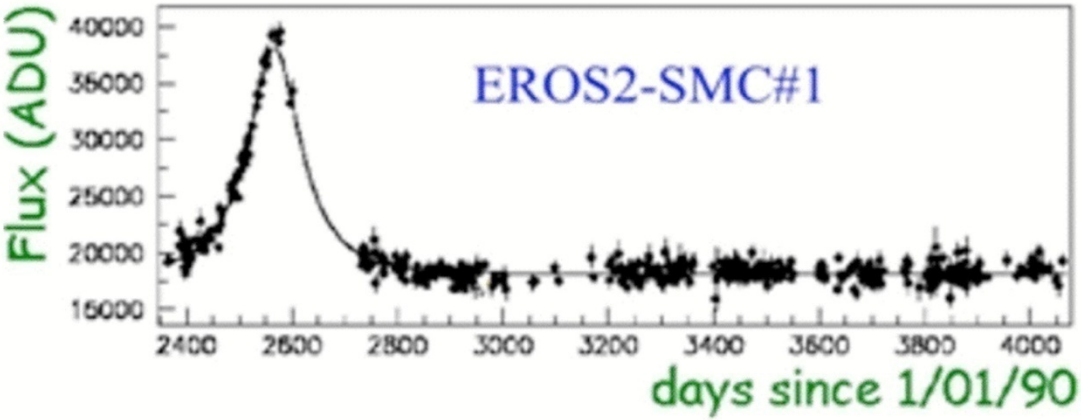

- **The SMC candidate. t_E = 125 days.**

The longest found towards the magellanic clouds

- **Probably due to self-lensing:**

A lens in the halo would produce detectable distortions due to Earth annual motion (parallax)

Upper limit on the contribution of compact objects to the galactic halo

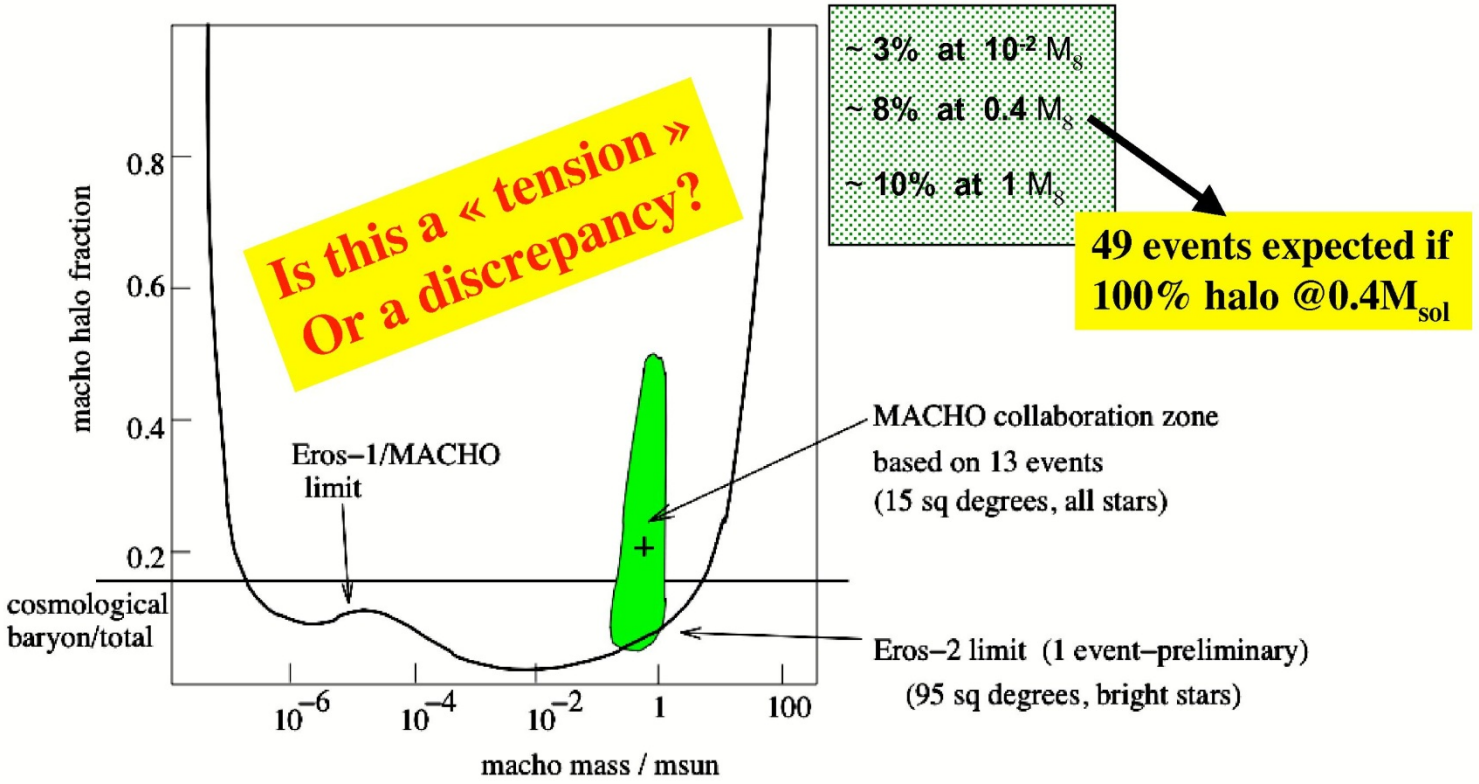

The 13 (+4) MACHO events in EROS data

- 13 occured before EROS data taking
- MACHO LMC-23 showed a second variation 7 years later in the EROS data
- MACHO LMC-14 and 20, seen in EROS but not in bright sample
- MACHO LMC-15, source fainter than EROS detection limit

Deceased candidates

- **EROS 1 – LMC#1** : **(Be star)**

~ 1992

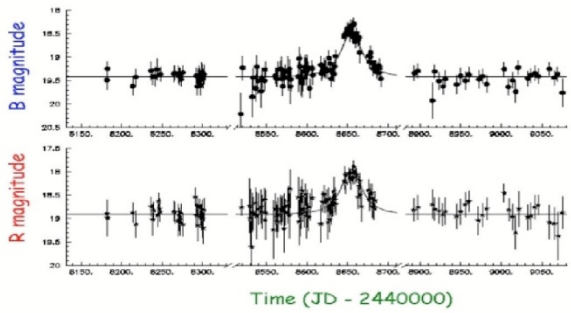

~ 1997

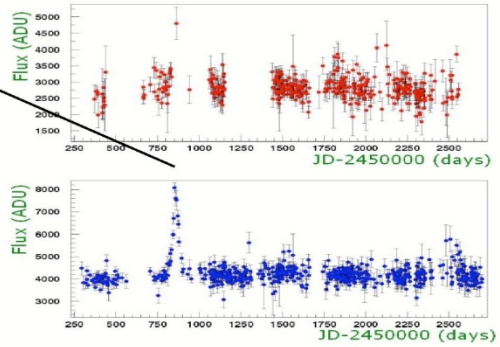

- **MACHO – LMC#23** :

~ 1995

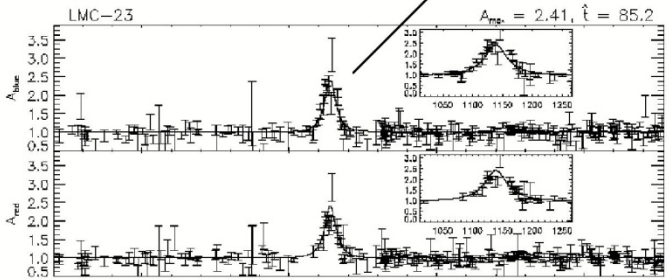

~ 2001

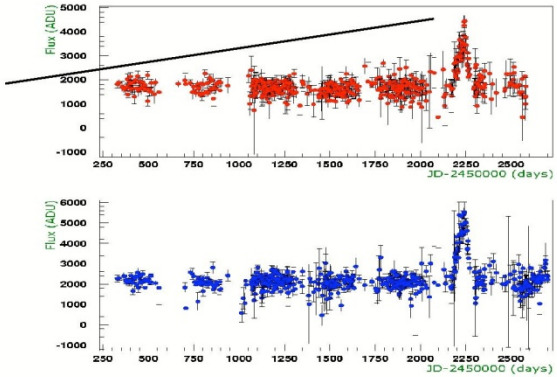

Possible origins of discrepancies

- **ESSENTIAL**: **Different monitored populations**
  - EROS = wide field, bright stars
  - MACHO = narrow field (mainly the bar), dim stars
  - ✓ could result in a stronger self-lensing contribution in MACHO sample
  - ✓ Variable star contamination: the « not so well understood background »
  - ✓ Blending underestimated (MACHO)
- Efficiency estimates

MACHO collaboration (astro-ph/0002510)

Target: Galactic bulge

Time of observations: 3 years

Number of stars (10^6): 17

Number of candidates: 99

Durations of events (days): 2.3 – 300

Square of sky: $S \sim 4$ degree^2

Optical depth: $2.91^{+0.47}_{-0.45} \times 10^{-6}$ (averaged on 8 fields near $l = 2.68^0, b = -3.35^0$.

EROS (II) collaboration (astro-ph/0001083)

Target: Spiral arms

Time of observations: 3 years

Number of stars (10^6): 9.1

Number of candidates: 7

Durations of events (days): $6.2 - 98$

Optical depth: $0.45^{+0.24}_{-0.11} \times 10^{-6}$.

OGLE (II) collaboration (astro-ph/0002418)

Target: Galactic bulge

Time of observations: 3 years

Number of stars (10^6): 20.5

Number of candidates: 214 (about 20 binary MLs)

Durations of events (days): 6.2 – 98

Since the end of 2000 OGLE started to monitor LMC

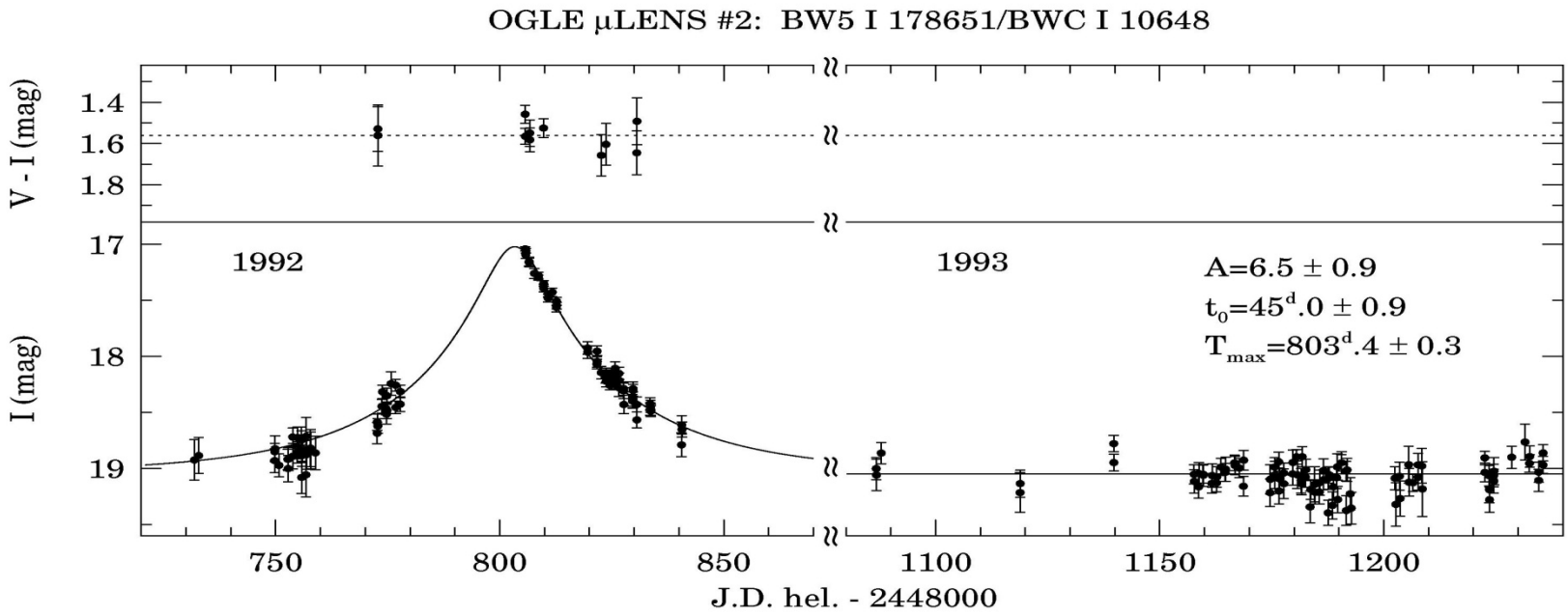
OGLE μLENS #2: BW5 I 178651/BWC I 10648
V - I (mag)
I (mag)
1.4
1.6
1.8
17
18
19
1992
1993
A=6.5 ± 0.9
t0=45d.0 ± 0.9
Tmax=803d.4 ± 0.3
750
800
850
1100
1150
1200
J.D. hel. - 2448000

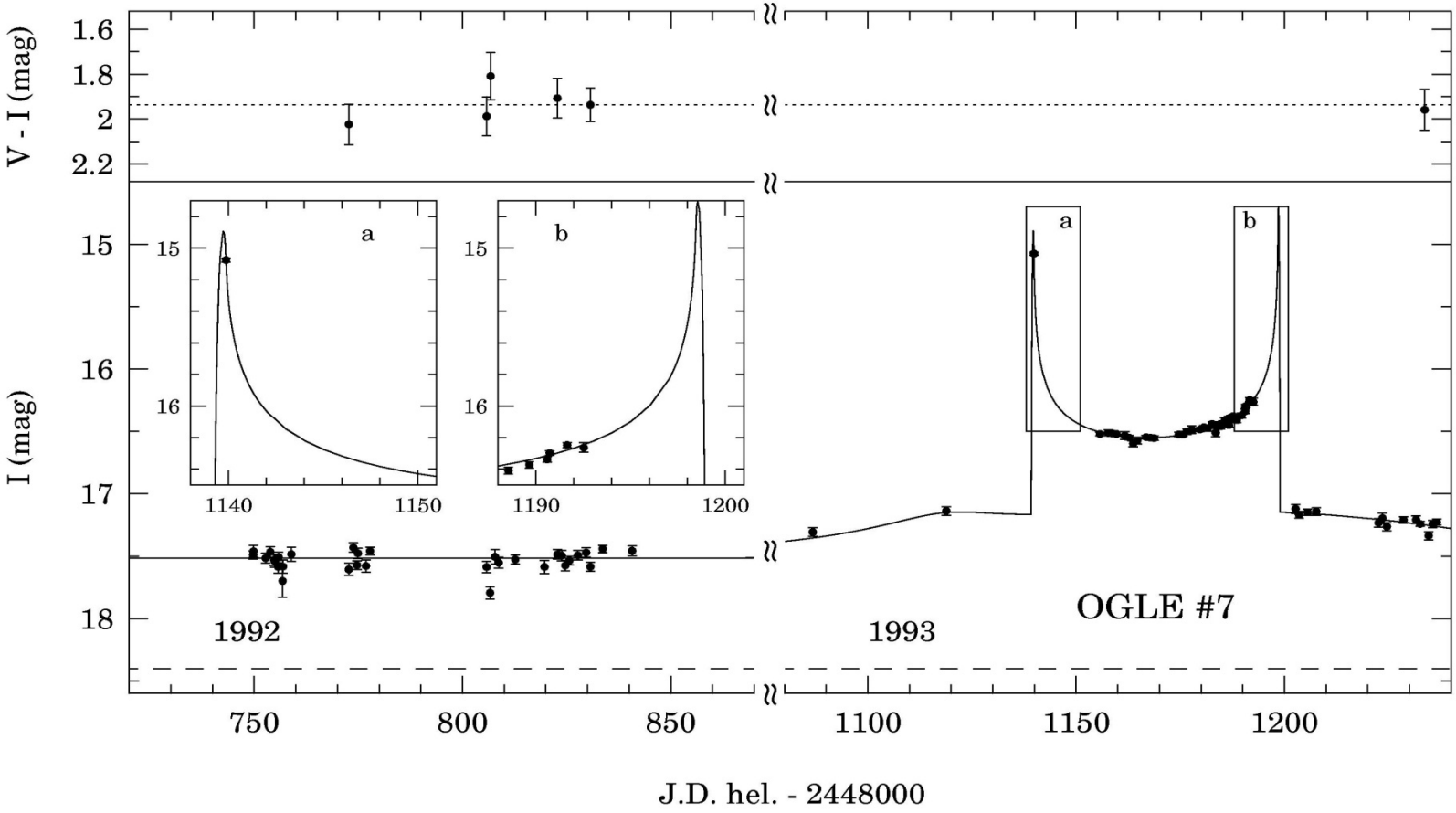
V - I (mag)
I (mag)
1.6
1.8
2
2.2
15
16
17
18
a
b
15
16
1140
1150
1190
1200
1992
1993
OGLE #7
750
800
850
1100
1150
1200
J.D. hel. - 2448000

Discoveries of BHs with stellar masses

MACHO, GMAN, MPS reported about discoveries of BHs with stellar masses (Bennett el al., ApJ, **579**, 639 (2002)) MACHO-96-BLG-5 $M/M_{\odot} = 6^{+10}_{-3}$ and MACHO-96-BLG-6 $M/M_{\odot} = 6^{+7}_{-3}$

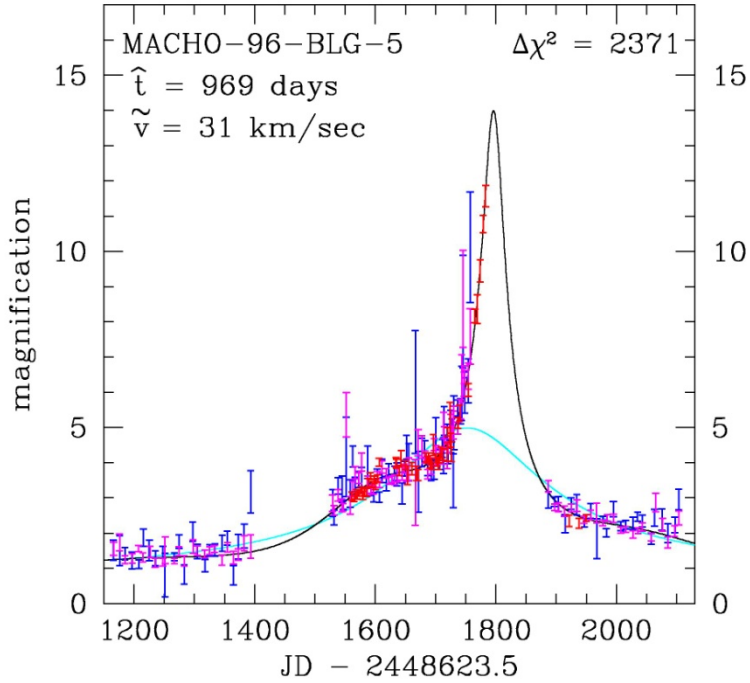

Fig. 7.— MACHO-96-BLG-5 lightcurves normalized to the unlensed flux of the lensed star. The MACHO red and blue data are plotted in magenta and blue, respectively, and the CTIO data are shown in red. The black curve is the parallax fit while the cyan curve is the best fit standard microlensing lightcurve. An additional 4 years of data showing very little photometric variation are not shown.

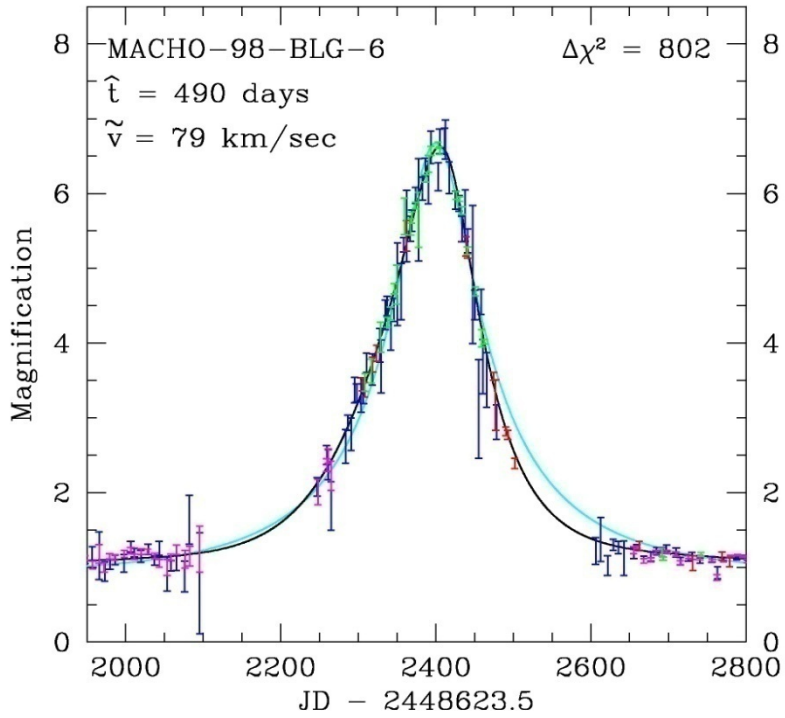

Fig. 4.— MACHO-98-BLG-6 lightcurve closeup with lightcurves normalized to the unlensed flux of the lensed star. The MACHO red and blue data are plotted in magenta and blue, respectively, the CTIO data are shown in red, and the MPS data are shown in green. The black curve is the parallax fit while the cyan curve is the best fit standard microlensing lightcurve. The gap in the MACHO red data during the day 2280-2650 interval is due to a CCD failure. An additional year of data showing no photometric variation is not shown.

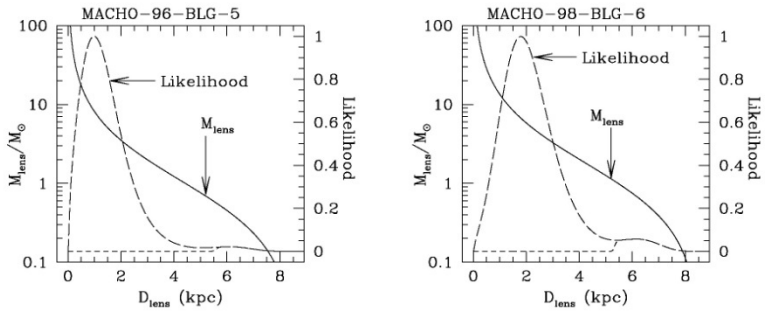

Fig. 11.— The mass vs. distance relations (solid curves) for our candidate black hole lenses are shown along with the likelihood functions (long dashed curves) computed assuming a standard model for the Galactic phase space distribution. The source star is assumed to reside in the bulge for both events. The implied best fit masses are $M = 6^{+10}_{-3}\mathrm{M}_\odot$ for the MACHO-96-BLG-5 lens and $M = 6^{+7}_{-3}\mathrm{M}_\odot$ for the MACHO-98-BLG-6. The 95% confidence level lower limits on the masses are $1.6\mathrm{M}_\odot$ and $0.94\mathrm{M}_\odot$ respectively. The short dashed curves delineate the portion of the likelihood functions that is allowed when the lens is assumed to be a main sequence star. The ratio of the area below this portion to the entire area below the likelihood curve gives a probability that a lens is a main sequence star. For MACHO-96-BLG-5, the upper limit on the lens brightness is very stringent because of the HST images, and a main sequence lens is ruled out.

Table 7. Mass & Magnitude Estimates for the MACHO Microlensing Parallax Events

Event	$M/\mathrm{M}_\odot$	$M_{\mathrm{MS}}/\mathrm{M}_\odot$	$D_{\ell-\mathrm{MS}}$	sep-MS	V_s	$\Delta I_{\ell s}$	$\Delta V_{\ell s}$	$\Delta B_{\ell s}$	$\Delta U_{\ell s}$
104-C	$1.1^{+1.1}_{-0.5}$	0.74	2.7 kpc	40 mas	17.3	3.5	3.5	3.5	3.2
96-BLG-5	6^{+10}_{-3}	-	-	-	-	-	-	-	-
96-BLG-12	$1.3^{+1.8}_{-0.7}$	0.75	2.0 kpc	28 mas	18.0	2.1	2.2	2.2	2.3
98-BLG-6	$2.5^{+1.7}_{-0.9}$	0.88	5.7 kpc	5 mas	20.1	2.2	1.9	1.6	1.1
99-BLG-1	$0.7^{+1.2}_{-0.4}$	0.40	1.7 kpc	17 mas	18.9	1.8	3.2	3.6	3.9
99-BLG-8	$1.2^{+1.6}_{-0.6}$	1.2	1.6 kpc	25 mas	16.3	1.3	0.7	−0.3	−1.1

Note. — These are the parameters of the "most likely" main sequence star lenses for our best microlensing parallax events. For MACHO-96-BLG-5, a main sequence lens is ruled out.

The ML mass determination

Using photometric observations of the caustic-crossing binary lens microlensing event EROS BLG-2000-5, PLANET collaboration reported about the first microlens mass determination, namely the masses of these components are 0.35 $M_\odot$ and 0.262 $M_\odot$ and the lens lies within 2.6 kpc of the Sun (An et al., ApJ, 72, 521 (2002)).

When new observational data would be collected and the processing methods would be perfected, probably some microlensing event candidates lost their status, but perhaps new microlensing event candidates would be extracted among analysed observational data. So, the general conclusion may be done. The very important astronomical phenomenon was discovered, but some quantitative parameters of microlensing will be specified in future. However, the problem about 80% of DM in the halo of our Galaxy is still open (10 years ago people believe that microlensing could give an answer for this problem).

Future space projects

a) Galactic Exoplanet Survey Telescope (GEST): during 3 seasons (2.5 years) ~ 1.5 m telescope will monitor about $\sim 2 \times 10^8$ stars in 6 degree^2 toward Galactic bulge will find ~ 5000 planet like Jupiter, ~ 1300 planet like Neptune, ~ 100 planet like the Earth.

b) GAIA, SIM & astrometrical microlensing is very important issue

Planet discovery with ML with the lowest mass

(J.-P. Beaulieu et al. Nature, 2006)

Planet discovery with ML with the lowest mass in 2006 (now people find a planet with a mass about 2 Earth masses, see Mayor et al.)

(J.-P. Beaulieu et al. Nature, 2006)

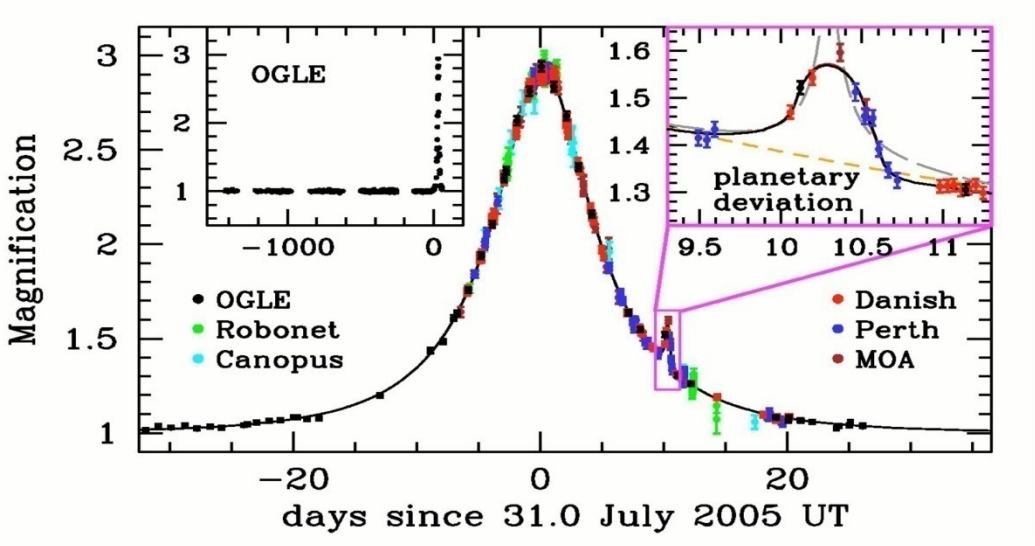

Figure 1 : The observed light curve of the OGLE-2005-BLG-390 microlensing event and best fit model plotted as a function of time. The data set consists of 650 data points from PLANET Danish (ESO La Silla, red points), PLANET Perth (blue), PLANET Canopus (Hobart, cyan), RoboNet Faulkes North (Hawaii, green), OGLE (Las Campanas, black), MOA (Mt John Observatory, brown). This photometric monitoring was done in the I band (with the exception of Faulkes R band data and MOA custom red passband) and real-time data reduction was performed with the different OGLE, PLANET and MOA data reduction pipelines. Danish and Perth data were finally reduced by the image subtraction technique[19] with the OGLE pipeline. The top left inset shows the OGLE light curve extending over the previous 4 years, whereas the top right one shows a zoom of the planetary deviation, covering a time interval of 1.5 days. The solid curve is the best binary lens model described in the text with a planet-to-star mass ratio of $q = 7.6 \pm 0.7 \times 10^{-5}$, and a projected separation $d = 1.610 \pm 0.008\ R_E$ (where R_E is the Einstein ring radius). The dashed grey curve is the best binary source model that is rejected by the data, while the dashed orange line is the best single lens model.

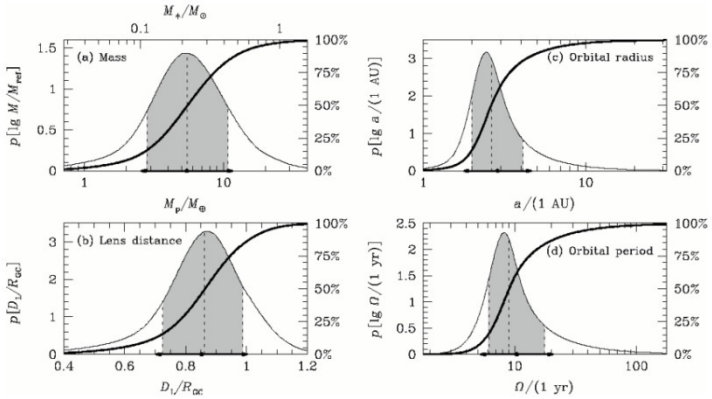

Figure 2 : Bayesian probability densities for the properties of the planet and its host star. The individual panels show the masses of the lens star and its planet (a), their distance from the observer (b), the three-dimensional separation or semi-major axis of an assumed circular planetary orbit (c) and the orbital period of the planet (d). The bold, curved line in each panel is the cumulative distribution, with the percentiles listed on the right. The dashed vertical lines indicate the medians, and the shading indicates the central 68.3% confidence intervals, while dots and arrows on the abscissa mark the expectation value and standard deviation. All estimates follow from a Bayesian analysis assuming a standard model for the disk and bulge population of the Milky Way and the stellar mass function of ref. [23], and a prior for the source distance D_S=1.05 ±0.25 R_{GC} (where R_{GC}= 7.62 ± 0.32 kpc for the Galactic Centre distance). The medians of these distributions yield a $5.5^{+5.5}_{-2.7}$ Earth mass planetary companion at a separation of $2.6^{+1.5}_{-0.6}$ AU from a $0.22^{+0.21}_{-0.11} M_\odot$ Galactic Bulge M-dwarf at a distance of 6.6 ± 1.0 kpc from the Sun. The median planetary period is 9^{+9}_{-3} years. The logarithmic means of these probability distributions (which obey Kepler's third law) are a separation of 2.9 AU, a period of 10.4 years, and masses of $0.22 M_\odot$ and $5.5 M_\oplus$ for the star and planet, respectively. In each plot, the independent variable for the probability density is listed within square brackets. The distribution of planet-star mass ratio was taken to be independent of the stellar mass, and a uniform prior was assumed for the planet-star separation distribution.

The POINT-AGAPE collaboration

(Pixels Observation at INT) (Andromeda Galaxy Amplified Pixel Experiment)

ARI – Liverpool, IoA – Cambridge, ITP – Zurich, OMP – Toulouse, Oxford University
PCC-Collège de France – Paris, QWM – London, Université Bretagne-sud – Vannes

Photometric survey of M31:

- Isaac Newton Telescope (INT) ∅=2,5m (La Palma, Canaries)
- Wide Field Camera (WFC)
- 180 observation nights (1 h/night between aug. 1999 and jan. 2002)
- 3 filters : Sloan i', r' et g'
- field : 0,55 deg²

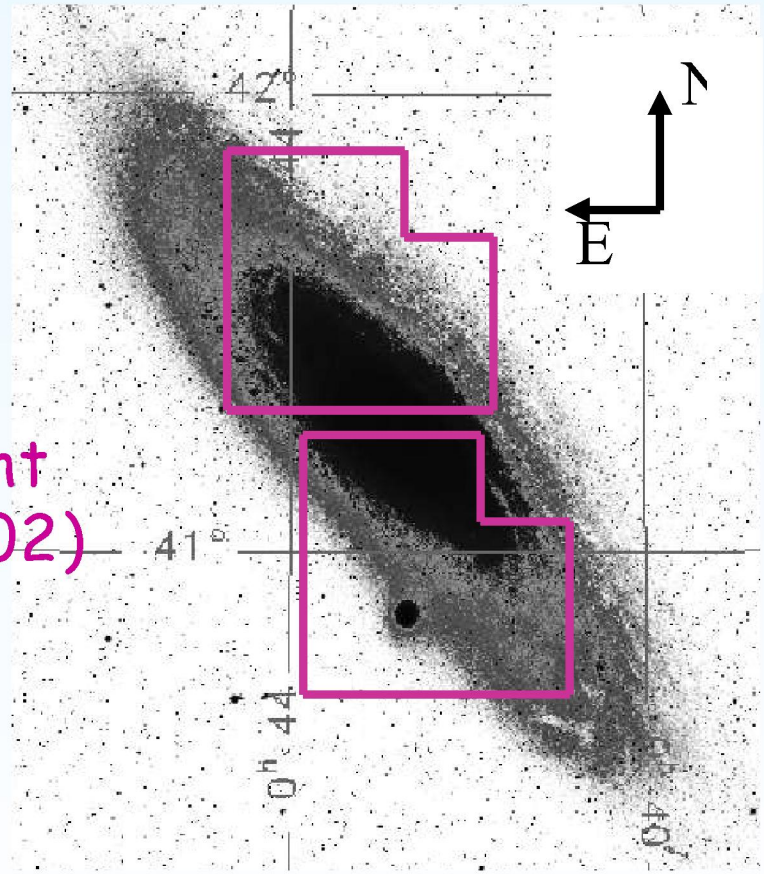

D.P. Bennett et al. A Low-Mass Planet with a Possible Sub-Stellar-Mass Host in Microlensing Event MOA-2007-BLG-192
Arxive:0806.0025[astro-ph] .

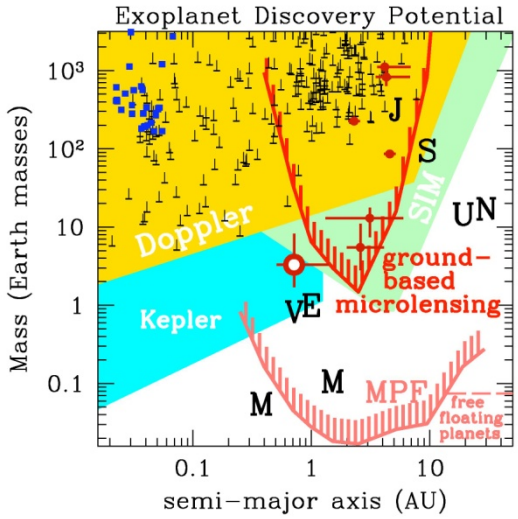

Fig. 16.— The known extrasolar planets are plotted as a function of mass vs. semi-major axis, along with the predicted sensitivity curves for a number of methods. The microlensing planets are indicated by dark red spots with error bars, and the large red spot with a white dot in the center is MOA-2007-BLG-192Lb. The blue dots indicate the planets first detected via transits, and the black bars with upward pointing error bars are the radial velocity planet detections. (The upward error bars indicate the 1-σ $\sin i$ uncertainty.) The gold, cyan, and light green shaded regions indicated the expected sensitivity of the radial velocity programs and the Kepler and SIM space missions. The dark and light red curves indicate the predicted lower sensitivity limits for a ground based and space-based (Bennett & Rhie 2002) microlensing planet search program, respectively. The Solar System's planets are indicated with black letters.

Table 2. Parameter Values and MCMC Uncertainties - without prior

parameter	value	2-σ range
M	$0.039^{+0.022}_{-0.012} M_\odot$	0.019–0.113$M_\odot$
m	$2.3^{+2.5}_{-0.8} M_\oplus$	0.9–14.4$M_\oplus$
$a_\perp$	$0.58^{+0.18}_{-0.14}$ AU	0.32–1.04 AU
D_L	1.3 ± 0.5 kpc	0.5–2.3 kpc
I_S	21.44 ± 0.08	21.30–21.60
q	$1.9 \pm 0.8 \times 10^{-4}$	0.6–6.4 $\times 10^{-4}$

Table 3. Parameter Values and MCMC Uncertainties - with prior

parameter	value	2-σ range
M	$0.060^{+0.028}_{-0.021} M_\odot$	0.024–0.128$M_\odot$
m	$3.3^{+4.9}_{-1.6} M_\oplus$	1.0–17.8$M_\oplus$
$a_\perp$	$0.62^{+0.22}_{-0.16}$ AU	0.33–1.14 AU
D_L	1.0 ± 0.4 kpc	0.5–2.0 kpc
I_S	21.44 ± 0.08	21.31–21.61
q	$1.8^{+1.9}_{-0.8} \times 10^{-4}$	0.5–7.1 $\times 10^{-4}$

7 bright-short microlensing events

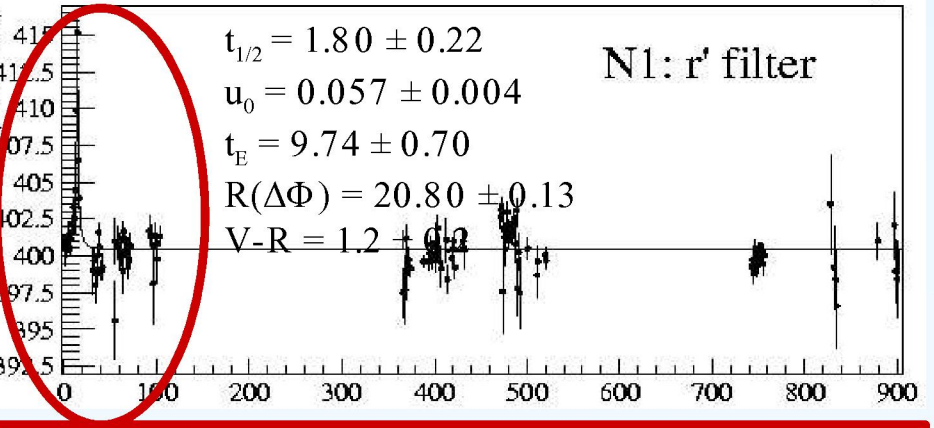

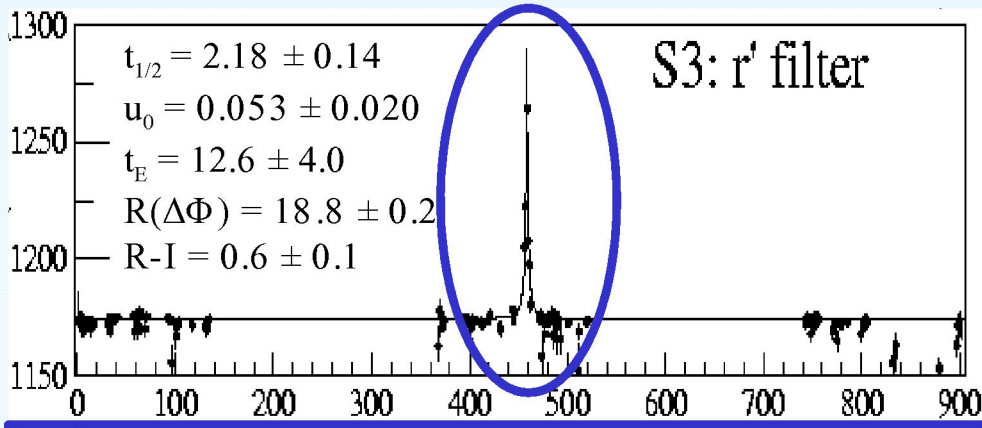

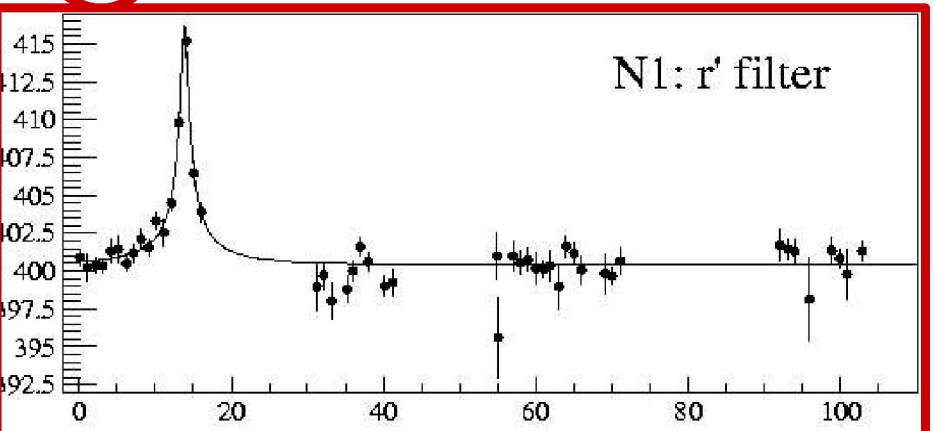

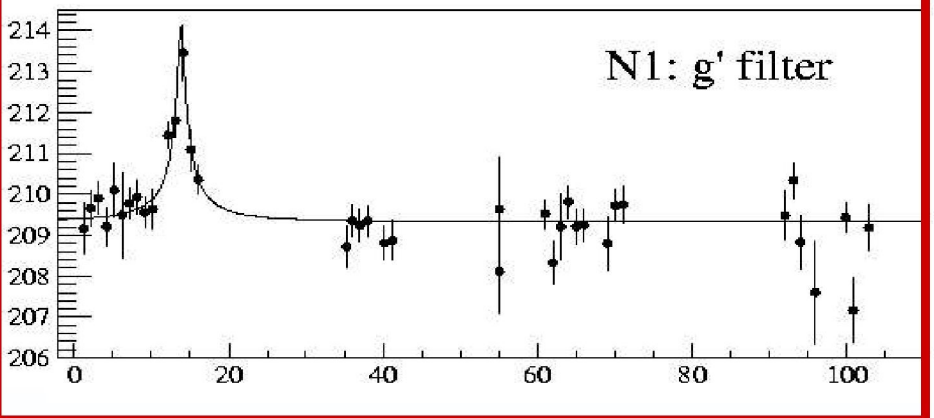

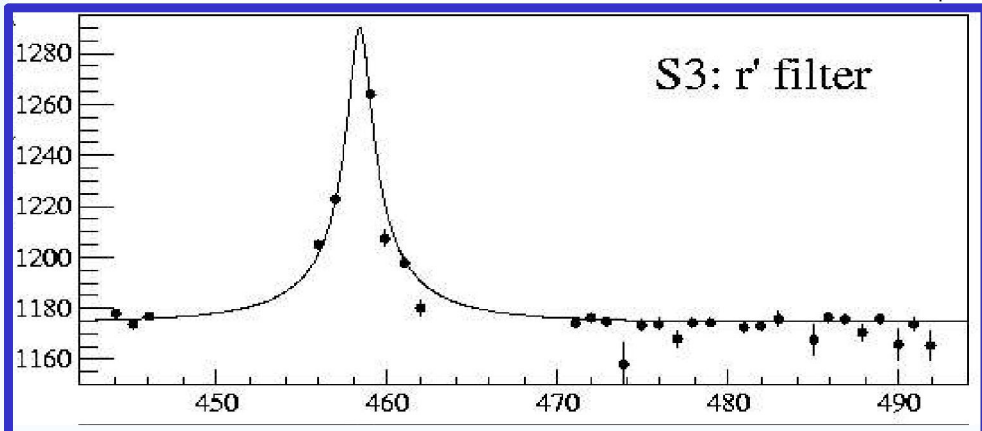

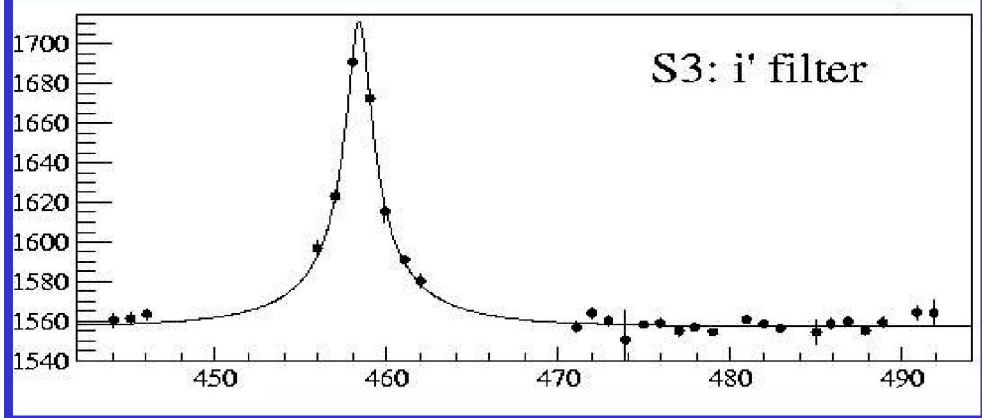

A&A 432, 501–513 (2005)
DOI: 10.1051/0004-6361:20041355

Astronomy & Astrophysics

Influence of magnification threshold on pixel lensing optical depth, event rate and time scale distributions towards M 31

F. De Paolis[1], G. Ingrosso[1], A. A. Nucita[1], and A. F. Zakharov[2,3]

[1] Dipartimento di Fisica, Università di Lecce and INFN, Sezione di Lecce, CP 193, 73100 Lecce, Italy
e-mail: ingrosso@le.infn.it
[2] Institute of Theoretical and Experimental Physics, 25, B. Cheremushkinskaya St., Moscow 117259, Russia
[3] Astro Space Centre of Lebedev Physics Institute, Moscow

Received 26 May 2004 / Accepted 2 November 2004

Abstract. Pixel lensing is the gravitational microlensing of light from unresolved stars contributing to the luminosity flux collected by a single pixel. A star must be sufficiently magnified, that is, the lens impact parameter must be less than a threshold value u_T if the excess photon flux in a pixel is to be detected over the background. Assuming the parameters of the Isaac Newton Telescope and typical observing conditions, we present maps in the sky plane towards M 31 of threshold impact parameter, optical depth, event number and event time scale, analyzing in particular how these quantities depend on u_T in pixel lensing searches. We use an analytical approach consisting of averaging on u_T and the star column density the optical depth, microlensing rate and event duration time scale. An overall decrease in the expected optical depth and event number with respect to the classical microlensing results is found, particularly towards the high luminosity M 31 inner regions. As expected, pixel lensing events towards the inner region of M 31 are mostly due to self-lensing, while in the outer region dark events dominate even for a 20% MACHO halo fraction. We also find a far-disk/near-disk asymmetry in the expected event number, smaller than that found by Kerins (2004). Both for self and dark lensing events, the pixel lensing time scale we obtain is $\simeq$1−7 days, dark events lasting roughly twice as long as self-lensing events. The shortest events are found to occur towards the M 31 South Semisphere. We also note that the pixel lensing results depend on $\langle u_T \rangle$ and $\langle u_T^2 \rangle$ values and ultimately on the observing conditions and telescope capabilities.

Key words. gravitational lensing – Galaxy: halo – cosmology: dark matter – galaxies: individual: M 31 – methods: observational

1. Introduction

Pixel lensing surveys towards M 31 (Crotts 1992; Baillon et al. 1993) can give valuable information to probe the nature of MACHOs (Massive Astrophysical Compact Halo Objects) discovered in microlensing experiments towards the LMC and SMC (Large and Small Magellanic Clouds) (Alcock et al. 1993; Aubourg et al. 1993) and also address the question of the fraction of halo dark matter in the form of MACHOs in spiral galaxies (Alcock et al. 2000).

This may be possible due to both the increase in the number of expected events and because the M 31 disk is highly inclined with respect to the line of sight and so microlensing by MACHOs distributed in a roughly spherical M 31 halo give rise to an unambiguous signature: an excess of events on the far side of the M 31 disk relative to the near side (Crotts 1992).

Moreover, M 31 surveys probe the MACHO distribution in a different direction to the LMC and SMC and observations are made from the North Earth hemisphere, probing the entire halo extension.

The Pixel lensing technique studies the gravitational microlensing of unresolved stars (Ansari et al. 1997). In a dense field of stars, many of them contribute to each pixel. However, if one unresolved star is sufficiently magnified, the increase of the total flux will be large enough to be detected. Therefore, instead of monitoring individual stars as in classical microlensing, one follows the luminosity intensity of each pixel in the image. When a significative (above the background and the pixel noise) photon number excess repeatedly occurs, it is attributed to an ongoing microlensing event if the pixel luminosity curve follows (as a function of time) a Paczynski like curve (Paczynski 1996).

Clearly, variable stars could mimic a microlensing curve. These events can be recognized by performing observations in several spectral bands and monitoring the signal from the same pixel for several observing seasons to identify the source.

Two collaborations, MEGA (preceded by the VATT/Columbia survey) and AGAPE have produced a number of microlensing event candidates, which show a rise in pixel luminosity in M 31 (Crotts & Tomaney 1996; Ansari et al. 1999; Auriere et al. 2001; Calchi Novati et al. 2002).

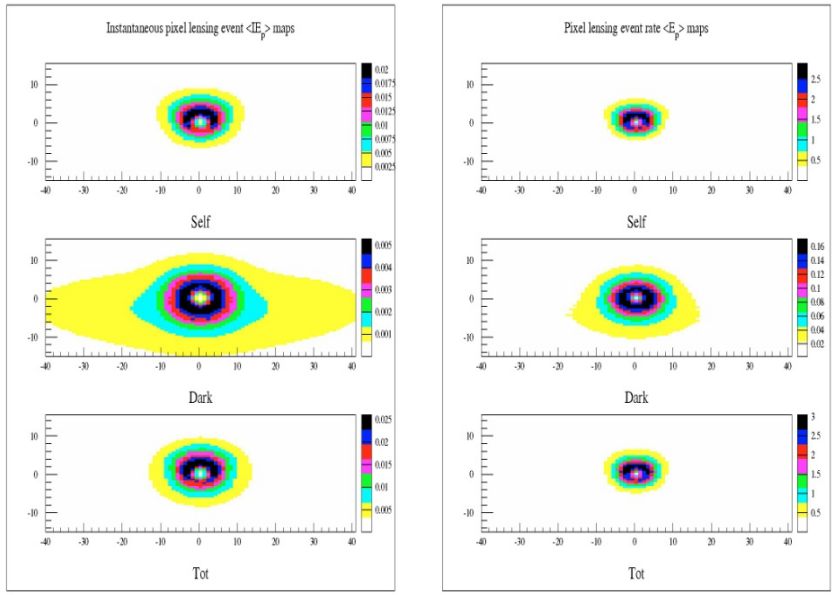

Fig. 5. In panel **a)**, the instantaneous pixel lensing event number density $\langle IE_{\rm p}(x,y)\rangle$ maps (events per arcmin^2) towards M 31 are given for self, dark and total lensing. In panel **b)** maps of pixel lensing event rate $\langle E_{\rm p}(x,y)\rangle$ (events per year and per arcmin^2) are given, in the same cases.

expected total number of events detectable by monitoring for 1 year the 100×70 arcmin^2 region oriented along the major axis of M 31 (events within 8 arcmin from the center are excluded). The first four lines refer to the models considered in Table 1 and to the parameters in the third row of Table 2. As one can see, the obtained results for the Reference model are intermediate with respect to those for the other more extreme models.

In the last row of Table 3, for the Reference model we show how the expected event number changes considering a different value of $\langle u_{\rm T}\rangle_\phi \simeq 1.44 \times 10^{-2}$ (see 5th row in Table 2). As expected, one can verify that roughly the event number scales as $\langle u_{\rm T}\rangle_\phi$.

Similar results have been obtained in previous simulations (see, e.g. Kerins 2004, and references therein). We also note that our numerical results scale with the fraction of halo dark matter in form of MACHOs and with the MACHO mass by a factor $(f_{\rm MACHO}/0.2)\ \sqrt{0.5\ M_\odot/m_{\rm l}}$.

In Table 4 we give the total event number $\langle E_{\rm p}\rangle$ for different lens populations (bulge, disk and halo) located in M 31. As one can see, the ratio dark/total events depends on the considered model, varying from 0.07 (for the massive disk model) to 0.40 for the massive halo model.

To study the far-disk/near-disk asymmetry, in the last three columns of Table 4 we give results for the South/North M 31 Semispheres and in brackets their ratio. For the Reference model, we find that self-lensing events are roughly symmetric (the same is true for lenses located in the MW disk and halo, not given in the table), while events due to lenses in M 31 halo are asymmetrically distributed with a ratio of about 2. The asymmetry is particularly evident (in the last column of the table) for sources located in the disk.

In Table 5 the instantaneous total number of events $\langle IE_{\rm p}\rangle$ within the considered M 31 region is given. The first four rows refer to the parameter values $\langle m_{\rm b}\rangle \simeq 0.31\ M_\odot$, $\langle m_{\rm d}\rangle \simeq 0.53\ M_\odot$, $f_{\rm MACHO} = 0.2$ and $\langle u_{\rm T}^2\rangle_\phi \simeq 9.56 \times 10^{-3}$ (used throughout the paper). For comparison with the results obtained by Kerins (2004), in the last four rows of Table 5 we present our results for $\langle m_{\rm b}\rangle \simeq 0.5\ M_\odot$, $\langle m_{\rm d}\rangle \simeq 0.5\ M_\odot$, $f_{\rm MACHO} = 1$ and $\langle u_{\rm T}^2\rangle_\phi \simeq 1.17 \times 10^{-3}$. The asymmetry ratio we obtain is always rather smaller than that quoted by Kerins (2004).

As it has been mentioned by several authors, in order to discriminate between self and dark lensing events, it is important to analyze the event duration. Indeed self-lensing events are expected to have, on average, shorter duration with respect to events due to halo MACHOs.

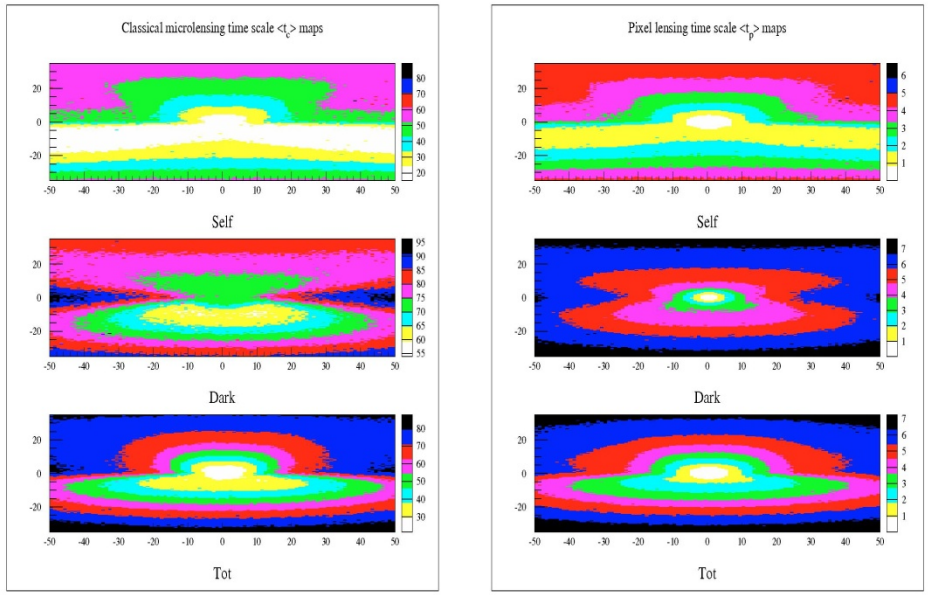

Fig. 6. In panel **a)**, mean classical event duration time $\langle t_c(x,y)\rangle$ (in days) maps towards M 31 are given for self, dark and total lensing. In panel **b)** for pixel lensing, maps of $\langle t_p(x,y)\rangle$ are given, in the same cases.

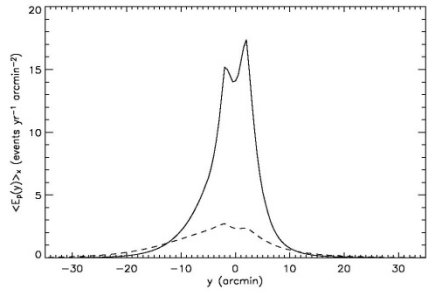

Fig. 7. The projected (along the x axis) mean event number $\langle E_p(y)\rangle_x$ is given as a function of the coordinate y for the Reference model. The dashed line refers to dark lensing events by MACHOs in M 31 and MW halos while the solid line is for self-lensing events by stars in M 31 bulge and disk.

6.4. Pixel lensing event time scale

Maps of mean event duration time scale in classical and pixel lensing are shown in Figs. 6a and 6b.

Here we use the probability, for each location of sources and lenses given in Eq. (26), of obtaining event duration maps for self and dark microlensing events.

As expected, short duration events are mainly distributed towards the inner regions of the galaxy and this occurs for both $\langle t_c(x,y)\rangle$ and $\langle t_p(x,y)\rangle$. The main effect of $\langle u_T(x,y)\rangle_\phi$ is to decrease the event time scale, in particular towards the inner regions of M 31, giving a larger number of short duration events with respect to expectations based on $\langle t_c(x,y)\rangle$ calculations.

Both for self and dark events the pixel lensing time scale we obtain is $\simeq$1–7 days, in agreement with results in Kerins (2004), but much shorter with respect to the duration of the events observed by the MEGA Collaboration (de Jong et al. 2004). This is most likely due to the fact that current experiments may not detect events shorter than a few days.

However, the pixel lensing time scale values depend on $\langle u_T(x,y)\rangle_\phi$ and ultimately on the observational conditions and the adopted analysis procedure. Indeed from Table 2 one can see that the $\langle u_T(x,y)\rangle_\phi$ value may be easily doubled, changing the adopted parameters and therefore giving longer events.

In Fig. 8 the pixel lensing event duration $\langle t_p(y)\rangle$ averaged along the x direction is given as a function of the y coordinate. The dashed line refers to dark lensing events by MACHOs

Pixel-lensing and extra-solar searches
G. Ingrosso, S. Calchi-Novati, F. De Paolis, P. Jetzer, A. Nucita, AFZ
(MNRAS, in press, arXiv:0906.1050)

Planets with masses 0.1 Earth masses may be detected in M31


NASA

Hint of planet outside our galaxy

By Jason Palmer

Science and technology reporter, BBC News

Astronomers believe they have seen hints of the first planet to be spotted outside of our galaxy.

Situated in the Andromeda galaxy, the planet appears to be about six times the mass of Jupiter.

The method hinges on gravitational lensing, whereby a nearer object can bend the light of a distant star when the two align with an observer.

The results will be published in Monthly Notices of the Royal Astronomical Society (MNRAS).

The team, made up of researchers from the National Institute of Nuclear Physics (INFN) in Italy and collaborators in Switzerland, Spain, and Russia, exploited a type of gravitational lensing called microlensing.

The effect of large, massive objects between an observer and a distant planet or star can cause distortion or multiple images as the

AP/NASA

First Planet in Another Galaxy Possibly Found

Friday, June 12, 2009

FOX NEWS

The Andromeda galaxy in a NASA composite image.

Astronomers may have found the first planet in another galaxy, according to New Scientist magazine.

Planet : PA-99-N2 b

THE PLANET

Basic data :

Name	PA-99-N2 b
Discovered in	2009
M.sin *i*	6.34 M_J ref.
Update	16/06/09

http://exoplanet.eu/planet.php?p1=PA-99-N2&p2=b&showPubli=yes&sortByDate

Remarks :

Reanalysis of data by An et al 2004

2 related publications : (sort by author) (sort by date)

AN J., EVANS N., KERINS E., BAILLON P., CALCHI NOVATI S., CARR J., CREZE M., GIRAUD-HERAUD Y., GOULD A., HEWETT P., JETZER Ph., KAPLAN J., PAULIN-HENRIKSSON S., SMARTT S., TSAPRAS Y. & VALLS-GABAUD D. (The POINT-AGAPE Collaboration) , 2004

The anomaly in the candidate microlensing event PA-99-N2

ApJ. , **601** , 845

paper

INGROSSO G., CALCHI NOVATI S., DE PAOLIS F., JETZER Ph., NUCITA A. & ZAKHAROV A. , 2009

Pixel-lensing as a way to detect extrasolar planets in M31

MNRAS , **-** , -

accepted

preprint

THE STAR in M31

Name	PA-99N2
Distance	670000 *pc*
Mass	0.5 M_{sun}

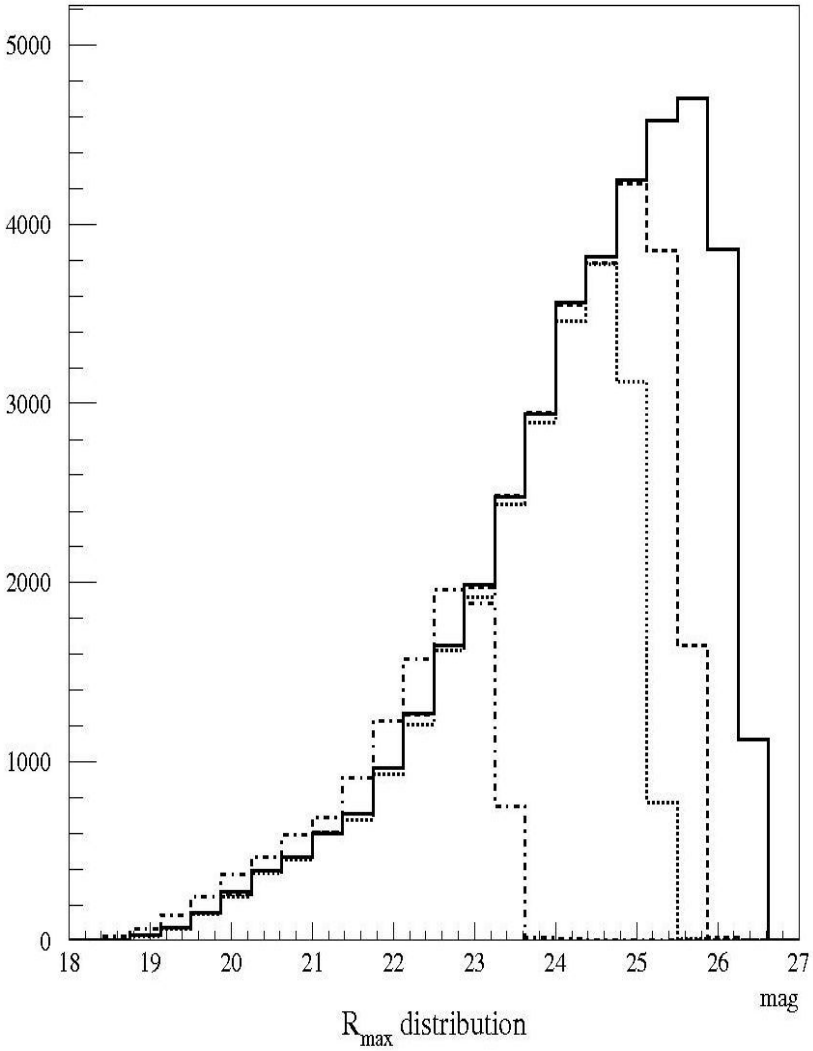

Figure 1. Normalised distributions of R_{max} for detectable pixel-lensing events with telescopes having different sizes $D =$ 1.5, 2.5, 4, 8 m.

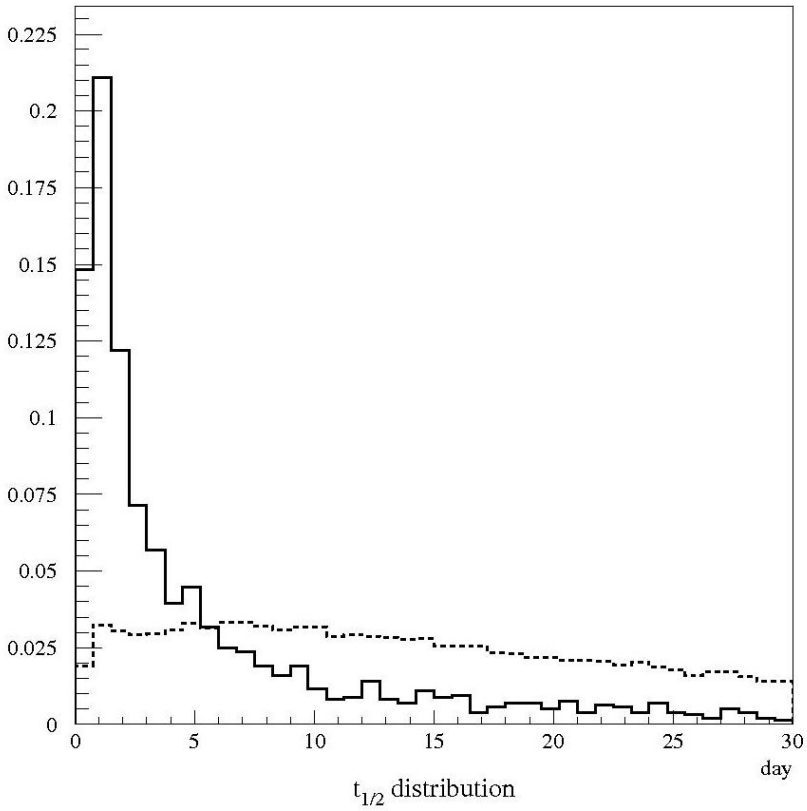

Figure 2. Normalized distributions of $t_{1/2}$ (the duration of a microlensing event without planet) for events with $\chi^2_r > 4$ and $N_{good} > 3$ (solid lines) and for simulated events (dashed lines). Here we take $D = 8$ m telescope parameters.

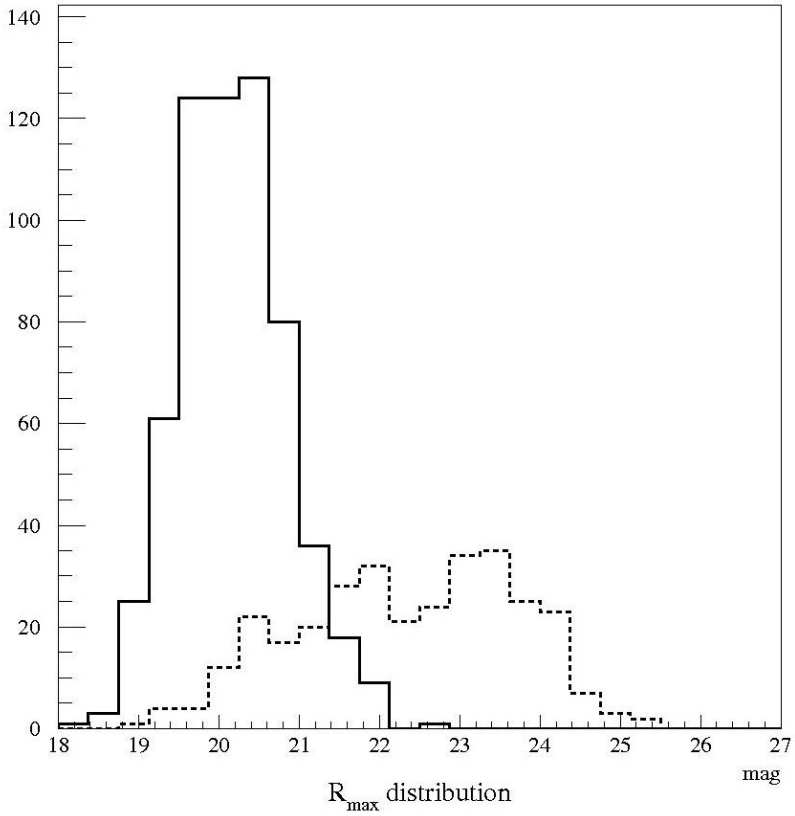

Figure 3. Normalized distributions of R_{max} for events with $\chi^2_r > 4$ and $N_{good} > 3$, assuming a telescope diameter $D = 8$ m. Events with $\rho/u_0 > 1$ (solid line) and $\rho/u_0 < 1$ (dashed line) are shown.

Table 2. Parameters of events shown in Figs. 4 - 8. We also give in the last two columns the sum of residuals χ_r and the maximum value of the mean (with respect to the source area Σ) planetary signal $< \epsilon >_{max}$.

	ρ/u_0	u_0	d_P/R_E	M_P ($M_\oplus$)	θ (deg)	R_E (AU)	t_E (day)	R_{max} (mag)	$t_{1/2}$ (day)	χ_r	$\chi_{r\ max}$	$< \epsilon >_{max}$
#1	2.89	9.47×10^{-3}	0.90	1525	341.8	2.2	16.1	20.2	0.5	194	730	642
#2	1.18	2.63×10^{-2}	0.68	265	104.8	2.8	52.1	21.1	4.0	43	980	249
#3	0.04	3.74×10^{-1}	1.17	0.3	298.0	3.2	23.7	24.1	18.7	9	77	381
#4	0.12	3.56×10^{-1}	2.25	71	190.3	2.3	18.7	23.5	16.5	13	79	566
#5	0.08	1.62×10^{-1}	1.32	1278	336.0	3.9	28.4	23.8	13.3	37	153	1323

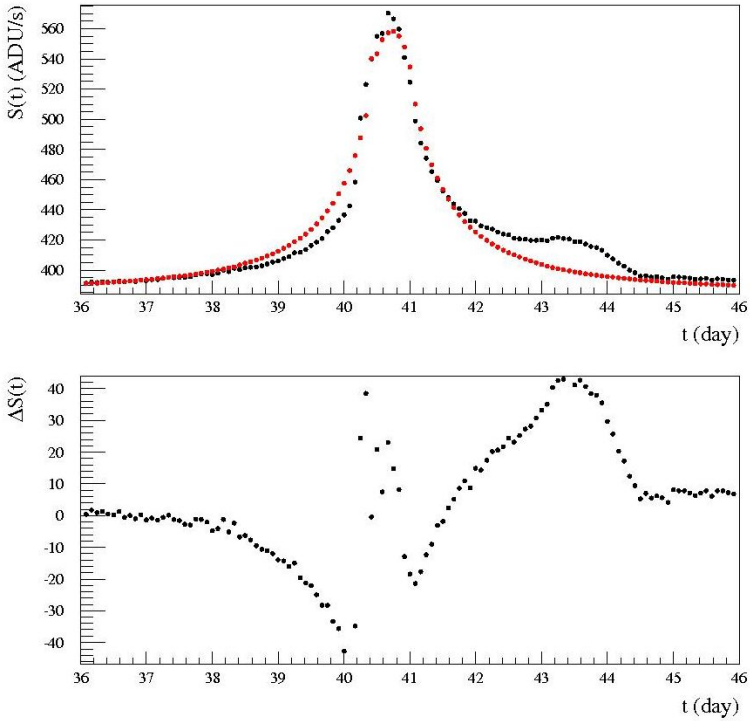

Figure 4. Event of the I class #1 (see Table 2). The upper panel shows the simulated light curve and the corresponding best fit model (a Paczyński light curve modified for finite source effects). The lower panel gives the difference.

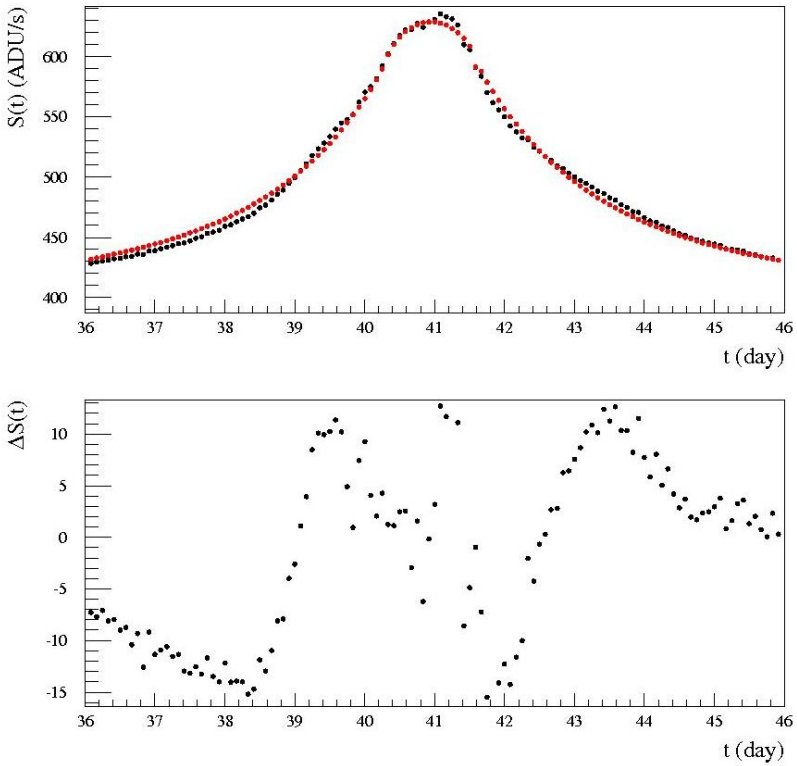

Figure 5. The same as in Fig. 4 for the I class event #2 (see Table 2).

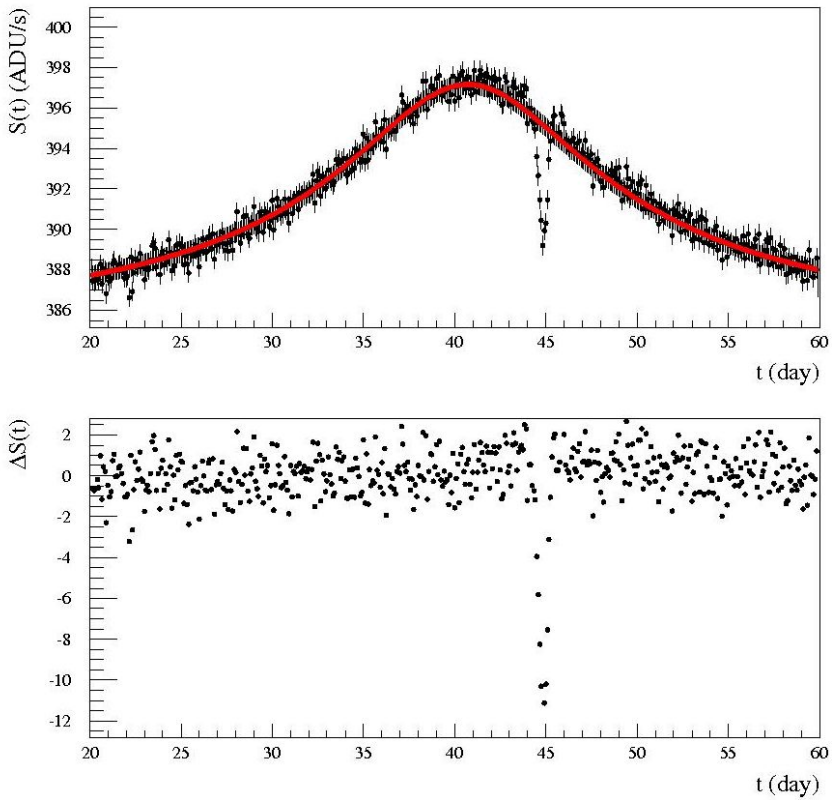

Figure 6. The same as in Fig. 4 for the second class event #3 (see Table 2).

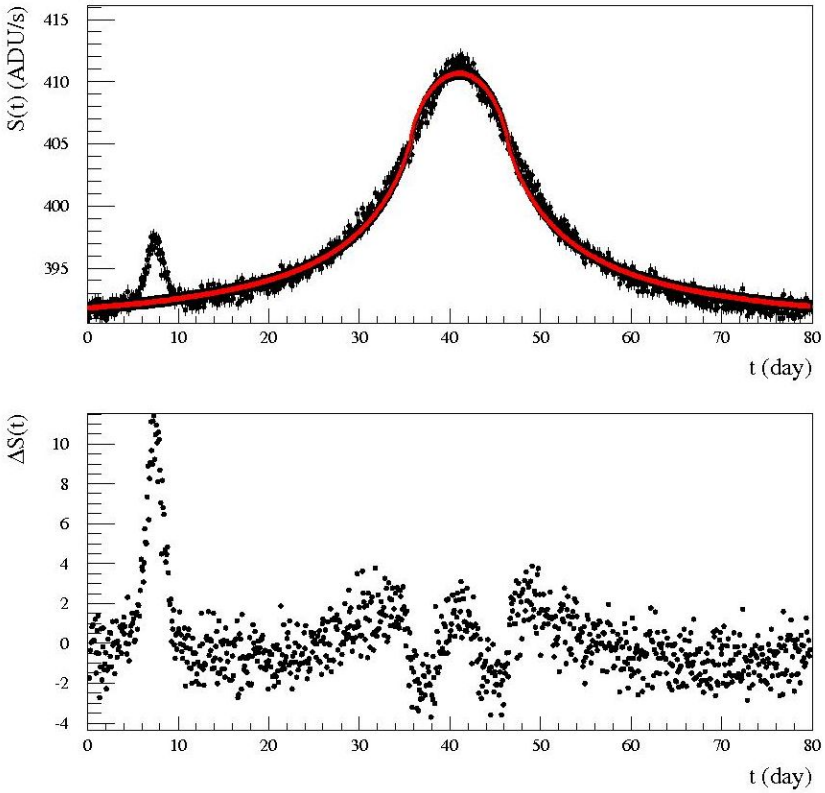

Figure 7. The same as in Fig. 4 for the second class event #4 (see Table 2).

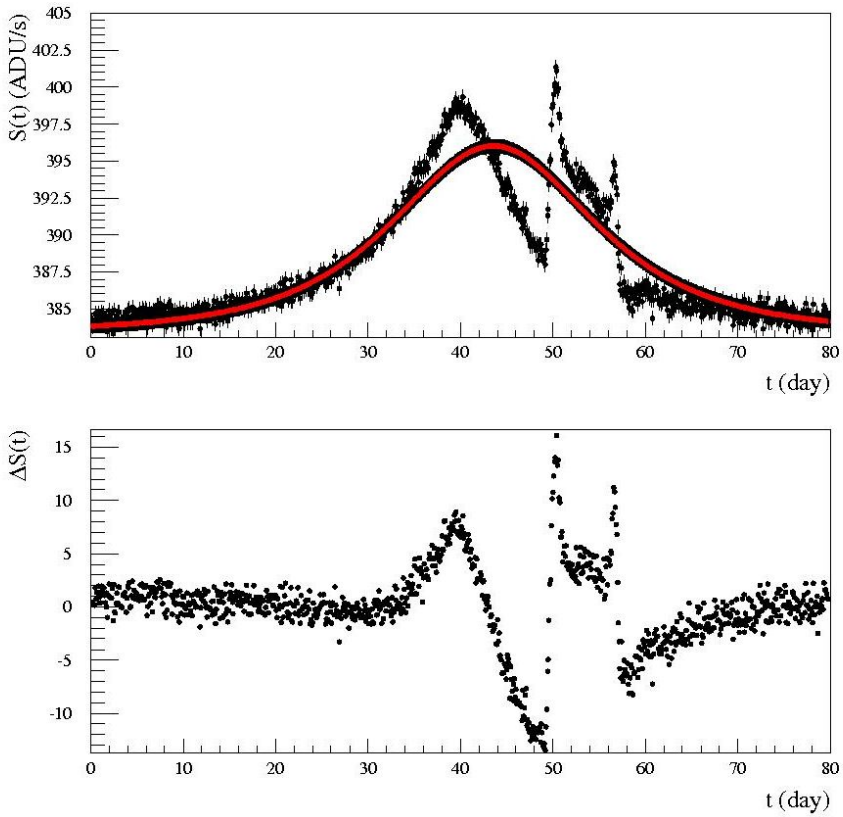

Figure 8. The same as in Fig. 4 for the second class event #5 (see Table 2).

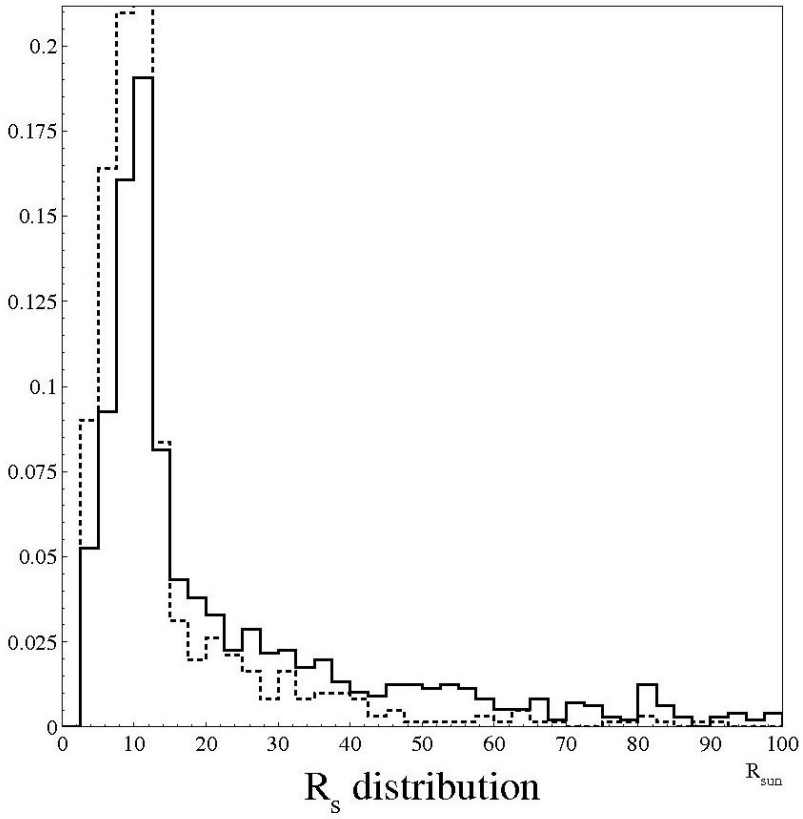

Figure 7. The distribution of the source radius for first (solid line) and second (dashed line) class of events.

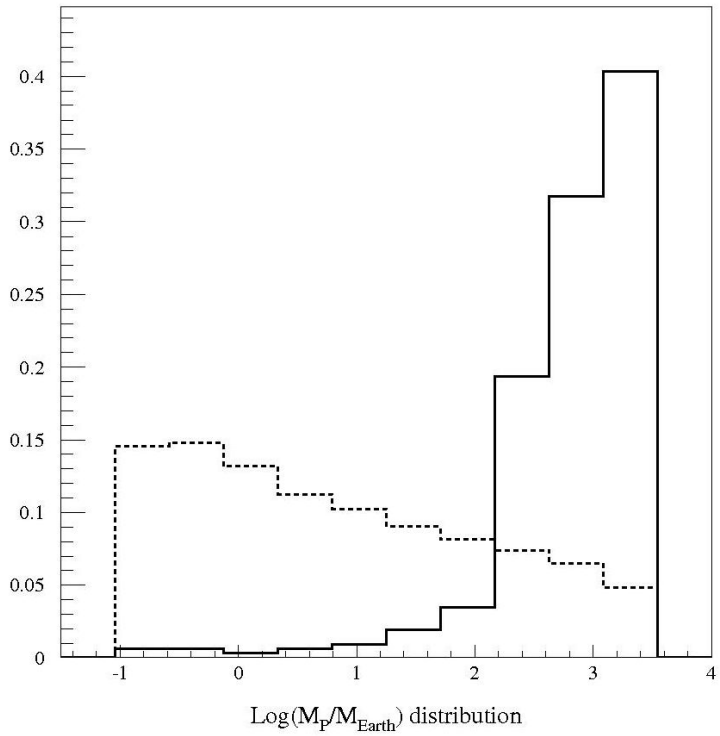

Figure 8. The distribution of the planet mass M_P for the second class of events is shown (solid line). For comparison, the M_P distribution of the generated events is also shown (dashed line). Here we take $N_{im} = 12$ day^{-1} and $D = 8$ m.

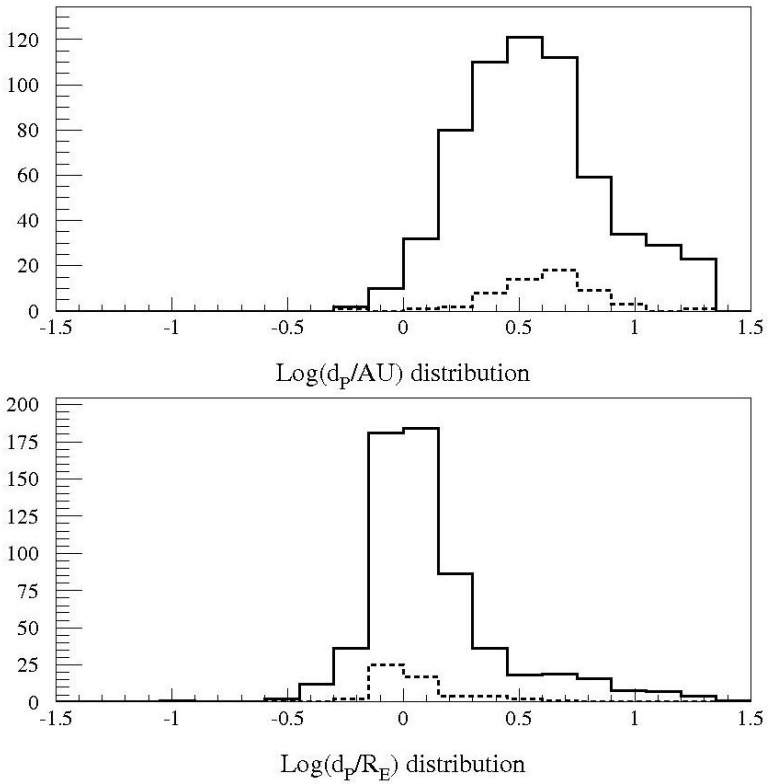

Figure 9. Upper panel: for the second class of events, distributions of the star-to-planet separation d_P (in AU units) for all (solid line) and small planetary mass ($M_P < 20\ M_\oplus$, dashed line). Lower panel: distributions of $s = d_P/R_{\rm E}$ for events as before.

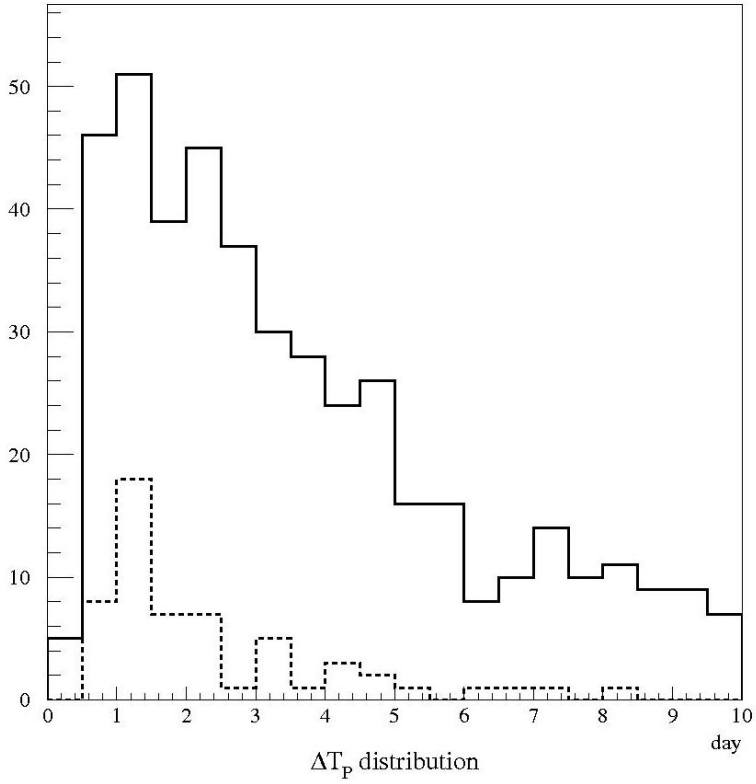

Figure 10. Time duration ΔT_P distributions for all (solid line) and low (dashed line) planetary masses, for the second $(\rho/u_0 < 1)$ class of events.

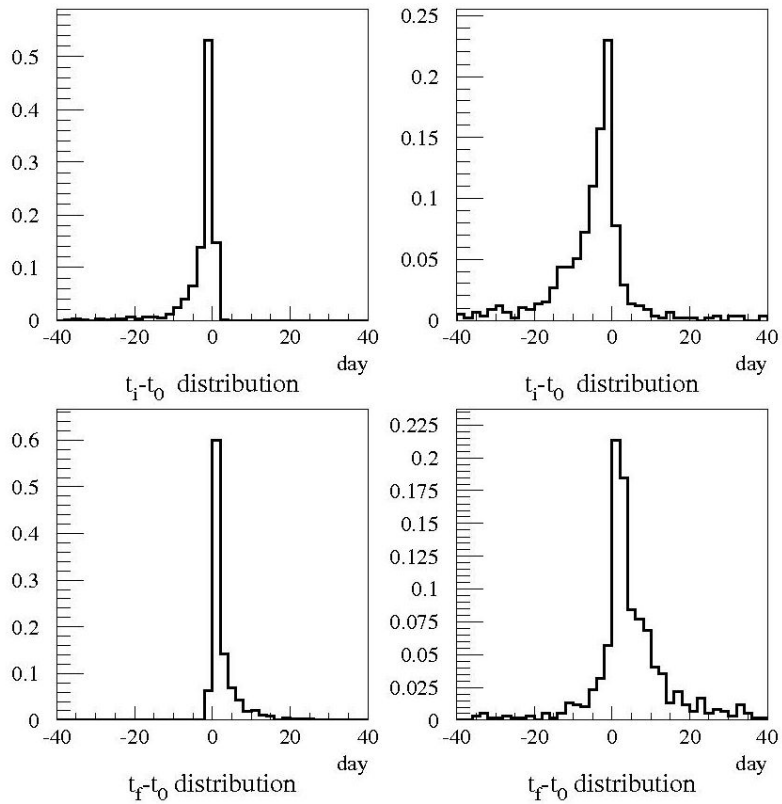

Figure 11. Histograms for the differences $(t_i - t_0)$ (left panels) and $(t_f - t_0)$ (right panels) for first (upper panels) and second (lower panels) classes of events. Initial and final instants for the start and the end of significant (at least 3 points over 3σ) deviations in light curves are denoted by t_i and t_f, while t_0 is the instant of maximum on the light curve for a lens without planet.

Table 1. First class pixel-lensing events ($\chi^2_r > 4$, $N_{good} > 3$ and $\rho/u_0 > 1$). Mean values of lensing parameters: maximum flux deviation $< R_{max} >$, full-width half-maximum event duration $< t_{1/2} >$, Einstein radius $< R_{\rm E} >$, planet-to-star distance $< d_P >$ and planet mass $< M_P >$.

l.o.s.	$< R_s >$ $R_\odot$	$< R_{max} >$ (mag)	$< t_{1/2} >$ (day)	$< R_{\rm E} >$ (AU)	$< d_P >$ (AU)	$< M_P >$ ($M_\oplus$)	$< \Delta T_P >$ (day)
A	26.0	20.01	2.26	2.35	6.34	197	4.3
B	25.2	19.97	2.43	2.73	6.68	148	6.3
C	27.9	19.82	3.14	3.06	6.29	187	7.1
D	24.5	20.18	3.14	2.08	5.99	205	6.3

Table 2. As in Table 1 for the second class pixel-lensing events ($\chi^2_r > 4$, $N_{good} > 3$ and $\rho/u_0 < 1$).

l.o.s.	$< R_s >$ $R_\odot$	$< R_{max} >$ (mag)	$< t_{1/2} >$ (day)	$< R_{\rm E} >$ (AU)	$< d_P >$ (AU)	$< M_P >$ ($M_\oplus$)	$< \Delta T_P >$ (day)
A	14.9	23.31	11.46	2.60	4.99	1024	6.8
B	12.9	22.89	13.12	3.32	4.57	905	9.0
C	14.5	22.94	14.56	3.66	5.68	863	11.3
D	15.1	23.20	13.75	2.50	3.77	929	11.5

Table 3. Probability to detect pixel-lensing events (second column) and to find planetary features ($\chi^2_r > 4$ and $N_{good} > 3$) for first ($\rho/u_0 > 1$, third column) and second ($\rho/u_0 < 1$, fourth column) classes of events for telescopes of different diameters, assuming $N_{im} = 12$ day^{-1} and $t_{exp} = 30$ min.

D (m)	P_{p-l} (%)	P_I (%)	P_{II} (%)
1.5	27	0.1	0.04
2.5	62	0.8	0.46
4	78	1.5	0.78
8	100	2.5	1.53

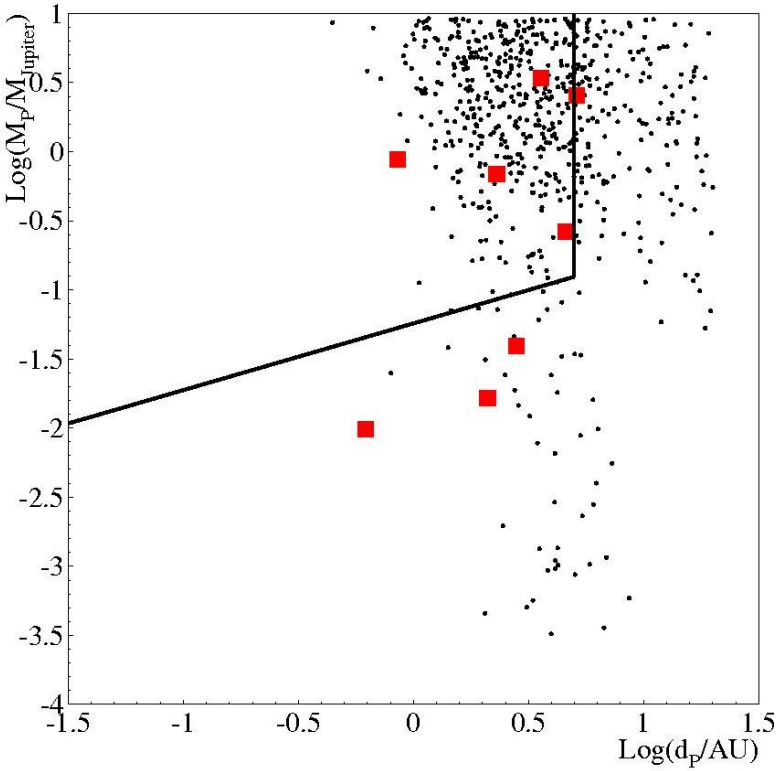

Figure 11. Scatter plot of the planet mass (in unit of Earth mass) vs planet distance (in Astronomical Units). The solid thick line delimits the region (upper and left) of planet detection accessible by the radial velocities, transit and direct imaging methods. The eight small boxes are the planets detected by the microlensing technique. Starting from a sample of 40,000 detectable pixel-lensing events ($D = 8$ m), 630 selected events (indicated by black dots) with $\chi_{\rm r} > 4$, $N_{\rm good} > 3$ and $\langle\epsilon\rangle_{\rm max} > 0.1$ show planetary features and among these 48 events have $M_{\rm P} < 20\ M_{\oplus}$.

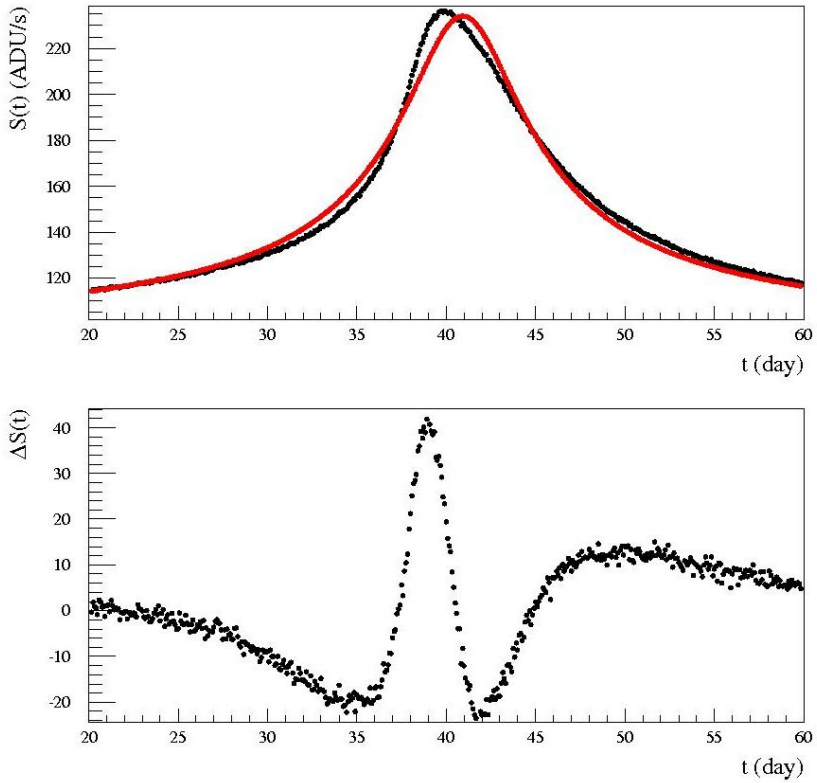

Figure 16. The upper panel shows the simulated light curve of an event with the parameters of the best fit finite source model for the PA-99-N2 event (An et al. 2004). In particular, $d_P = 0.68\ R_E$, $q = 7.59 \times 10^{-3}$ (corresponding to a planet mass $M_P = 2670\ M_\oplus$ for a lens mass of $M_l = 1\ M_\odot$), $u_0 = 0.0386$, $t_E = 124.3$ day, $v_\perp = 340$ km s^{-1} and $\theta = 26.4$ deg. We take the source magnitude $M_r = -2.0$, and a source radius of $R_s = 14\ R_\odot$ (the average radius for a second class event), consistently with the above mentioned analysis. The lower panel gives the difference with respect to the Paczyński light curve (modified for finite source effects) for the same parameters. Here we use the INT telescope parameters and $N_{im} = 12$ day^{-1}.

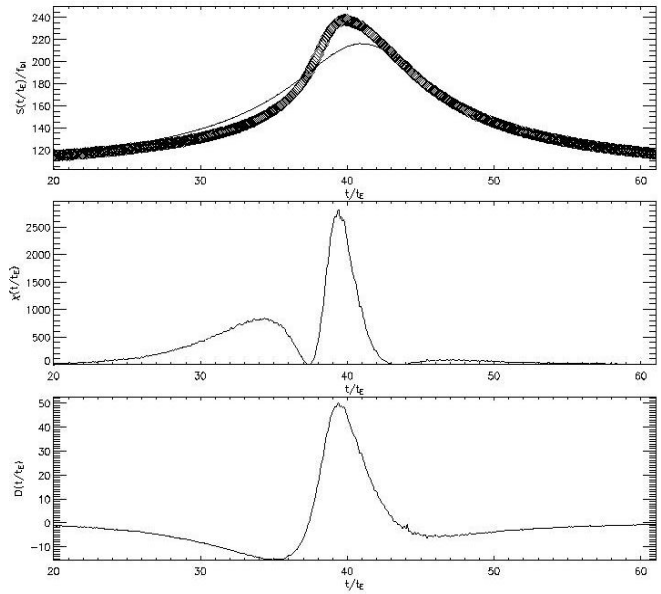

Figure 13. The upper plot shows the simulated light curve of an event with the parameters of the best fit finite source model for the PA-99-N2 event (An et al. 2004). In particular, $d_P = 0.68\ R_E$, $q = 7.59 \times 10^{-3}$ (corresponding to a planet mass $M_P = 2670\ M_\oplus$ for a lens mass of $M_l = 1\ M_\odot$), $u_0 = 0.0386$, $t_E = 124.3$ day, $v_\perp = 340$ km s^{-1} and $\theta = 26.4$ deg. We take the source magnitude $M_r = -2.0$, and a source radius of $R_s = 14\ R_\odot$ (the average radius for a second class event), consistently with the above mentioned analysis. The central plot gives the residuals with respect to the Paczyński light curve (modified for finite source effects) for the same parameters and the lowest plot gives the parameter $\mathcal{D}$. Here we use the INT telescope parameters and $N_{im} = 12$ day^{-1}.

Thanks for your kind attention

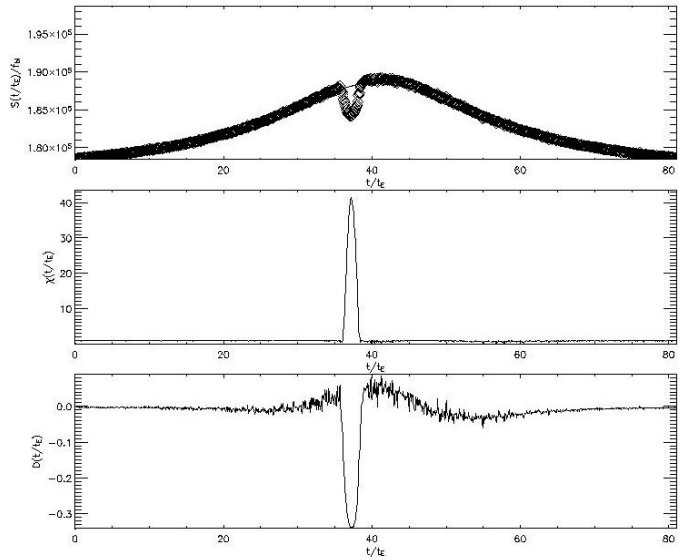

Figure 5. The same as in Fig. 4 for an event with the following parameters: $M_l = 0.27\ M_\odot$, $M_r = -0.74$ mag and $R_s = 24.5\ R_\odot$, $R_E = 4.03$ AU and $t_E = 43.36$ day, $u_0 = 0.32$, $R_{max} = 23.22$ and $t_{1/2} = 34.8$ day, $M_P = 0.15\ M_\oplus$, $d_P = 1.19\ R_E$, $\theta = 4.44$ rad, $\rho/u_0 = 0.03$.

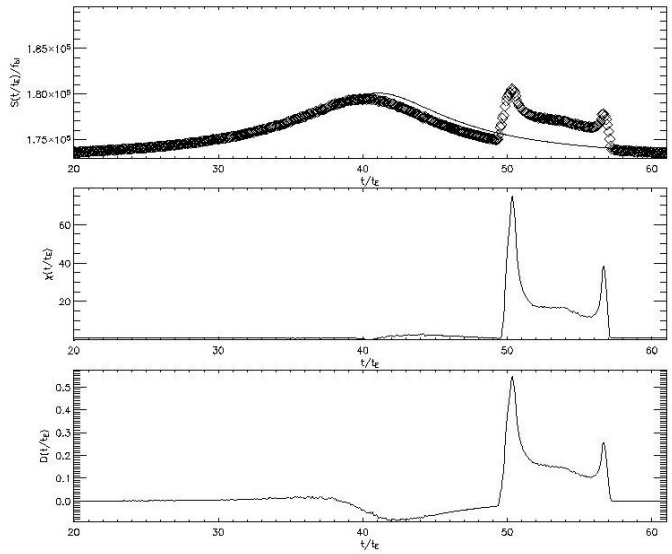

Figure 6. The same as in Fig. 4 for an event with the following parameters: $M_l = 0.21\ M_\odot$, $M_r = 0.72$ mag and $R_s = 10.2\ R_\odot$, $R_E = 3.90$ AU and $t_E = 28.44$ day, $u_0 = 0.16$, $R_{Max} = 23.78$ and $t_{1/2} = 13.3$ day, $M_P = 1278\ M_\oplus$, $d_P = 1.32\ R_E$, $\theta = 5.86$ rad, $\rho/u_0 = 0.075$.

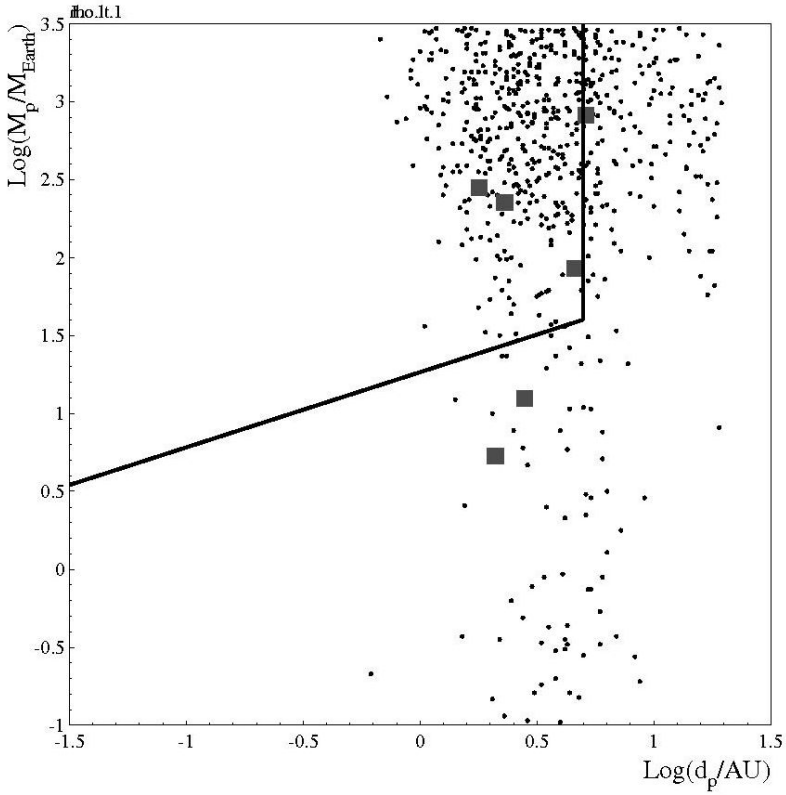

Figure 12. Scatter plot of the planet mass (in unit of Earth mass) vs planet distance (in Astronomical Units). The solid thick line delimits the region (upper and left) of planet detection by the standard techniques (radial velocities and transit). The six small boxes are the planets detected by microlensing. Starting from a sample of 40,000 detectable pixel-lensing events, 612 events (with $\rho/u_0 < 1$) show planetary features and among these 57 events have $M_P < 20\ M_\oplus$.

Conclusions

- **EROS finds the expected rates of events in 5 directions in the galactic plane**
- But very few events towards the Magellanic clouds
- Compact objects $10^{-7}\ M_{sun} < M < 20\ M_{sun}$ are **NOT** a major component of the galactic halo